Identifying Soil Erosion Processes in the Alps using Machine Learning Techniques

Inauguraldissertation

zur

Erlangung der Würde eines Doktors der Philosophie vorgelegt der Philosophisch-Naturwissenschaftlichen Fakultät der Universität Basel

von

Lauren Zweifel

Basel, 2021

Genehmigt von der Philosophisch-Naturwissenschaftlichen Fakultät
auf Antrag von

Prof. Dr. Christine Alewell

Erstbetreuerin

Prof. Dr. Heiko Schuldt

Zweitbetreuer

Prof. Dr. Michael Maerker

Externer Experte

Basel, den 22.6.2021

Prof. Dr. Marcel Mayor

Dekan

Contents

Abstract

Soils are an important part of our ecosystem and a significant resource, which ought to be protected. A major threat to soil is the degradation caused by soil erosion. Alpine regions are affected by soil erosion mainly due to the prevailing climate conditions (triggered by wind, water/snow) and the steep terrain (gravitational processes). Soil erosion is further increased due to climate change related factors (e.g., more extreme precipitation events) as well as changing land-use practices (e.g., more intensely used/abandoned pastures). Monitoring of soil erosion processes is therefore crucial for gaining a holistic understanding of spatial and temporal developments. However, it is difficult to observe the extent of ongoing soil erosion in Alpine terrain due to the inaccessibility of regions, steep topography, and the vastness of affected regions. To successfully overcome many of these restrictions, we use remote sensing approaches with the use of machine learning techniques.

Our aim was to identify different soil erosion processes and to map the location and extent of these soil erosion sites. For this purpose, multiple mapping methods are explored. The results produced with the monitoring tools are further analysed to understand the spatial distribution and temporal developments of soil erosion sites and to identify potential causal factors. Degraded sites are classified according to the *major erosion process* (shallow landslides; sites with reduced vegetation cover affected by sheet erosion) or *triggering factors* (trampling by livestock; management effects).

In a first step, we developed a semi-automatic workflow based on Object-based Image Analysis (OBIA), with which soil erosion features are mapped on the basis of high-resolution aerial images (0.25-0.5 m, RGB spectral bands) and a digital terrain model (2 m). This approach is used to map erosion sites and assign corresponding classes located within the Urseren Valley (Central Swiss Alps, Canton Uri) at five different time steps during a 16-year study period (aerial images of 2000, 2004, 2010, 2013 and 2016). The area affected by soil erosion increased by a total of 156% ± 18% during these 16 years. OBIA yields high quality results but the workflow presents multiple constraints, such as labour and time intensive steps or a lack of transferability to other regions, which make the method unsuitable for larger scale applications.

We therefore applied a deep learning approach, which can be used in a faster and more efficient manner. This approach uses fully-convolutional neural networks with the U-Net architecture and is capable of rapid segmentation and classification of aerial images in order to identify soil erosion sites. The mapping results of the OBIA study are used as training data (9 km^2 training area) for this U-Net mapping tool. We compare the results of the U-Net to those of OBIA for a held-out test region in the Urseren Valley (17 km^2 testing area) and found that the U-Net performs on par with OBIA in terms of segmentation of erosion sites as well as the identified temporal trends (16-year period). Both the *spatial* (within the Urseren Valley) and *temporal* (data from new year not seen during training) transferability were tested. Due to method-specific differences, the U-Net achieves a F_1-score of 78% when compared to OBIA results. However, visual assessments indicate that the U-Net is slightly more accurate than OBIA (U-Net maps additional affected sites).

With the U-Net tool, grassland areas can be mapped efficiently. Ten study sites across Switzerland (8 located in the Alps, 1 in the foothill region of the Alps, 1 in the Jura mountains) were selected to map the location and extent of *shallow landslides*, to identify potential causal factors and to better understand regional differences. Using a logistic regression with a Group Lasso variable selection method we identify important variables from a set of explanatory variables consisting of traditional susceptibility modelling factors as well as climate-related factors representing local and cross-regional conditions. Due to different conditions of the study sites, different important explanatory variables are identified (regression model accuracies between 70.2 and 79.8%). However, slope and aspect are amongst the most consistent. A model evaluating all sites simultaneously (regression model accuracy 72.3%) confirms these findings and further selects topographic roughness as an additional important variable. Sites with better regression model performance are located in the Alps and tend to have an east-west orientation of the valley axis, possibly capturing processes related to slope exposition (e.g., snow gliding on South facing slopes).

As snow gliding is thought to be an important trigger for soil erosion during winter months, we calculate a spatial snow glide model (SSGM) for Switzerland based on a 30-year winter precipitation average. Modelled snow glide distances are compared to shallow landslide densities of the ten mapped study sites. Correlations were found between higher snow glide distances and higher shallow landslide densities (and vice versa). For more detailed evaluations on the connection between snow gliding and soil erosion, additional high resolution data sets (winter precipitation) and higher temporal resolutions of mapped erosion sites are needed, as snow gliding is generally event based (i.e., during strong '*snow glide winters*').

During this thesis, a monitoring tool was developed, which allows for mapping and subsequent analysis of soil erosion sites located on grasslands with unprecedented efficiency. This will allow for future large scale applications such as nation-wide or even Alpine-wide studies. The produced data sets may accompany other studies on soil erosion (e.g., erosion modelling) and may serve as the basis for land-use mitigation strategies.

List of Figures

List of Tables

Abbreviations

OBIA Object-based Image Analysis

UAV Unmanned Aerial Vehicle

GSD Ground Sample Distance

RGB Red, Green, Blue (spectral bands)

DTM Digital Terrain Model

ExG Excess Green Index

GLCM Grey Level Co-occurrence Matrix

CNN Convolutional Neural Networks

NIR Near-Infrared

U-Net Name of the CNN architecture

GIS Geographic Information System

ReLU Rectified Linear Unit

GPU Graphics Processing Unit

ROC Receiver-Operator-Characteristics

AUC Area-Under-Curve

BS Brier Score

TPR True Positive Rate

FPR False Positive Rate

TWI Topographic Wetness Index

SLS Shallow Landslide

SSGM Spatial Snow Glide Model

Cattle in the Swiss Alps
Photo: Max Itin

1 Introduction

1.1 Soil Erosion

Soils are a crucial component, if not the basis of terrestrial ecosystems and provide essential ecosystem services to us humans. These functions include carbon and nutrient storage and cycling, water cycling, climate regulation, or providing habitat and food for organisms, to name a few (FAO and ITPS, 2015). Soil erosion, which is defined as the removal of topsoil through wind, water or tillage, is known to be a major global threat to the environment, leading to soil degradation and soil loss (FAO and ITPS, 2015; Lal, 2001; Pimentel et al., 1995; Pimentel, 2006). There are various on- and off-site effects of soil erosion, such as deterioration of soil quality and nutrient reserves, reduction of water retention capacity, emission of greenhouse gases or water pollution (Lal, 2004, 2014, 2019; Pimentel and Burgess, 2013). Indirect and direct anthropogenic influences (e.g., climate change and land use change) are linked to the acceleration of soil erosion rates (Borrelli et al., 2020; Li et al., 2016; Märker et al., 2008; Nearing et al., 2004; Osman, 2014). With erosion rates often exceeding soil formation rates (Alewell et al., 2015; FAO and ITPS, 2015), it is critical to understand the conditions and processes governing soil erosion to increase sustainable use of this valuable resource.

1.2 Soil Erosion in Alpine Regions

The Alps are a mountain range arching across eight different European countries with a wide variety of climate regions, geological settings and environmental conditions. Approximately 20 % of the total Alpine range is located within Switzerland, which in turn covers 60 % of the Swiss territory (EDA, 2021; FSO, 2013). A high diversity of landscapes, soils and vegetation characterise the environmentally sensitive Alps (FAO and ITPS, 2015). The dominant land use is grassland (man-made below the tree line) mainly used for pastures or meadows (FSO, 2013; Fischer et al., 2008).

Alpine soils are susceptible to erosion processes due to the prevailing topographic conditions as well as the inherent fragility of the soils (Alewell et al., 2015; Egli and Poulenard, 2017; Meusburger and Alewell, 2014). In addition to the steep terrain, the climatological conditions in the Alps can further increase susceptibility to soil erosion (Egli and Poulenard, 2017; Meusburger and Alewell, 2014). Soil erosion can be triggered by events such as strong or prolonged precipitation or processes related to frost and snow cover (e.g., freezing-thawing cycles, snow gliding, gliding, avalanches, snow melt). Climate change is expected to strongly affect mountain regions, with increasing temperatures, changing precipitation patterns and related effects on flooding, drought or snow cover (Gobiet et al., 2014). As such, erosion triggering conditions may likely increase in the future (CH2018, 2018; Egli and Poulenard, 2017; Gianinetto et al., 2020; Meusburger and Alewell, 2008). Moreover, anthropogenic land-use change such as intensification or land abandonment further increase the risk of soil erosion (Egli and Poulenard, 2017; Geitner et al., 2017; Newesely et al., 2000; Meusburger and Alewell, 2008;

Tasser et al., 2003, 2005; Wiegand and Geitner, 2010b). The abandonment of difficult to access areas leads to a reduction in biodiversity, which in turn can decrease soil stability (Fischer et al., 2008; Pohl et al., 2009; Tasser et al., 2003). Simultaneously, easily accessible sites are more intensely used (Fischer et al., 2008; Meusburger and Alewell, 2008; Tasser et al., 2005; Wiegand and Geitner, 2010b). Anthropogenic activities, such as the operation of alpine ski runs, may cause additional damage to soils (Pintaldi et al., 2017) (Figure 1.1).

Figure 1.1: *Soil erosion in Alpine terrain caused by the operation of ski runs (Brienzer Rothorn, Canton Lucerne). The smaller slope on the right side of the image shows shallow erosion, which may have been caused by snow abrasion. Photo: R. Brogli 2018.*

The intensity of the land-use management and the condition of the vegetation cover strongly effect soil erosion rates (Alewell et al., 2015; Meusburger and Alewell, 2014; Poulenard and Podwojewski, 2004). A study by Alewell et al. (2015) for the Urseren Valley (Canton Uri) has shown, that grassland areas experience an average of 180 t km^{-2} year^{-1} of soil erosion, with measurements in intensely used grasslands (hot spots) of up to 600-3000 t km^{-2} year^{-1}. These values exceed the soil formation rates estimated for alpine areas with 54 ($\pm$14) to 113 ($\pm$30) t km^{-2} year^{-1} for older soils ($>$10–18 kyr) and 415 ($\pm$242) to 881 ($\pm$520) t km^{-2} year^{-1} for very young soils ($\leq$1 kyr) (Alewell et al., 2015). With such high erosion rates and expectations of increasing soil erosion it is crucial to better understand ongoing processes and develop tailored sustainable land management and governing strategies (Alewell et al., 2008; Geitner et al., 2017).

1.2.1 Soil Erosion Processes

During soil erosion processes, soil particles are displaced and transported downstream (FAO and ITPS, 2015). This loss of topsoil leads to a reduction in soil quality causing soil degradation. Soil erosion on mountain slopes can be caused by different processes, caused by wind, water or snow, gravitational processes, and anthropo-zoogenic influences (Apollo et al., 2018; FAO and ITPS, 2015; Lepeška, 2016; Pimentel, 2006; Wiegand and Geitner, 2010b). Often the processes leading to erosion are manifold and interlinked. This makes assigning a clear triggering cause to soil erosion sites difficult. In the following, the most common erosion forms investigated in this thesis are described.

Shallow Landslides

Shallow landslides can be described as patches with removed vegetation cover showing bare soil (Figure 1.2). These sites generally have a size of 2-200 m^2 (Schauer, 1975; Wiegand and Geitner, 2010b). Although relatively small, they often occur in groups and in some cases affect entire slopes (Wiegand and Geitner, 2010b; Zweifel et al., 2019). As the name suggests, these landslides are shallow and often only the top layers are removed. In extreme cases damage to infrastructure can be caused. Shallow landslides are caused by gravitational movement of the top layer and are often triggered by heavy and/or prolonged precipitation events (Guzzetti et al., 2008; Leonarduzzi et al., 2017). Additionally, trampling by cattle can cause surface tension cracks to form, which may lead to shallow landslides induced by this weakness (Geitner et al., 2021; Wiegand and Geitner, 2010b). Once bare soil patches have formed, they are susceptible to further erosion.

Another process driving soil erosion is snow gliding, which is the slow movement of the snow cover down-slope along the boundary between snow cover and vegetation cover (Blechschmidt, 1990; Höller, 2014; in der Gand, 1968). This can lead to the removal of the vegetation cover by abrasion, revealing bare soil patches. Furthermore, snow gliding can cause superficial damage, which can lead to shallow landslides forming at a later stage (Wiegand and Geitner, 2010b). While these bare soil sites differ to those of shallow landslides (Geitner et al., 2021), we are not able to distinguish between these erosion forms on aerial images, which are the basis for our studies. Therefore, we include shallow erosion caused by snow gliding in this category.

Figure 1.2: *Numerous shallow landslides on a grassland slope located in the Cation Uri, Switzerland. Photo: L. Zweifel 2018.*

Livestock Trails

Livestock trails are caused by trampling of cattle in pasture areas (Figure 1.3). These trails develop parallel to the slope contour lines, mainly in steep terrain, which are often used by cattle to traverse from one area to another. The heavy impact of the hooves damages the vegetation cover, displaces topsoil and subsequently leads to soil compaction. This reduces the infiltration capacity of the soil which also promotes overland flow of water (Apollo et al., 2018; Torresani et al., 2019; Yong-Zhong et al., 2005; Zhao et al., 2007). In some cases, livestock trails can act as an initiation point for further erosion, such as by snow gliding or landsliding (Sidle and Bogaard, 2016; Meusburger and Alewell, 2008; Geitner et al., 2021; Zweifel et al., 2019). On the other hand, livestock trails may also have stabilising effects due to the terracing structure of the slopes (Alewell et al., 2015; Tasser et al., 2003). In this case the structure increase surface roughness, which can reduce snow gliding and due to the fragmentation of the slope only smaller areas are removed (Tasser et al., 2003).

Figure 1.3: *Livestock trails located on a grassland slope near the Brienzer Rothorn (Canton Lucerne). Close to the valley bottom (centre of image) well established livestock trails can be observed. In the left upper corner shallow landslides have formed as a consequence of livestock trails. Photo: R. Brogli 2018.*

Sheet Erosion

Sheet erosion is the process of soil particle removal across a surface by rainwater impact and overland water flow (Smith and Wischmeier, 1957) (Figure 1.4). An intact vegetation cover can protect against erosion by reducing the water runoff and increasing water infiltration (Durán and Pleguezuelo, 2008). Therefore, a reduced or damaged vegetation cover is susceptible to sheet erosion, especially when occurring on slopes. Often the effects of this soil erosion process are not visible to the eye until already quite severe. A damaged vegetation cover or soil layer can be caused by overgrazing and trampling by cattle (O'Mara, 2012; Pimentel and Kounang, 1998; Torresani et al., 2019) or by climate effects (e.g.,

Figure 1.4: *Severe sheet erosion at an advanced stage on a grassland slope used for pasturing in the Canton Grisons, Switzerland. In the right lower corner livestock trails can be observed. Photo: L. Zweifel 2020.*

droughts or extreme rain events). With changing land-use practices (e.g., more intensely used pastures) this issue is enhanced.

During winter and early spring a reduced vegetation cover is present, which is why winter related erosion processes have a strong impact on sheet erosion rates (e.g., snow melt) (Konz et al., 2012; Meusburger and Alewell, 2008; Stanchi et al., 2014). Additionally, events such as severe droughts and strong precipitation events are likely to increase with climate change, which will further affect sheet erosion (Durán and Pleguezuelo, 2008; Gobiet et al., 2014).

Management Effects

The last category, which was observed during work on this project, are larger areas with reduced vegetation cover near the valley bottom with clear boundaries due to land use management to the surrounding vegetation (Figure 1.5). These areas are clearly caused by anthropogenic practices, such as the use of heavy machinery, over-fertilisation or cutting of grass before drought periods. Therefore, we define these areas as management effects (Zweifel et al., 2019). The erosion process that governs these areas is most likely mainly sheet erosion. However, these sites show a high temporal variability, as these areas (e.g., used for hay production) are often rotated (from year to year) and their occurrence is dependent on the seasonal land-use and damages are often relatively short-lived.

1.3 Soil Erosion Assessment

There are many different approaches that exist for measuring and assessing soil erosion processes. Field studies allow for observing and measuring soil erosion rates on smaller scales (e.g., plot-scale) as well as different time scales. Techniques range from classical sediment traps for shorter time

Figure 1.5: *Photograph showing the village Zumdorf (Urseren Valley, Canton Uri). Large patches of reduced vegetation cover (caused by management effects) can be observed in the upper left corner. Photo: Copyright © Swiss Department of Defence, Civil Protection and Sport DDPS.*

periods (e.g., one season) to chemical tracers for longer periods (e.g., fallout radionuclides ^{137}Cs, ^{210}Pb and $^{239+240}$Pu) (Alewell et al., 2014; Meusburger et al., 2014; Shakhashiro and Mabit, 2009). Measurements are in turn the basis for modelling techniques along with additional environmental parameters on different scales from local to global (Bezak et al., 2021; Borrelli et al., 2014, 2021). Erosion models may also be used in connection with climate and land-use scenarios (Märker et al., 2008). The up-to-date modelled erosion risk map for Switzerland was developed by Bircher et al. (2019) for arable lowlands and by Schmidt et al. (2018, 2019a,b) for grasslands surfaces and is based on the Revised Universal Soil Loss Equation (RUSLE) model.

Although there are many modelling approaches for soil erosion rates on different spatial and temporal scales, there is still a need for validation data sets for uncertainty assessment (Alewell et al., 2019; Borrelli et al., 2021). A step in this direction can be provided with erosion damage mapping (Fischer et al., 2018). This may be achieved with field observations, however the spatial scale and resolution of such observations are limited. Additionally, erosion sites are often inaccessible and the extent of eroded area is difficult to assess from the ground. Furthermore, gaining temporal information of these eroded sites is not possible. To overcome the issue of inaccessibility of steep terrain, remotely sensed data (e.g., aerial images, satellite images, UAV images) can be used, which offers a bird's-eye view. The rich data availability in Switzerland provides the possibility to conduct studies with high resolution data sets which cover the entire country (Swisstopo, 2020).

Mapping of eroded sites with remote sensing techniques often focus on one particular erosion process. One large area of research is the mapping of landslides, which can cause severe damage in various different areas of the world (Casagli et al., 2016; Guzzetti et al., 2012; Hölbling et al., 2015, 2016a; Martha et al., 2012; Mayr et al., 2016; Wiegand et al., 2013; Zhao and Lu, 2018; Zhong et al., 2020).

Another form of severe soil erosion is gully erosion caused by rainfall runoff, causing deep removal of soil along drainage paths. While this erosion form may not occur on Alpine grasslands, they severely affect many regions of the world and have increasingly been mapped and modelled using remote sensing techniques (Aber et al., 2019; Conoscenti et al., 2013; D'Oleire-Oltmanns et al., 2012; Johansen et al., 2012; Pérez, 2017; Shruthi et al., 2015; Vrieling et al., 2007; Zakerinejad and Märker, 2015).

During earlier stages of mapping with remote sensing techniques, pixel-based methods were common. As spatial resolutions of images increased (aerial, satellite, and UAV imagery), the focus shifted from pixel-wise mapping to object-based mapping (Blaschke and Strobl, 2001; Blaschke et al., 2014). This approach is named Object-based Image Analysis (OBIA) and became state-of-the-art for environmental applications in the 2000s and 2010s (Blaschke, 2015). When using OBIA, multiple pixels with similar properties are combined and defined as an *object*. OBIA has the advantage of producing objects with corresponding information based on spectral, spatial, textural and contextual properties (Blaschke, 2010; Martha et al., 2010, 2012; Stumpf and Kerle, 2011). This additional information can be used to classify the defined objects and has increased mapping accuracies. While the OBIA approach is flexible and adaptable to different aerial image conditions, the requirement of manual adjustments decreases the level of automation.

During the last years image segmentation using machine learning approaches such as *deep learning* have become increasingly popular for remote sensing tasks, as these approaches are often better equipped to handle large amounts of data in an efficient manner with a high degree of automation (Chen et al., 2018; Li et al., 2018; Ma et al., 2019; Mboga et al., 2019; Parente et al., 2019; Prakash et al., 2020; Yuan et al., 2020; Zhang et al., 2016; Zhu et al., 2017). While there are many different algorithms that can be applied, a popular approach in remote sensing is based on semantic segmentation (Chen et al., 2018; Ma et al., 2019). By performing semantic segmentation we are able to identify the location of objects by assigning class probabilities to each pixel located on an input image. This can be achieved by using convolutional neural networks (CNNs, Krizhevsky et al. (2012)), which are able to reduce the amount of information contained on input images to the most important features. In the context of this work, we apply the *U-Net* architecture (named after the shape of the workflow structure) which was developed by Ronneberger et al. (2015), who also demonstrated, that the U-Net requires less training data compared to other similar approaches (Flood et al., 2019). Once this algorithm has been trained with the target classes of interest (in our case different soil erosion classes), new images can be swiftly classified. During the prediction stage of the algorithm, a specific class probability is assigned to each pixel present on the image (Chen et al., 2016). However, such models based on deep learning require high quality data sets (i.e., boundaries of features) for training, which can be a limiting factor for many mapping tasks in natural environments (Chen et al., 2018; Samarin et al., 2020).

1.4 Goal and Outline of the Thesis

With the availability of high-quality data sets and the technical advancements in regard to environmental mapping, the aim of this thesis is the following: to develop an efficient monitoring tool to capture both the locations as well as the extent of all visible soil erosion processes on Alpine grasslands. By mapping both larger and smaller scale erosion sites at multiple time steps, an understanding can be developed for the spatio-temporal development of erosion sites.

The high quality of data sets available for Switzerland offers an excellent foundation for research based on remote sensing techniques. From an aerial perspective, most soil erosion processes on grassland can be observed (i.e., on aerial imagery). We differentiate between different processes and triggering factors and work with the erosion classes *shallow landslides*, *livestock trails*, *sheet erosion* and *management effects*, which are described in detail in Section 1.2.1. By differentiating between erosion processes crucial information is gained which allows for better decision making on land use mitigation by authorities of local to national scale.

The first study presented in Chapter 2 is published as Zweifel et al. (2019). In this study we identified and mapped soil erosion sites for the Urseren Valley (Canton Uri, Switzerland). For this purpose, Object-based Image Analysis (OBIA) was applied to five different aerial images across a 16-year period (2000–2016). The focus of this study was to identify the patterns of the different erosion classes and to develop a workflow with OBIA to distinguish between these classes. By mapping multiple aerial images at different time steps we were able to analyse the development of these erosion classes over both space and time.

While the mapping approach based on OBIA yields very accurate results, the method cannot be transferred to other regions in an efficient manner due to various constraints (e.g., computational time, adaptations to regional conditions, intensive requirement of additional manual procedures). However, with the overarching goal of understanding soil erosion processes on larger scales, a monitoring tool was developed which can simultaneously profit from the accurate results produced with OBIA but also overcome the constraints of the OBIA workflow. A deep learning approach was taken, which is described in detail in Chapter 3. This work was conducted in close collaboration with the Department of Computer Science and is published as Samarin et al. (2020). The mapped erosion sites from the first study (results of Chapter 2) serve as the basis (training data) for the deep learning approach. We prove that this method is capable of fulfilling the requirements of a reliable soil erosion monitoring tool in terms of accuracy, efficiency and automation.

In Chapter 4 the erosion monitoring tool is used to map shallow landslides in ten different study mountain across Switzerland. The study sites are located in mountainous terrain of the Jura mountains, the foothill regions of the Alps as well as in different regions of the Alps. The shallow landslides are statistically evaluated to identify their most important causal factors. The same set of explanatory variables are used for the statistical evaluations of all sites, which show varying levels of success depending on the location of the study site and orientation of the main valley axis. This study has been published as Zweifel et al. (2021).

Another major cause for soil erosion in mountain terrain is the process of snow gliding. In Chapter 5 the preliminary results are presented of a study investigating this process. Originally, the effects of snow gliding on soil erosion were going to be examined in Chapter 4 but was then expanded to its own study, which will be completed in the near future. The preliminary results show the relationship of snow glide distances to mapped shallow landslides. For this purpose, a spatial snow glide model was calculated for Switzerland. The mapped shallow landslides were used to evaluate, whether higher modelled snow glide distances correlate with higher shallow landslide densities.

In Chapter 6 the conclusions of this thesis are presented and an outlook is given in Chapter 6.3.

Val Piora, Ticino
Photo: Lauren Zweifel

2

Spatio-Temporal Pattern of Soil Degradation in a Swiss Alpine Grassland Catchment

Abstract

Soil degradation on Alpine grasslands is triggered mainly by extreme topography, prevailing climate conditions and land use practices. Suitable monitoring tools are required to assess soil erosion with high temporal and spatial resolution. In this study, we present an unprecedented and comprehensive approach based on Object-based Image Analysis (OBIA) to map and assess all occurring erosion processes within a catchment (Urseren Valley, Switzerland). Five high-resolution (0.25-0.5 m) orthophotos with RGB spectral information (SwissImage) produced during a 16-yr period were analyzed. Soil erosion sites are classified according to their type (shallow landslide or sites with reduced vegetation cover affected by sheet erosion) or the triggering land use management impacts (haying, trampling) with the Overall Accuracy ranging between 78 and 88% (Kappa 0.65 – 0.81) for the different years. The area affected by soil erosion increases for all classes during the study period (2000 – 2016) by a total of 156% $\pm$ 18% (consisting of 3% shallow landslides, 5% livestock trails, 46% sheet erosion and 46% management effects). Slopes at lower elevations ($<$ 1800 m asl) are increasingly affected by livestock trails and sheet erosion caused by trampling and grazing as well as other management practices. For areas located above the agricultural land use, an increase in shallow landslides, as well as sheet erosion, can be observed. This points to climate change as a triggering factor of soil degradation, which has not been identified so far as a factor for soil erosion in the Urseren Valley. While OBIA yields conservative estimations mainly due to limitations of spatial resolutions, the method facilitates a comprehensive overview of the ongoing temporal and spatial development regarding soil degradation within the Urseren Valley.

2.1 Introduction

Alpine grasslands can be strongly affected by various types of soil erosion triggered by wind, water, snow, gravity and management impacts (e.g., trampling). Future climate change is expected to have a strong impact on the Alpine region causing not only an increase in temperature but also a change in frequency and intensity of precipitation events as well as strongly altered snow dynamics (Beniston, 2006, 2012; CH2011, 2011; Frei et al., 2018; CH2018, 2018). Along with changing land use practices,

Study published as Zweifel, L., Meusburger, K., Alewell, C., 2019. *Spatio-temporal pattern of soil degradation in a Swiss Alpine grassland catchment.* Remote Sens. Environ. 235, 111441.

such as intensified use of pastures, these changes are expected to have an increasing effect on the soil erosion rates in Alpine regions (Bosco et al., 2009; Meusburger and Alewell, 2008, 2009; Scheurer et al., 2009). Certain Alpine regions already experience high rates of soil erosion (e.g., average erosion rate of 180 $t\ km^{-2}\ yr^{-1}$ with maximum in erosional hot spots of 3000 $t\ km^{-2}\ year^{-1}$ in the Urseren Valley) and thereby exceed Alpine soil production rates (for old soils between 54 $t\ km^{-2}\ yr^{-1}$ and 113 $t\ km^{-2}\ yr^{-1}$, for young soils between 119 $t\ km^{-2}\ yr^{-1}$ and 248 $t\ km^{-2}\ yr^{-1}$)(Alewell et al., 2015). In combination with the extreme prevailing topographic and climate conditions, the land use can be considered unsustainable (Meusburger and Alewell, 2014). The main types of erosion processes occurring in our study area (Urseren Valley, Central Swiss Alps) are landslides, sheet erosion (e.g., rill and inter-rill erosion), livestock trails and damages due to management (i.e., haying, use of heavy machinery, over-fertilisation). We separate livestock trails from other management effects due to the very different appearances, triggering factors and distribution in the catchment.

Shallow landslides typically have a size of $2-200\ m^2$ and occur when a triggering event, such as heavy and prolonged precipitation or movement of the snow cover displaces the topsoil layer (Ceaglio et al., 2012; Wiegand and Geitner, 2010a,b). In many cases it is a combination of both triggers which eventually lead to landslides (e.g., disturbance of surface stability by the snow, then water saturation with heavy rain events). These areas continue to be exposed to further erosion by wind and water and might take years to decades to re-vegetate or might even steadily increase. While shallow landslides are a naturally occurring phenomenon, pasture management (e.g., trampling by livestock, stocking density) can have a destabilizing effect, increasing the local susceptibility to landslides (Maag et al., 2001; Meusburger and Alewell, 2008; Schauer, 1975; Tasser and Tappeiner, 2002). Sheet erosion is the result of surface run-off and the consequent detachment and displacement of topsoil particles down slope (Alewell et al., 2019; Nearing et al., 2017). Sheet erosion can affect large areas and occur for long periods of time before being noticed. Livestock trails are the direct result of trampling by livestock, when the vegetation cover has not enough time for recovery and the soil is compacted (Apollo et al., 2018). These trails mainly develop in pasture areas following the contour lines of the slope, when livestock traverse steep areas. The reduction of vegetation cover through trampling and overgrazing can increase sheet erosion.

Scientific communities working on the different phenomena of soil erosion are often separated due to the varying methods applied to capture these erosion processes (e.g., field measurements, mapping, modelling or tracer techniques). However, erosion processes interact and boundaries are not clear between the processes and may be overlapping. Local authorities need information on the overall soil degradation situation, which is impossible to achieve from surveys at ground level in the field. Here, remote sensing offers the opportunity to observe and monitor different erosion processes at high spatial resolutions. This might set the methodological framework to study spatio-temporal auto-correlation between different erosion processes and will extend the study of susceptibility mapping beyond landslides to other processes of soil degradation.

All above mentioned erosion processes can be observed on high-resolution orthophotos (Figure 2.1). While many changes have occurred over the course of 16 years, such as the general vegetation cover (e.g., reduction of shrubs), an increase in bare soil sites as well as a reduction of the vegetation cover in certain areas is evident. A photograph taken in 2009 shows the severity of these erosion features in the field (Figure 2). As Object-based Image Analysis (OBIA) has proven to be a reliable tool for many difficult detection tasks in the field of remote sensing, especially in the case of high-resolution images (pixel size $<$ object size) (Blaschke, 2010; Chen et al., 2018), our hypothesis is, that in spite of very different color ranges and brightness between photos, temporal development of degradation features can be mapped.

When applying this semi-automated method, the pixels of remotely sensed images are first grouped into segments producing image objects containing pixels with similar spectral properties. The image objects are then classified based on the information associated with the objects, such as spectral, spatial, textural or contextual properties (Martha et al., 2010, 2012; Stumpf and Kerle, 2011). In the case of soil erosion, OBIA has been extensively used to map landslides on satellite images, mainly with the aim of producing landslide inventory maps (Eisank et al., 2014; Guzzetti et al., 2012; Hölbling et al., 2015, 2016a, 2017; Martha et al., 2012; Mayr et al., 2016; Stumpf and Kerle, 2011; Wiegand et al., 2013). In some studies, aerial images were used for mapping purposes instead of or in addition to satellite images (Hölbling et al., 2016a,b; Moine et al., 2009). Other applications of OBIA for capturing soil erosion consist of rill and gully erosion mapping (D'Oleire-Oltmanns et al., 2014; Johansen et al., 2012; Karami et al., 2015; Shruthi et al., 2011, 2014, 2015). Gully erosion is not assessed in this study, as it does not occur on grassland in our catchment, but might be captured with the technique in other areas.

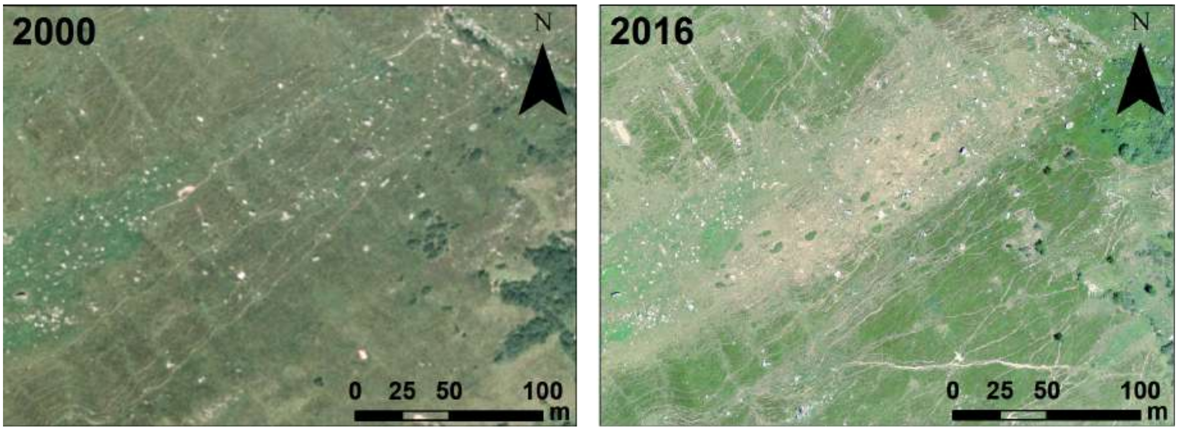

Figure 2.1: *Sub-image from the orthophotos of the Urseren Valley. The side by side comparison of the images taken in 2000 and 2016 show the increasing amount of soil degradation over time.*

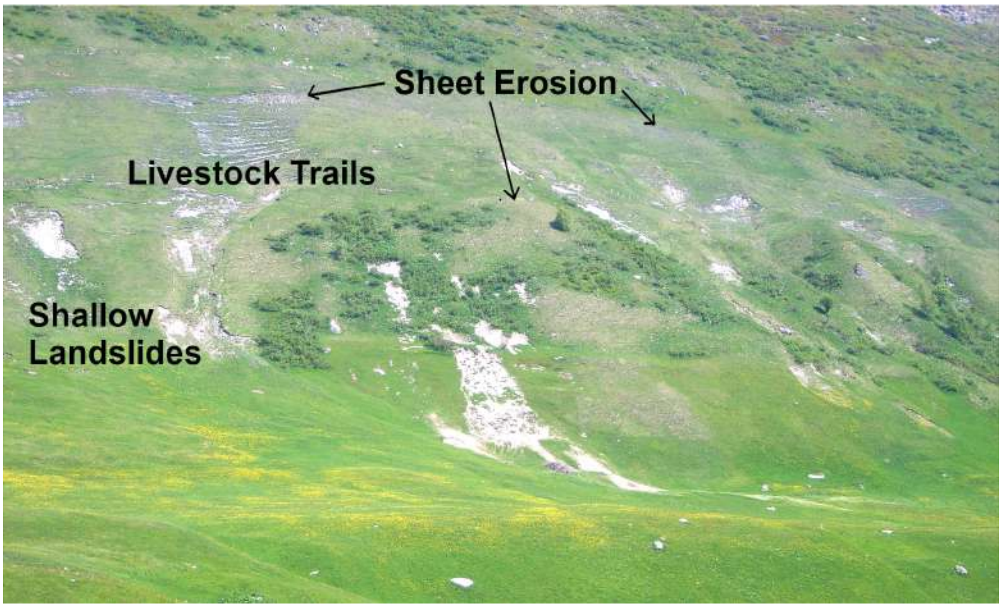

Figure 2.2: *Photograph from the Urseren valley showing different erosion processes (examples of landslides, livestock trails and sheet erosion are labeled). The image was taken in early summer of 2009.*

While the different scientific communities have been using OBIA to map erosion features with distinct boundaries (e.g., gullies, landslides), no study known to the authors has been conducted on mapping all occurring erosion processes including diffuse boundaries (e.g., sheet erosion) in a single approach for Alpine grasslands. With this study we present a holistic approach using OBIA to identify all visible occurring processes causing soil loss on Alpine grasslands (Urseren Valley) on high-resolution RGB orthophotos. In many cases the transitions between different types of erosion processes are not distinct, but for this study we assign classes to eroded and degraded sites according to their leading erosion type or process (shallow landslides, sheet erosion) and erosion caused by land use management (livestock trails, management effects) with a set of rules defined in Section 2.3.2 based on typical visual characteristics of the classes, such as spectral properties or geometric attributes.

By mapping multiple orthophotos (2000 – 2016) we aim at a time series that allows for a comprehensive analysis in space and time of all the erosion processes. Spatio-temporal maps will give us valuable insights into the erosion dynamics of the catchment including even small scale erosion features, which is crucial information for sustainable land management (Alewell et al., 2008).

2.2 Study Site

The selected study site is located in the high-alpine Urseren Valley (Figure 2.3) in the Swiss Central Alps (Canton Uri) and covers an area of 26 km^2. The valley has a mean slope angle of 27° and is discharged by the river Reuss. With elevations between 1400 and 3200 *m asl* the valley is exposed to subalpine-alpine climate conditions. The mean annual temperature of the nearest station (Andermatt, 1438 *m asl*) is 4.0 °*C* (period 1981 to 2011) and the mean annual rainfall is 1400 *mm* (max. in October, min. in February). On average, the maximum yearly precipitation intensity is 110 $mm/3d$ with values ranging up to 270 $mm/3d$ in the year 2000 (Source MeteoSwiss). The valley is covered with snow from November until April (mean seasonal snow depth of 60 *cm*) with a maximum in March (mean snow depth of 95 *cm*) (Source MeteoSwiss). While the run-off is dominated by snow melt from May until June (max. in June), summer and autumn floods can also be major contributors to the flow regime.

The orientation of the U-shaped valley is NE–SW and is situated along a tectonic fault line separating Gneiss of the Gotthard massif on the south and Granite of the Aare massif on the north (crystalline basement called “Altkristallin”, (Labhart, 1999)). Along the fault line there are vertically dipping layers consisting of Permacarbonic (sandy-clay deposits) and Mesozoic sediments. The latter consists of different material depositions from the Triassic period (sandstone, rauhwacke and dolomite), early Jurassic period (“Lias”; dark clay-marl and marl) as well as from middle Jurassic period (“Dogger”; clays, marl and limestone). During orogenesis, the material was metamorphosed to schist (Angehrn, 1996; Wyss, 1986; Kägi, 1973). The south-east facing slope contains clay-rich soils produced by weathering of the calcareous bedrock which provide a high risk for slope instabilities. The prevailing soil types in the Urseren Valley are Podzols and Cambisols (after IUSS Working Group WRB (2006)). Leptosols are common on steep slopes and on elevations above 2000 *m asl* (with Rendzic Leptosols on calcareous substrate). At the valley bottom clayey Gleyic Luvisols and Gleysols can be found. Due to the deforestation of the valley, started by early settlers in 1100 A.D., the slope instability is high, avalanches are frequent and therefore an increased susceptibility to soil erosion is present (Ceaglio et al., 2012; Freppaz et al., 2010; Korup and Rixen, 2014; Stanchi et al., 2014). The potential tree line is located at approximately 2150 *m asl* (C. Körner, personal communications). The south-east facing slope is mainly covered with grassland and is generally more productive due to the geological bedrock and therefore is more intensely used for pasturing. The north-west facing slope is less productive and

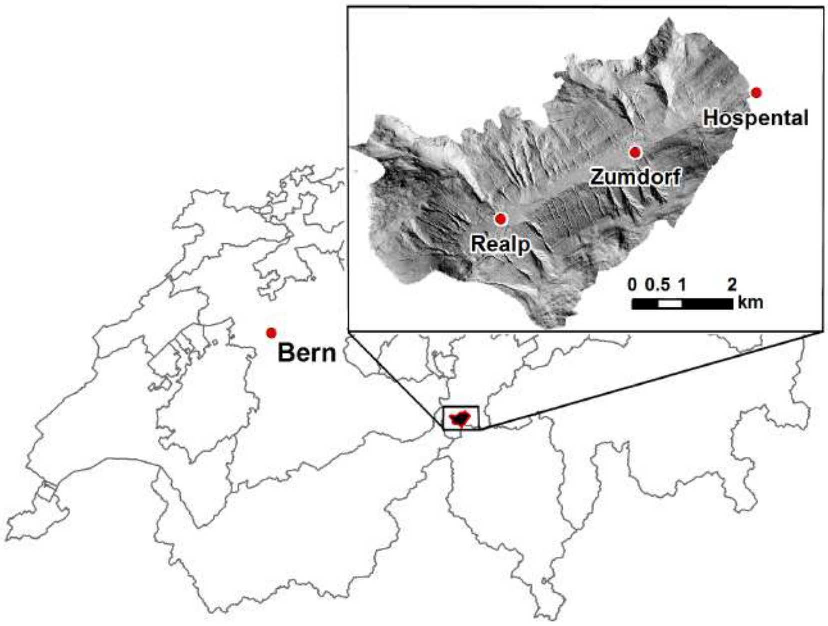

Figure 2.3: *The Urseren Valley and its location within Switzerland.*

covered with shrubs, mainly *Alnus viridis*. Livestock consists primarily of cattle and sheep with a small number of goats. With an increasing number of livestock the stocking density increased over time, causing more intense use of grassland pastures. For more details on the history of the land use in the Urseren Valley see Meusburger and Alewell (2008).

2.3 Materials & Methods

2.3.1 Materials

Orthophotos

Orthophotos (*SwissImage*) are georeferenced aerial images produced by Swisstopo (Swisstopo, 2010) that have been corrected for the influence of the terrain and of the camera. This product covers the entire area of Switzerland and is updated every three years during the vegetated season. The images contain the visible spectral bands red, green and blue (RGB) and have a ground sample distance (GSD) of 0.5 *m* for older images and 0.25 *m* for newer images (see Table 2.1 for details). We used the CORINE land cover data set (EEA, 2006) (spatial resolution of 100 *m*) to crop the orthophotos according to the presence of grasslands in the Urseren Valley. Due to the coarse resolution of the CORINE data set precise delineation of grassland areas is not possible, however, large areas containing high alpine rock fields can successfully be excluded.

Additional Data Sets

The digital terrain model (DTM) *SwissALTI3D* (Swisstopo, 2014) has a spatial resolution of 2 *m*. Using ArcGIS (Version 10.5) we calculated the slope, aspect and standard curvature (plan and profile) from the DTM, which yield important ancillary information for the classification process. We also

Table 2.1: *Orthophoto acquisition dates and specifications.*

Year	Date	GSD	Position Accuracy
2000	24. August	0.5 m	± 0.5 m
2004	09. September	0.5 m	± 0.5 m
2010	20. July	0.25 m	± 0.25 m
2013	01. August	0.25 m	± 0.25 m
2016	20. July	0.25 m	± 0.25 m

calculated the Excess Green index (ExG), which is a vegetation index that can be calculated from only visible spectral bands (Woebbecke et al., 1995; Mayr et al., 2016) and is calculated as follows:

$$ExG = 2g - r - b,$$

where

$$r = \frac{R}{R+G+B}, \quad g = \frac{G}{R+G+B}, \quad b = \frac{B}{R+G+B}.$$

Furthermore, thematic data sets (taken from the topographic landscape model *SwissTLM3D* (Swisstopo, 2019)) containing information on the presence of roads, rivers/streams and buildings were used to refine the rule set. All above mentioned data sets are listed in Table 2.2.

Table 2.2: *List of data sets used for the Object-based Image Analysis.*

Product	Description	Type	Spatial Res.
SwissImage	Orthophotos (RGB)	Ras.	0.25 – 0.5 m
SwissALTI3D	Digital Terrain Model; Calc. Derivatives	Ras.	2 m
SwissTLM3D	Thematic Layers: Roads, Streams, Buildings	Vec.	1 : 25’000
CORINE	Land Cover (Grasslands)	Ras.	100 m

2.3.2 Erosion Mapping with Object-based Image Analysis

To identify and map the degraded sites on the orthophotos we used OBIA. The work-flow was developed with the software *eCognition Developer* (Version 9.3.2) (Figure 2.4). As a first step, object primitives are generated by grouping together pixels with similar properties (1). For the generation of the object primitives, the multi-resolution segmentation algorithm of eCognition was used (scale parameter = 40, shape = 0.1, compactness = 0.5). The segmentation takes into account the heterogeneity of pixel values (RGB) as well as the size of the desired image objects. Additionally, the DTM and its derivatives as well as the calculated ExG index were incorporated during the segmentation process. Parameters were calibrated manually, while care was taken to achieve object primitives that best represent our target objects, which show a strong variation concerning their shape as well as size.

The orthophotos of the catchment were divided into four sub-sections to better handle the data load (above and below 2000 *m asl* as well as south and north of the river). In a next step, a manually calibrated ExG index threshold was applied to classify all objects belonging to the class vegetation (2). ExG thresholds varied from one orthophoto to the next, however, ideal values were well defined.

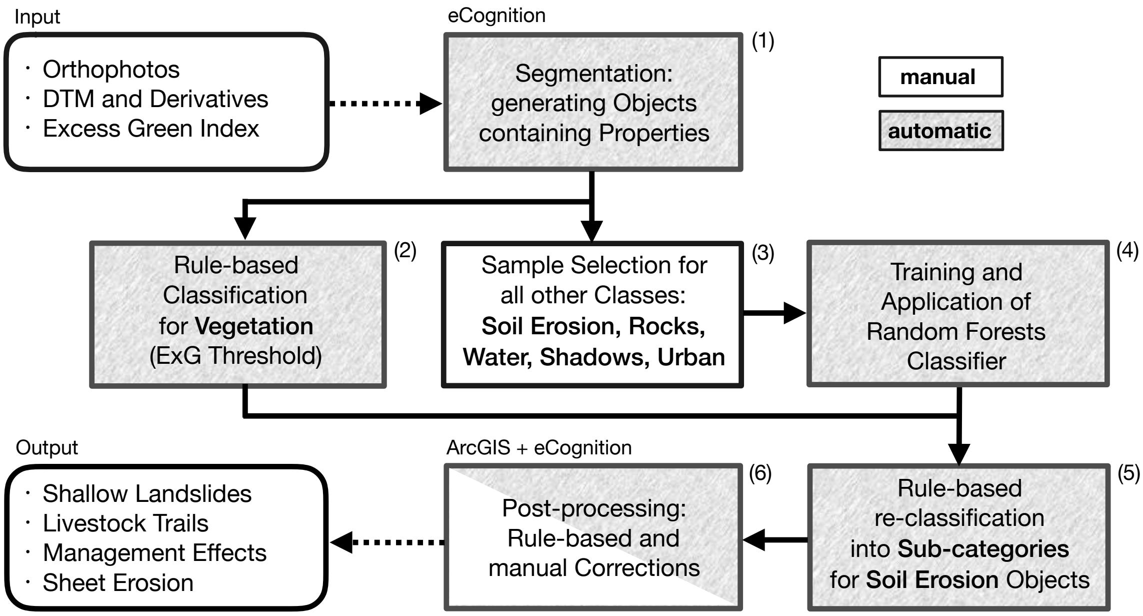

Figure 2.4: *Work-flow diagram of the Object-based Image Analysis used to map and classify visible soil erosion features. Steps that require manual work are described in white boxes, while automatic steps are described in grey boxes. Numbered steps are further described in the text with (1)–(6).*

Table 2.3: *List of object features used for the random forest classifier.*

		Object Features
Layer Values	Mean	R, G, B, ExG, Elevation, Aspect, Slope, Curvature, Hue, Intensity, Saturation, Brightness
	Std. Dev.	R, G, B, ExG, Elevation, Aspect, Slope, Curvature
	Border Contrast	ExG
Geometry	Extent	Area, Length/Width
	Shape	Compactness, Density, Elliptic fit, Roundness, Rectangular fit, Shape Index
Texture	GLCM (all dir.)	Contrast, Dissimilarity, Entropy, Mean, Std. Dev., Correlation

For all other unclassified objects, samples were selected to represent their class (soil erosion, rocks, shadow, water, roads or buildings) (3). For every orthophoto roughly 3% of all objects were manually selected as samples across the entire area. Approximately 30% of the samples were selected to represent the class *soil erosion*, as this class contains bare soil areas as well as patches with strongly reduced vegetation cover, which exhibits a wide variety of appearances. The selected samples were used to train the random forest classifier based on the object features listed in Table 2.3 to classify all remaining unclassified objects (4). For the random forest classifier, which was applied within eCognition, we selected all 36 predictors (Table 2.3), with 6 features considered per split with a tree size of 6 and a maximum tree number of 50, which offered the best trade-off between calculation time and classification performance. The object features used for the random forest classifier (Table 2.3) were selected from the point of view of differentiating soil erosion objects from all other objects (e.g. rocks, water, urban). Features consist of various layer values derived from the orthophoto, the ExG index, the DTM and its derivatives as well as geometric variables and object textural variables from the

Grey Level Co-occurrence Matrix (GLCM) (Haralick et al., 1973) and were chosen based on literature (Martha et al., 2010; Moine et al., 2009; Stumpf and Kerle, 2011) and testing of further features within eCognition. Information on the feature importance results of the random forest classifier can be found in the supplementary material (Figure S1). At this stage, the random forest classifier has classified objects belonging to the class soil erosion. To allocate the specific erosion sub-categories to the soil erosion objects we created an additional rule set based on the visual appearance of the four sub-categories, described in detail below. For the differentiation between the categories we translated the visual characteristics in to suitable object features and calibrated thresholds (Table A.1; for more details see Table S1 in the supplemental material) (5). We distinguish between erosion classes, that are clearly identifiable with distinct boundaries, namely shallow landslides, livestock trails and management effects. For sites with reduced vegetation cover and diffuse boundaries we assume sheet erosion to be the dominant erosion process.

Shallow landslides are distinguished by their clear boundary to the surrounding vegetation as well as their relatively compact shape and occurrence on steeper slopes ($> 25°$) (Meusburger and Alewell, 2008; Wiegand and Geitner, 2013). Livestock trails, on the other hand, are very uniquely elongated and narrow and follow the contour lines of the slope within a range of $\pm$ 20°. Management impacted grasslands are typically large, compact areas with distinct boundaries (e.g., within fences or ownership boundaries) and are found near the valley floor on gentle slopes ($< 25°$) easily accessed with machinery. Remaining objects are classified as areas with reduced vegetation cover susceptible to sheet erosion, as it is difficult to determine a certain pattern, due to the various shapes, sizes and locations of this type of erosion process.

Table 2.4: *List of object features used in the rule set to define soil erosion categories.*

Erosion Category	Object Features
Shallow Landslides	Mean Slope, Border Contrast of ExG, Shape Index, Rel. Border to Class ‘Vegetation’
Livestock Trails	Length/Width, Density, Main Direction
Management Effects	Area, Mean Slope
Sheet Erosion	Remaining ‘Soil Erosion’ Objects

Post-processing in the form of visual assessment and subsequent manual corrections of the results was required to assure the comparability of the erosion classes between the individual years (6) (Figure 2.5). Objects with an area $< 4\ m^2$ were removed from all results to assure conformity between all years, due to the varying GSD or the orthophotos.

2.3.3 Verification

For all erosion classes we conducted a thorough visual investigation with zooming in to the respective orthophotos to assure the accuracy of the classification results as well as an accuracy assessment of randomly selected points. The latter was conducted with five soil experts familiar with the field situation in the valley. Each expert evaluated 100 random points for each orthophoto, generating a total of 500 points per expert. Approximately half the sample points were randomly selected from the class background and the other half from erosion classes, to best evaluate the overall accuracy of erosion classes, which occur rarely compared to background pixels. The randomly chosen pixels were independently reviewed through visual assessment and were allocated by the experts to the following

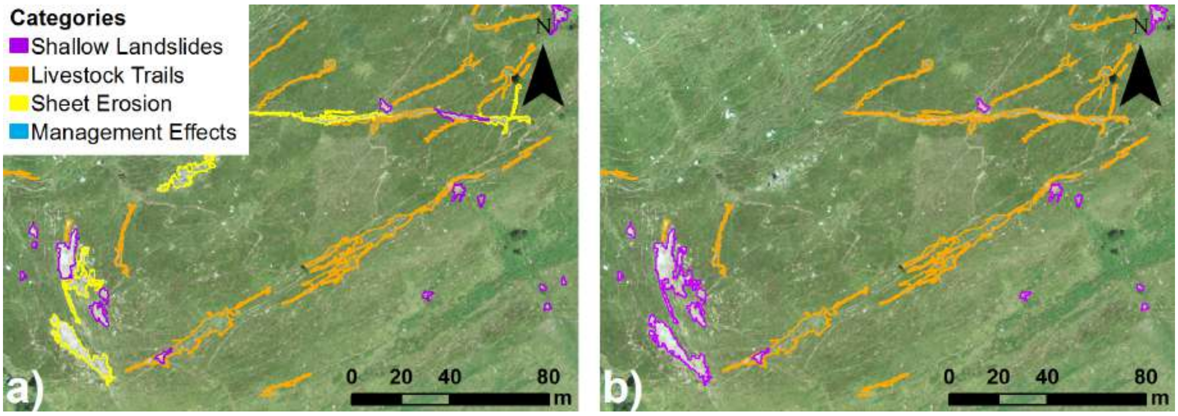

Figure 2.5: *A subarea of the Urseren Valley (2013) showing an example of classification results a) before and b) after manual corrections.*

classes: shallow landslides, livestock trails, sheet erosion, management effects or background (anything other than soil erosion). These results were then compared to the results of OBIA to calculate accuracy scores for each mapped orthophoto. The accuracy was assessed based on the error matrix and the related statistics, namely the Overall Accuracy, Producer's Accuracy, User's Accuracy and Kappa coefficient (Radoux and Bogaert, 2017).

Additionally, we calculated accuracy scores for shallow landslides for the two years (2000 and 2004) overlapping with the manually mapped landslides from the previous study by Meusburger and Alewell (2008) (only sites $> 10\ m^2$ to guarantee comparability). Verification with field measurements was only possible with a limited selection of random sites, due to the large extent of the study area. Due to the extreme topography and the fact that field measurements were conducted 2 years after the newest orthophoto was taken (2016), the choice of suitable erosion sites was limited. While the location and the extent of shallow landslides can clearly be determined in the field it was not possible to determine the exact boundaries of the other erosion features two years later. For the mapped shallow landslides, field measurements of ten sites were compared to the length and width of the objects generated with OBIA. The measurements of the OBIA mapped landslides were corrected for the steepness of the slope to guarantee comparability.

2.4 Results & Discussion

2.4.1 Spatial distribution of mapped erosion sites

Mapping of the orthophoto taken in 2016 resulted in 3.4 % of the valley surface being affected by some type of erosion process (Figure 2.6). Examples of the four erosion classes and their appearance on orthophotos can be seen on Figure 2.7. The south-east facing slope is more strongly affected by soil erosion and contains 92 % of all mapped sites. Concurrently, grassland is the dominant vegetation cover on this side of the valley. Most agricultural activity in the form of livestock grazing and haying takes place on the lower slopes of this side due to the higher fertility of the soil developed on calcareous and silicate schists, which in turn are prone to erosion. The grassland surface area in this land use zone ($<$ 2000 *m asl*) is affected by 6.8 %. The north-west facing slope, on the other hand, is mostly covered with shrub vegetation (*Alnus viridis*, *Sorbus aucuparia*), and is less favored for agricultural use (Meusburger and Alewell, 2008).

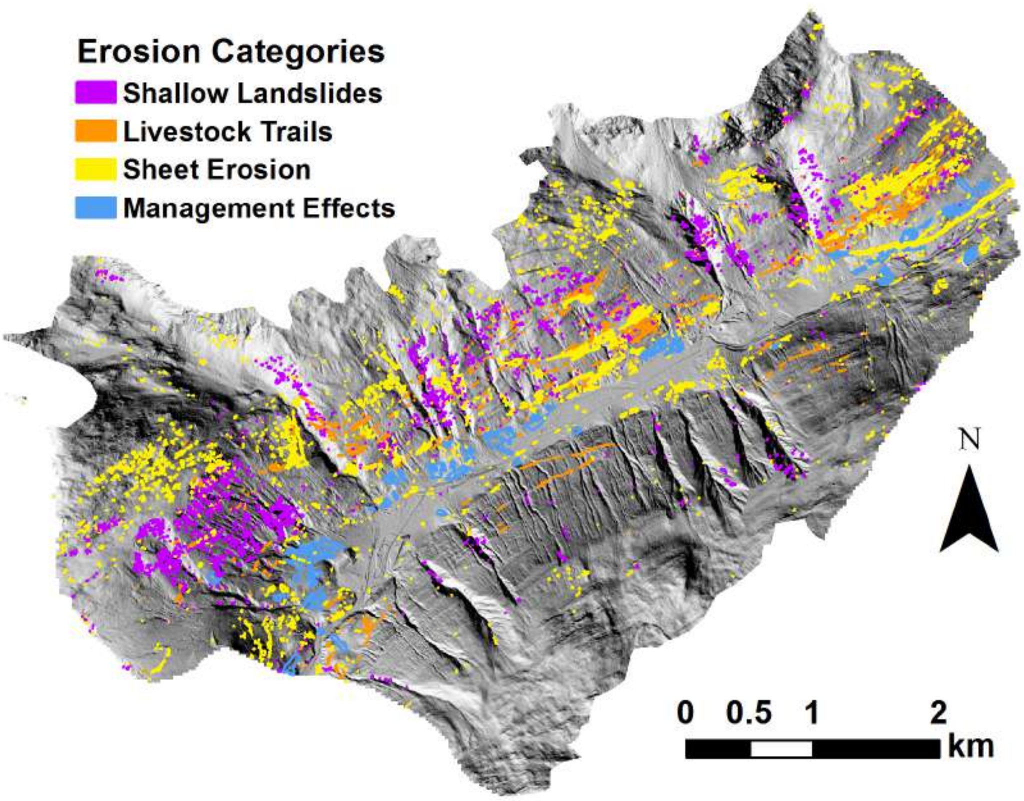

Figure 2.6: *The map shows the relief of the Urseren Valley with the OBIA mapped erosion sites based on the most recent orthophoto of 2016.*

Shallow landslides are commonly quite small with an average size of 40.2 m^2. They can, however, vary in size from very small (4 m^2) to 6172 m^2 for the largest site, which are located in steep terrain and caused by headward erosion of the stream. Most sites tend to be smaller but are often aggregated into groups, with 69.2% of landslides located within 10 *m* of each other. Additionally, landslide locations are often in close proximity to streams, with 49.4% within a distance of 100 *m*. The slope angles at which shallow landslides primarily occur, range from 33 to 44° with a mean of 39°, which agrees with other studies (Blechschmidt, 1990; Rickli and Graf, 2009; Tasser et al., 2003; Wiegand and Geitner, 2013). The elevation of slopes affected by shallow landslides ranges from 1769 to 2087 *m asl* with a

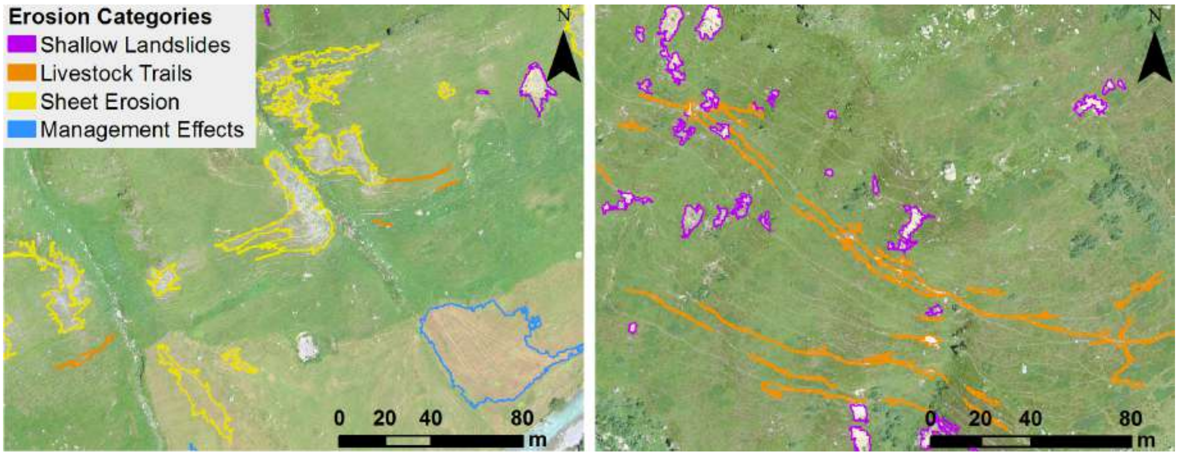

Figure 2.7: *Illustration of the different erosion types as they appear on the orthophoto (2016) and are subsequently mapped with OBIA.*

mean of 1931 *m asl*. The dominant slope aspects are east (43%) and south (41%) with fewer landslides located on western slopes (12%). These findings generally agree with studies conducted for other regions in the Alps, such as by Blechschmidt (1990) (Karwendel), Laatsch and Baum (1976) (Bavarian Alps) and Wiegand and Geitner (2013) (Tyrol). The south-east facing slope is exposed to more direct solar radiation and therefore experiences more snow-gliding events and enhanced snow-melt, which can trigger shallow landslides (Meusburger et al., 2013; Tasser et al., 2003; Wiegand and Geitner, 2013). Furthermore, snow-gliding is more easily triggered with wet boundary layer between the soil and snow cover, which is more likely given with warmer ground conditions (Fromm et al., 2018; Newesely et al., 2000).

Livestock trails generally follow the contour lines and occur on moderately steep slopes ($26-36°$), where cattle and sheep often traverse for grazing purposes. The average elevation of livestock trails is 1749 *m asl* and therefore are located close to the foot of the slope. There are, however, sites ranging up to 1834 *m asl*. The majority of livestock trails (85%) are found on the south-east facing side of the valley.

Sites with reduced vegetation cover caused by **management effects** are located near the foot of the slope (up to 1596*m asl*) and occur on gentler slope angles ($12-22°$). These areas are mostly used for hay production to feed livestock during winter months (Meusburger and Alewell, 2008).

Exposed soil surfaces susceptible to **sheet erosion** (from here on referred to only as *sheet erosion*), is a phenomenon that occurs across the entire catchment on all grassland surfaces. The triggering factors for these exposed soil surfaces are not consistent. Sheet erosion sites at lower elevations are mostly in the proximity of livestock trails and are therefore connected to land use practices. The sites at higher elevations are most likely caused by precipitation and snow movement or snow melt. The shapes and sizes of the sheet erosion objects vary greatly from only 5 m^2 up to 3 *ha* with a mean of 117 m^2. The average slope angles of affected sites range from 17 to 36° with a mean of 27°. Thus, sheet erosion is present on gentler as well as on steeper slopes.

2.4.2 Spatio-Temporal Development

Applying the OBIA method to historical orthophotos yields a time series with irregular frequencies starting from the year 2000. From 2000 until 2016 the measured area affected by soil erosion (sum of all four erosion categories) has increased by 156 % ± 18% (estimated propagated error based on accuracy assessment). This increase can be observed for all occurring erosion types with various intensities (Figure 2.8).

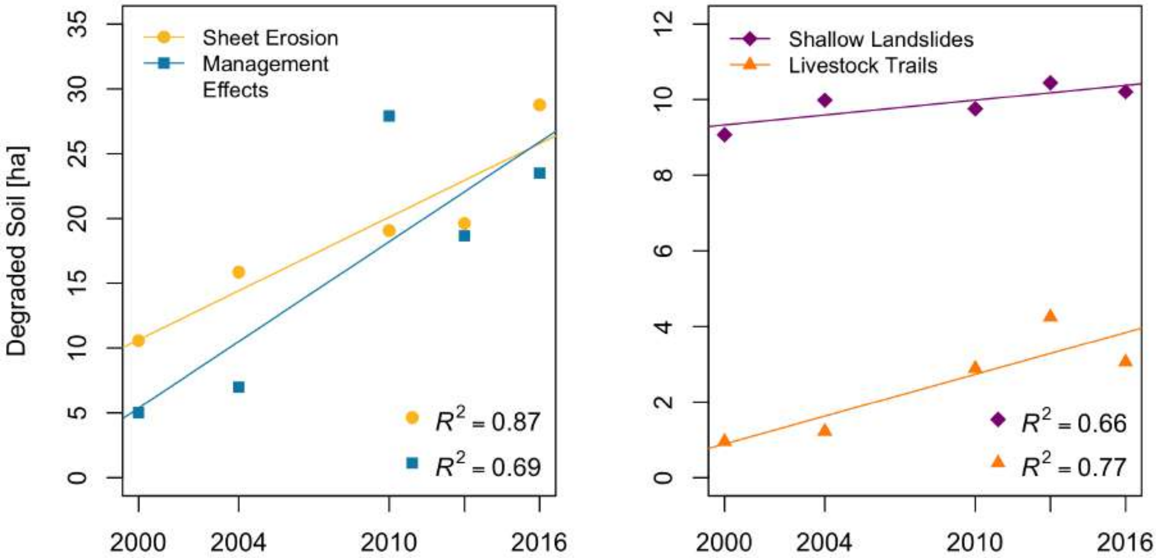

Figure 2.8: *Temporal development of all soil erosion classes in the Urseren Valley for each analyzed year between 2000 and 2016. Lines indicate the trend given by a linear regression.*

To achieve a more comprehensive understanding of the dynamic aspect of the erosion sites, we analyzed temporal and spatial changes simultaneously. Sheet erosion and management effects have increased substantially since 2000 (from 10.30 to 28.75 *ha* for sheet erosion and 4.06 to 23.49 *ha* for management effects) with management effects showing strong variations from 2010 to 2013. Shallow landslides and livestock trails both are generally smaller in size and also affect a smaller area. **Shallow landslides** show a constant but comparably small increase from 9.07 to 10.21 *ha* between 2000 and 2016. Meusburger and Alewell (2008) and Alewell et al. (2008) concluded that the amount of soil material eroded by landslides is considerably smaller than by sheet erosion. We can confirm regarding the areal effect that shallow landslides, even though being the most obvious erosion feature, are quantitatively not the dominant erosion process in the Urseren Valley. **Livestock trails** affect only a small area due to their narrow appearance but have, nevertheless, steadily increased during the investigation period (1.04 – 3.06 *ha*) with a peak in 2013 (4.25 *ha*). The decrease of livestock trails after 2013 is mainly due to the widening of the trails due to continuous trampling and grazing and/or climate effects which resulted in a shift into being classified as sheet erosion in 2016. The effect of livestock trails on erosion processes might be twofold. The horizontal structuring (e.g., “terracing") of the slopes can decrease the snow-gliding distance as well as the overland flow (Alewell et al., 2015; Tasser et al., 2003). Due to this fragmentation of the grassland surface in these areas only small parts of the topsoil are able to slide off (Tasser et al., 2003). On the other hand, due to the damaged vegetation cover and soil compaction caused by livestock trampling and grazing, shallow landslides and sheet erosion can be triggered more easily by winter processes (e.g., snow-melt or snow-gliding) and strong precipitation events / water saturation of soil (Alewell et al., 2015; Dommermuth, 1995; Konz et al., 2010; Tasser et al., 2003). Our results show, that areas highly affected by livestock trails lead to increased areas with reduced vegetation cover as well as landslides over time. As such, an increased amount of livestock trails can be a triggering factor for other erosion processes.

An overall increase in sites affected by **sheet erosion** is observed for the entire catchment. However, there is a high spatial variability observed in the results for the different orthophotos. This variability is due to the fact that these areas have a reduced vegetation cover, for which it is difficult to define clear boundaries. Especially in the case of very small degradation sites mapping precision as well as repeated detection on different orthophotos with differing color characteristics (e.g., solar angle, color tones) might be impaired. Additionally, having time steps of at least three years between the orthophotos allows for recovery of sheet erosion sites as well as the development of new sites. Areas that are permanently affected by sheet erosion are located at lower elevations in areas intensively used for pasturing.

The visual appearances of **management effects**, mainly caused by the use of heavy machinery or the application of manure at unsuitable times leaving the soil bare or the vegetation cover damaged, are very variable from one year to the next. Although the trend is generally increasing, possibly due to changing land use practices, the size of the affected area is very dependent on the timing of the orthophoto. In most cases these sites recover quickly, but in the meantime the exposed areas are vulnerable to erosion.

By dividing up the amount of eroded area in to elevation sections, we can observe the changes from 2000 to 2016 by erosion class (Figure 2.9). For livestock trails, sheet erosion and management effects the affected area has strongly increased at lowest elevations ($1500-1750$ *m asl*), which coincides with agricultural land use areas. For shallow landslides a shift in susceptibility zone can be observed. While higher elevations ($1750-2250$ *m asl*) show an increase, there is a small decrease at lowest elevations. This is discussed in further detail in Section 2.4.2.

Shallow Landslides

The spatio-temporal analysis of shallow landslides is discussed in more detail, as the sites have unambiguous, clear boundaries and we were able to compare our data with a previous study of manually mapped landslides by Meusburger and Alewell (2008). The temporal analysis reveals high dynamics within the catchment (Figure 2.10).

Changing areas are either highlighted as degrading (red; increasing trend) or as recovering (blue; decreasing trend). While recovery can be observed in some areas (i.e., north-east section and north-west facing slope), most grid cells show a strong increase, mainly located on the south-east facing slope. Most shallow landslides are located at mid-range elevations ($1750-2000$ *m asl*) and have increased only slightly since the year 2000 (Figure 2.9). While areas near the valley bottom ($1500-1750$ *m asl*) show a minor decline, the amount of area affected by shallow landslides above 2000 *m asl* has increased by around 40 % (1.8 – 3.1 *ha*). Affected areas near the valley floor are located in a geologically susceptible formation (Mesozoic layer) as well as regions heavily used for cattle and sheep pasturing (for more information on land use and geology see Meusburger and Alewell (2014)). The increase at higher elevations cannot be explained by intensified land use practices, as there is hardly any change in the intensity of livestock grazing. Therefore, the increase might be caused by snow processes and precipitation. Field observations at these higher sites indicate snow-gliding processes during the winter, such as abrasion marks on the bare soil and rolled up vegetation in the vicinity of shallow landslides shaped by the pressure of the moving snow cover (Meusburger and Alewell, 2014).

In addition to catchment scale overviews, the results allow for close-up evaluations of sites for better understanding of the local dynamic impacts on degraded sites (Figure 2.11). In the depicted region, a triggering event between the years 2010 and 2013 caused a sudden increase of bare soil sites. The

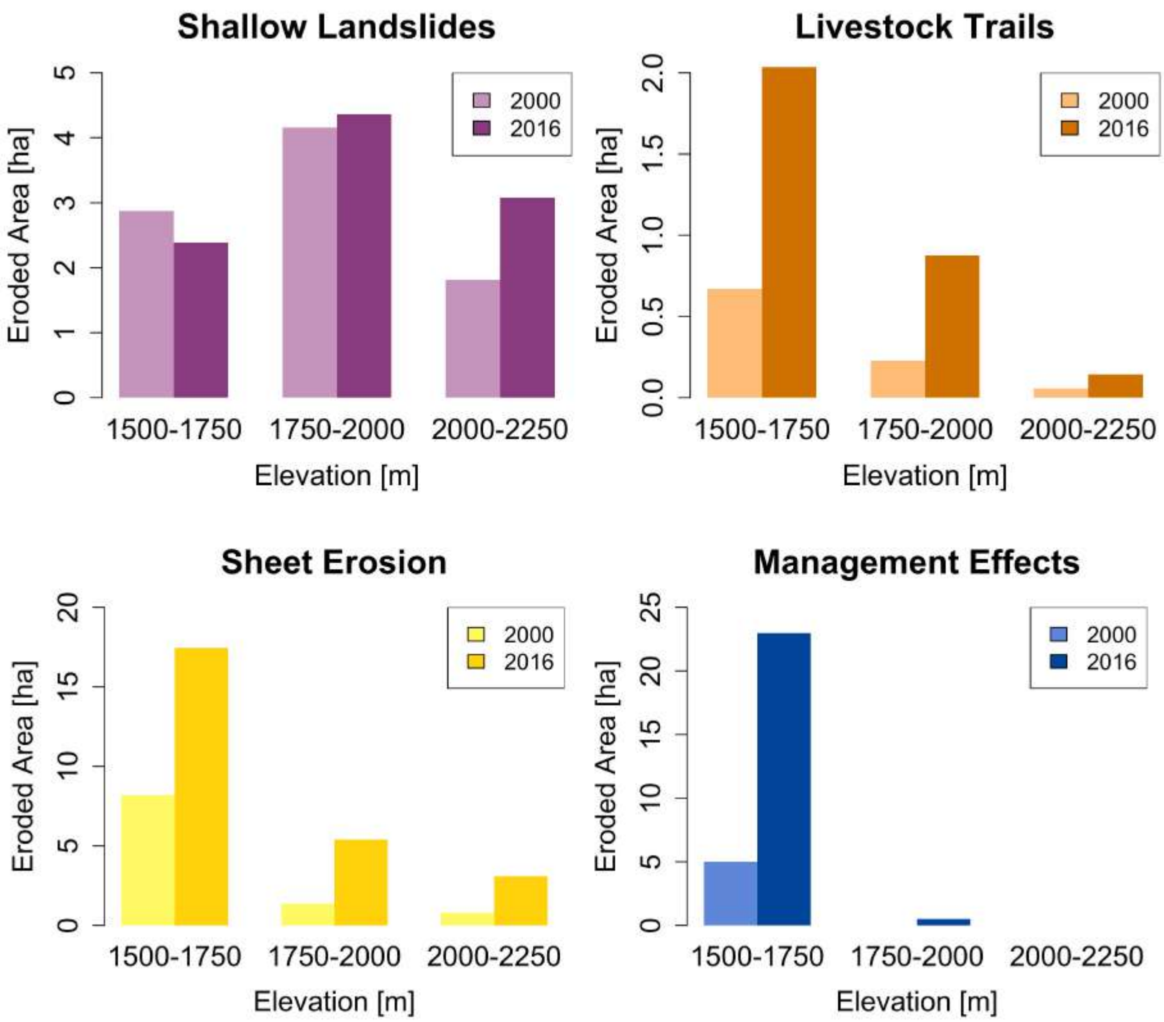

Figure 2.9: *Susceptibility zones with changes observed from 2000 to 2016 for shallow landslides (purple), livestock trails (orange), sheet erosion (yellow) and management effects (blue). Scales of the x-axis vary between erosion classes.*

disappearance of shrubs might have been caused by a high intensity event, such as an avalanche, or an increase in sheep stocking, as sheep for debarking shrubs (e.g., *Alnus viridis*, *Sorbus aucuparia*) were introduced to the valley for landscaping purposes.

As the two orthophotos of 2000 and 2004 were also used in the study by Meusburger and Alewell (2008), we compare results of manually mapped sites with results of OBIA (Figure 2.12). Because OBIA is capable of mapping smaller landslides ($> 4\ m^2$) than the manual method allows ($> 10\ m^2$), the total area is slightly higher for both years we compare (1.1 *ha* more on average). Still, the increasing trends are comparable between the two methods. The area affected by shallow landslides has doubled since 1959 from approx. 5 to 10 *ha*, demonstrating that long term monitoring is a necessity, as recovering phases are succeeded by newly triggering events.

2.4.3 Possible Causes for Increasing Trends in Soil Degradation

Our results show an increase for all erosion types during the study period. Meusburger and Alewell (2008) showed that shallow landslides specifically have increased over a longer time period using

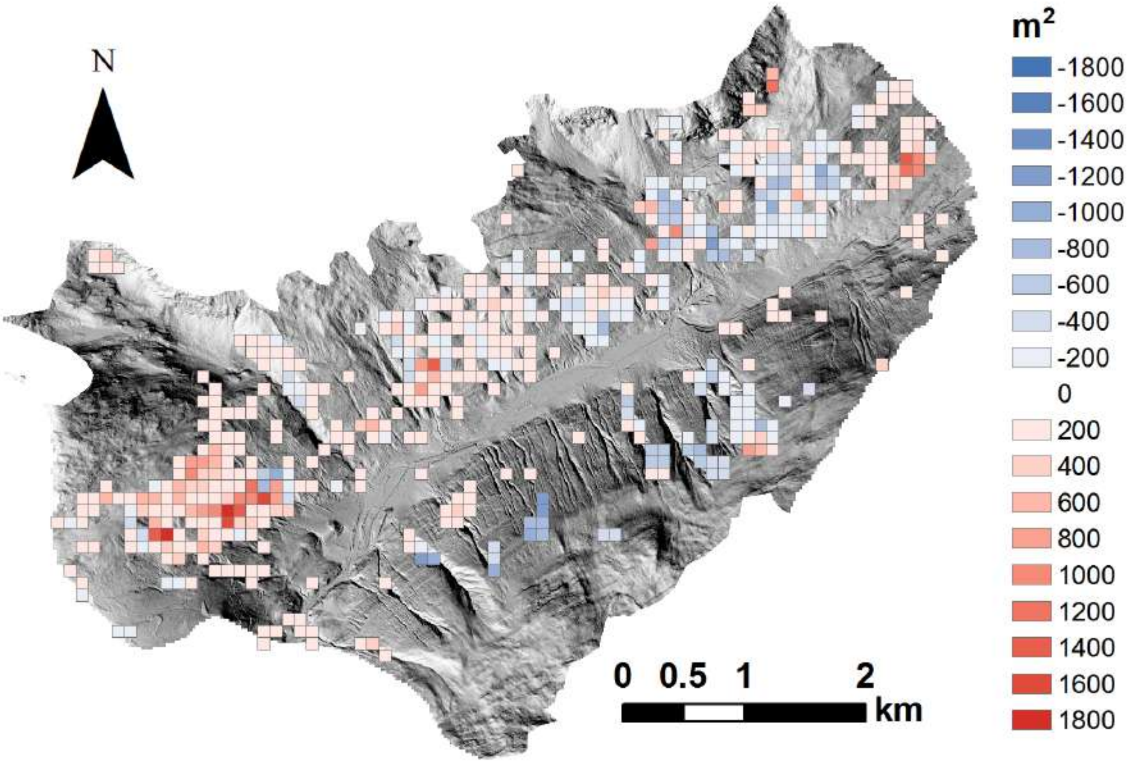

Figure 2.10: *The Urseren Valley with its temporal and spatial changes of shallow landslide affected areas between 2000 and 2016. Grid-cells have a size of* 100*x*100 *m. Areas in blue show amount of decrease and areas in red show amount of increase.*

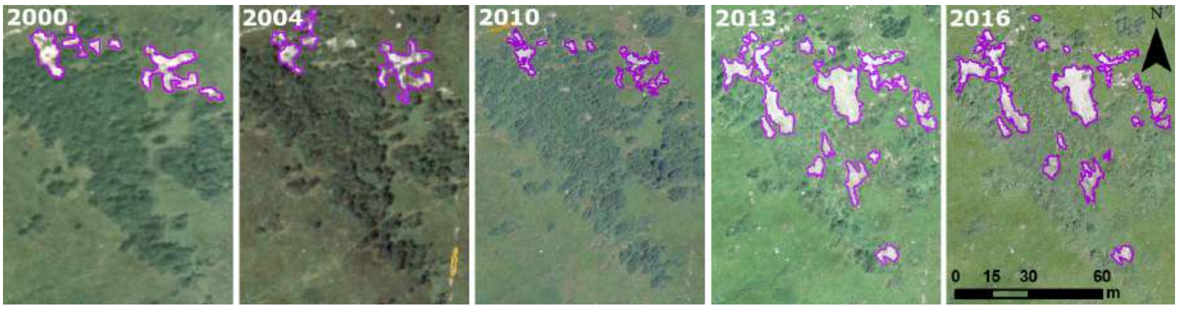

Figure 2.11: *A selected subset of the Urseren Valley as an example for the dynamic aspect of erosion on grasslands. The time series shows the evolution of shallow landslides from 2000 to 2016 parallel to a decrease in shrub cover. The smallest detected objects have a size of 4.5* m^2

images dating back to 1959. Some factors influencing soil degradation and soil erosion can be considered constant over time, such as the geological bedrock or the topographical conditions. However, other factors influencing erosion processes undergo dynamic changes, such as climate conditions and land use management. We found that areas of the Urseren Valley at lower elevations are showing increasing amount of erosion including erosion patterns linked to anthropogenic activity, such as land use management. Regions at higher elevations are barely used for agricultural purposes and therefore the observed increase has to be linked to climate related factors or grassland abandonment (Tasser et al., 2003; Meusburger and Alewell, 2008). Heavy machinery was introduced in the 1970's which simultaneously replaced traditional farming (e.g., manually repairing spots of damaged soil surface, cutting back single shrubs etc.) (Meusburger and Alewell, 2008; Scheurer et al., 2009). We have been able to document this increase in observable management degradation on the lower slopes using

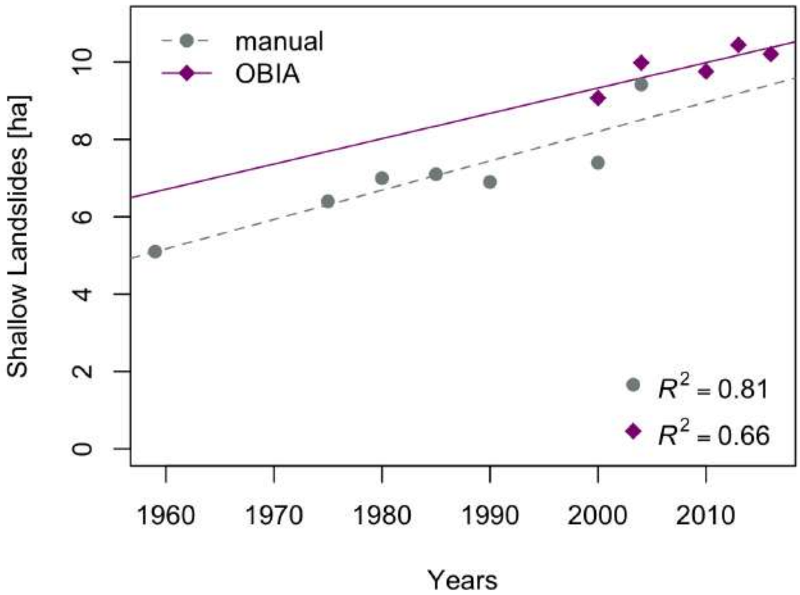

Figure 2.12: *Urseren Valley showing the temporal development of shallow landslides between 1959–2016 of the total affected area. Grey points (1959–2004) were mapped manually by Meusburger and Alewell (2008) and purple points (2000–2016) were mapped using OBIA. Lines indicate the trend given by a linear regression.*

OBIA. These management changes also influenced the use of livestock pastures. While remote and difficult to access areas were abandoned due to the resignation of permanent herding practices, areas closer to the valley floor and therefore easier to access, are being used more intensely (Meusburger and Alewell, 2008). In addition to a decrease in the effective pasture areas (i.e., because higher alpine pastures were abandoned), the number of cattle and sheep was increased (Meusburger and Alewell, 2008). These changes coincide with the increased amount of livestock trails observed and mapped at lower elevations, and may still have a continuous affect in the future. Sheet erosion is caused by increased run-off and/or by a reduction of the vegetation cover (Meusburger and Alewell, 2014; Nearing et al., 2004). The vegetation cover can be damaged by grazing and trampling of livestock or biomass production can be affected by drought. The latter can cause hydrophobicity and sealing of the soil and thereby changes run-off properties (Konz et al., 2010; Nearing et al., 2004; Scheurer et al., 2009). Presently, there are more days in the summer without rain, and this is expected to continue in the future. However, extreme precipitation events will be more frequent, which has already been observed for many areas in Switzerland since 1901 (CH2018, 2018). Prolonged intense precipitation events are also a major cause of shallow landslides (Gariano and Guzzetti, 2016). An increasing temperature trend has been observed for winter months too, and is expected to increase in the future (CH2018, 2018). Rapid snow-melt with warmer spring temperatures, causes additional run-off threat to soils (Konz et al., 2012; Saez et al., 2013). The winter temperatures could also have an influence on the occurrence of snow-gliding, which is the most common cause of shallow landslides (Wiegand and Geitner, 2013). Fromm et al. (2018) found, that parameters such as higher soil temperatures and higher soil moisture contents cause increased snow-gliding. Snow movement can also produces fissures, that can lead to the formation of new landslides (Blechschmidt, 1990; Leitinger et al., 2008; Meusburger and Alewell, 2009; Wiegand and Geitner, 2010b; Newesely et al., 2000). The effects of climate change on erosion processes can be complex due to feedback mechanisms. However, with the effects of both longer dry phases and extreme precipitation events as well as altered snow dynamics we can expect more soil degradation to occur, which is consistent with our observed trends (Nearing et al., 2004; Pruski and Nearing, 2002; Saez et al., 2013; Wood et al., 2016).

2.4.4 Accuracy Assessment

For all erosion classes we conducted a thorough visual investigation with zooming in to the respective orthophotos to assure the accuracy of the results. The analysis showed, that for livestock trails, sheet erosion and management effects the degraded areas are underestimated. For this reason, values of areas affected by these three erosion classes are to be considered as conservative estimations, with real numbers being considerably higher. Visual assessments of the orthophotos confirmed our general increasing trends of soil degradation. Additional accuracy assessment was conducted on the basis of randomly selected points, which were evaluated by experts familiar with the field situation in the valley (see Section 2.3.3). The evaluated points were compared to the results of OBIA to calculate accuracy scores for each mapped orthophoto (Table 2.5). The Overall Accuracy is in a range of 0.78 to 0.88 for all orthophotos with Kappa coefficients ranging from 0.65 to 0.81. Lower scores were achieved for the year 2004, which also has the darkest color conditions and was therefore harder to work with. With similar scores for the year 2000 compared to newer images (2010, 2013, 2016), we can assume, that the lower spatial resolution does not have major impacts on the accuracy of the results.

Table 2.5: *Accuracy scores of erosion categories using random sample evaluation.*

Orthophoto	Overall Acc.	Producer's Acc.	User's Acc.	Kappa
2000	0.87	0.77	0.79	0.81
2004	0.78	0.62	0.64	0.65
2010	0.88	0.86	0.85	0.81
2013	0.87	0.82	0.85	0.80
2016	0.87	0.89	0.81	0.81

With OBIA we generally obtain more accurate boundaries of erosion features and also detect smaller sites, which are mostly missed during manual mapping (Figure 2.13). Nevertheless, we also compared the shallow landslides of the manual data set to our OBIA results (only sites $> 10\ m^2$ to guarantee comparability) and calculated accuracy measures based on overlapping objects for the years 2000 and 2004. The OBIA mapped landslides have a Producer's Accuracy of 0.91 and a User's Accuracy of 0.86, which coincide with visual assessments, that landslides are the erosion features with the highest mapping accuracy. Additional measurements in the field showed, that the mean areal deviation between measurements and their corresponding sites mapped with OBIA is 6.5%.

2.4.5 Limitations of the Method

The investigation of the results showed, that the quality of mapped shallow landslides is very satisfying (Section 2.4.4). The other erosion classes have boundaries that are difficult to precisely delimit due to smooth transitions (sites with reduced vegetation cover susceptible to sheet erosion) or are simply too fine to always capture their entirety (livestock trails). The lower spatial resolution of 0.5 m of the orthophotos taken in 2000 and 2004 makes the precise erosion mapping more difficult, especially in the case of livestock trails. Even though features with clear boundaries $> 4\ m^2$ were detected, the overall area mapped as degradation is rater underestimated due to (i) underestimation of feature area or (ii)

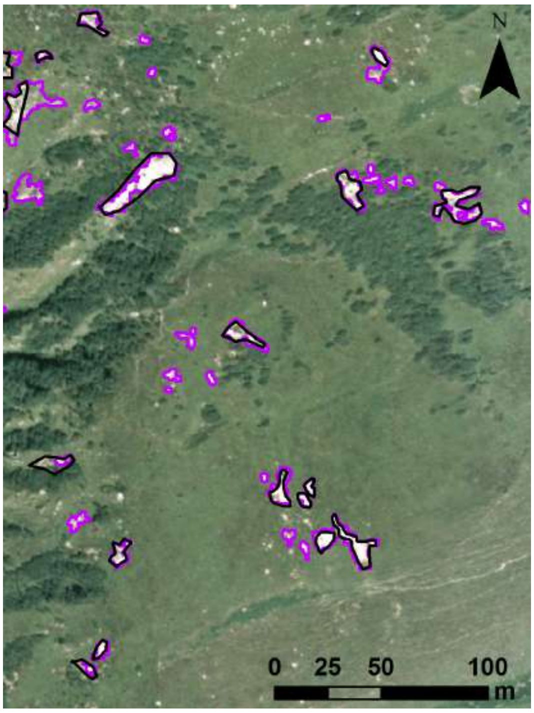

Figure 2.13: *A subarea of the Urseren Valley (2000) showing the results of the OBIA classification (purple) vs. the manual classification (black) of shallow landslides produced by Meusburger and Alewell (2008).*

non-detection of features with very diffuse boundaries. Other issues we encountered were the varying color spectra of the orthophotos mainly caused by the different acquisition times. This had a significant effect on the color of the vegetation, which required adaptations of the OBIA work-flow concerning ExG thresholds and some color related features such as brightness. Additional manual corrections were necessary to assure the correct mapping with OBIA and to guarantee the comparability between the individual years (Figure 2.5). For certain years up to 20% of soil erosion object classifications had to be changed manually after applying OBIA. Re-classifications mainly consisted of changing sheet erosion to shallow landslides and vice versa, to match mapping results of preceding orthophotos. Another source of error were individual rocks, which were not always successfully excluded from the soil erosion objects during the random forest classification. In some cases it was not possible to select perfect thresholds for the rule set, which assigned one of the four specific erosion categories to the soil erosion objects. In these cases the objects were wrongly classified as sheet erosion before manual corrections, as this is the remaining erosion class by default. The work time to map one orthophoto was approximately 4-5 working days including manual corrections.

2.5 Conclusions & Outlook

For this study, we developed a holistic approach using OBIA to provide information on the location and extent of different erosion features on high-resolution orthophotos ($0.25 - 0.5\ m$) for the Urseren Valley (Central Swiss Alps). We were able to use OBIA to map and classify sites according to the main erosion process or triggering land use management impact. For this purpose, we differentiate between erosion sites with clear boundaries (shallow landslides $> 4\ m^2$, livestock trails or management effects) and degraded sites with more diffuse boundaries (sites with reduced vegetation cover susceptible to sheet erosion). The differentiation between soil erosion class as well as the possibility to map small erosion features is crucial for the understanding of ongoing soil degradation within the catchment as well as for decision making at the level of local authorities to determine suitable land use and mitigation possibilities.

Our results show that soil degradation has increased during the study period for all erosion classes. The south-east facing slope, which has a higher fertility and therefore is used more intensely for pasturing, is affected by 90% of the ongoing soil degradation. We found that an increase of soil degradation at lower elevations is mainly due to land use practices, as increases were primarily classified as livestock trails, sheet erosion and management effects. Slopes at higher elevations, however, which are not or only to a limited extent used for grazing purposes are mostly affected by an increasing amount of shallow landslides and sheet erosion, that we associate with changing climate conditions (e.g., more frequent precipitation events, prolonged drought and changing snow dynamics).

Verification and corrections of the results are labor intensive and affected areas are often only conservative estimates due to the limiting factor of the spatial resolution of the images used. The results of the mapped erosion categories have Overall Accuracy scores of 0.78 – 0.88 (Kappa of 0.65 – 0.81). The date of acquisition of the orthophotos (e.g., color or state of the vegetation) and temporal variability of erosion processes are the main challenges for the mapping procedure. Especially fine erosion features, such as livestock trails, are often difficult to map in their entirety, due to the spatial resolution of the images. Small erosion sites are generally more difficult to detect repeatedly from one year to the next, due to the dynamic nature of these erosion sites, which also includes recovery of affected areas.

Spatial resolutions of orthophotos and digital terrain models are expected to increase in the future with SwissImage already being produced with a GSD of 10 cm for certain regions in Switzerland. These improvements in data quality will increase the capability of OBIA mapping. Not only will finer objects become easier to classify, but also the textural information used during the analysis is likely to improve. Furthermore, including more spectral bands, such as near infrared, would increase classification accuracy. Although this data is available (e.g., SwissImage RS containing RGB and NIR channels), no historical data set exists yet, which was an essential limitation for this study. OBIA has proven to be a powerful tool for mapping erosion on catchment scale and allowed us to achieve a comprehensive understanding of the ongoing soil degradation situation in the Urseren Valley. The method allows for a better understanding of the different causes leading to soil erosion as well as the resilience of the soils. The method is transferable to other regions of similar scale, with slight adaptations to the work-flow concerning local conditions, such as the aspect of slopes in the valley (e.g., for the direction of livestock trails or color conditions of the images). However, the labor intensity of OBIA likely hinders efficient up-scaling of research areas to regional, national or continental scale. As such, for large-scale studies alternative methods such as Deep Learning might be considered for the detection and classification of objects on remotely sensed images.

Acknowledgements

This study was funded by the Swiss National Science Foundation (Project No. 167333) as part of the National Research Program *NRP75 – Big Data*. We want to acknowledge Geodata4edu and MeteoSwiss for providing the data sets we used. Additionally, we are very thankful to the anonymous reviewers for their valuable suggestions and comments with which this paper was improved.

Soil Erosion on Alpine Slopes
Photo: Elia Kilcher

3

Identifying Soil Erosion Processes in Alpine Grasslands on Aerial Imagery with a U-Net Convolutional Neural Network

Abstract

Erosion in alpine grasslands is a major threat to ecosystem services of alpine soils. Natural causes for the occurrence of soil erosion are steep topography and prevailing climate conditions in combination with soil fragility. To increase our understanding of ongoing erosion processes and support sustainable land-use management, there is a need to acquire detailed information on spatial occurrence and temporal trends. Existing approaches to identify these trends are typically laborious, have lack of transferability to other regions, and are consequently only applicable to smaller regions. In order to overcome these limitations and create a sophisticated erosion monitoring tool capable of large-scale analysis, we developed a model based on U-Net, a fully convolutional neural network, to map different erosion processes on high-resolution aerial images (RGB, 0.25–0.5 m). U-Net was trained on a high-quality data set consisting of labeled erosion sites mapped with object-based image analysis (OBIA) for the Urseren Valley (Central Swiss Alps) for five aerial images (16 year period). We used the U-Net model to map the same study area and conduct quality assessments based on a held-out test region and a temporal transferability test on new images. Erosion classes are assigned according to their type (shallow landslide and sites with reduced vegetation affected by sheet erosion) or land-use impacts (livestock trails and larger management affected areas). We show that results obtained by OBIA and U-Net follow similar linear trends for the 16 year study period, exhibiting increases in total degraded area of 167% and 201%, respectively. Segmentations of eroded sites are generally in good agreement, but also display method-specific differences, which lead to an overall precision of 73%, a recall of 84%, and a F_1-score of 78%. Our results show that U-Net is transferable to spatially (within our study area) and temporally unseen data (data from new years) and is therefore a method suitable to efficiently and successfully capture the temporal trends and spatial heterogeneity of degradation in alpine grasslands. Additionally, U-Net is a powerful and robust tool to map erosion sites in a predictive manner utilising large amounts of new aerial imagery.

Study published as Samarin[†], M., Zweifel[†], L., Roth, V., Alewell, C., 2020. *Identifying Soil Erosion Processes in Alpine Grasslands on Aerial Imagery with a U-Net Convolutional Neural Network.* Remote Sens. 12, 4149. [†] authors contributed equally to this study

3.1 Introduction

Soil degradation is a major ecological threat which affects many areas of the world and can be accelerated by land-use management and changing climate parameters, such as precipitation and temperature (EEA, 2009; Fuhrer et al., 2006; Meusburger and Alewell, 2008; Nearing et al., 2004; Scheurer et al., 2009). In Switzerland, some alpine grassland areas are strongly affected by soil erosion due to the steep terrain and extreme climate conditions. While soil erosion occurs naturally in these environments—in the form of landslides (triggered by snow gliding or heavy precipitation events) or sheet erosion (the process of the removal of topsoil caused by rain drops' impacts and overland flow)—there are also anthropogenic influences (e.g., agricultural activities) which can accelerate erosion rates (Meusburger and Alewell, 2008; Tasser et al., 2003; Zweifel et al., 2019). For example, livestock keeping can lead to overgrazing and trampling in favoured grazing areas. Over time, livestock trails develop and trampling and grazing can lead to a reduction in vegetation cover, which in turn is prone to sheet erosion (Apollo et al., 2018; Torresani et al., 2019). Additionally, livestock keeping can cause instabilities on slopes and ultimately result in landslides (Wiegand and Geitner, 2010b). Therefore, erosion processes have strong temporal and spatial dynamic components, which is why large-scale understanding and detailed mapping over time and space is of great importance for long-term sustainable management practices. Alpine areas are difficult to access and erosion features can affect substantial areas, making a comprehensive understanding of ongoing erosion processes unattainable from the ground. Larger-scale erosion studies for Switzerland have mainly been approached with the help of soil erosion modelling—e.g., the (revised) universal soil loss equation (Alder et al., 2015; Bircher et al., 2019; Meusburger et al., 2010a, 2012; Prasuhn et al., 2013; Schmidt et al., 2018, 2019b,a). To achieve a thorough understanding of potential soil erosion threats, it is important to combine model outputs with observations for validation purposes (Fischer et al., 2018). The latter is especially crucial in mountainous and grassland areas, where model suitability has been questioned (see discussion in Alewell et al. (2019)). High-resolution aerial imagery offers the opportunity to remotely assess and map the spatial extent of bare soil sites and sites with strongly reduced vegetation cover, allowing certain constraints to be overcome, such as the inaccessibility or extent of a study area. Object-based image analysis (OBIA) is an approach commonly used to identify urban and natural "objects" on satellite and aerial imagery and has been successfully used in the past to map various forms of soil erosion (D'Oleire-Oltmanns et al., 2012; Eisank et al., 2014; Guzzetti et al., 2012; Hölbling et al., 2015, 2016a, 2020; Martha et al., 2012; Shruthi et al., 2011; Wang et al., 2020; Wiegand et al., 2013; Zweifel et al., 2019). OBIA creates image segments by grouping pixels with similar properties together, which can then be classified based on object information (spectral, spatial, textural, and contextual) with expertly developed classification rules and/or various machine learning classifiers. OBIA is a method suitable for smaller study areas, but large-scale studies become difficult to manage. Limitations including processing times, a lack of work-flow transferability to other scenes, and the involvement of manual steps hinder efficient spatial up-scaling of projects. In past years, deep learning methods have progressively been applied in the field of remote sensing for image classification tasks and segmentation tasks (Ma et al., 2019; Heydari and Mountrakis, 2019; Huang et al., 2018; Yuan et al., 2020). In this study, we apply a deep learning method to demonstrate that it is capable of mapping and classifying soil erosion features on aerial images in a fast, objective, reliable, and scalable manner. We apply a fully-convolutional neural network (CNN) framework using the U-Net architecture developed by Ronneberger et al. (2015). In general, the U-Net architecture offers itself to semantic segmentation tasks with limited training data. U-Net and variations of this architecture have become increasingly popular for remote sensing tasks. Many applications focus on urban settings for road (Yuan et al., 2019; Zhang et al., 2018b; Alshaikhli et al., 2019; Wulamu et al., 2019) or building extraction (Xu et al., 2018; Yi et al., 2019; Ivanovsky et al., 2019; Mboga et al., 2019) from satellite and aerial imagery. Applications in a natural environment are constrained by the limited availability of high-quality labelled training data. Despite this limitation, U-Net has been applied in cloud detection on satellite images (Yang et al., 2019), mapping of woody vegetation (Flood et al., 2019), segmentation of plant species (Kattenborn et al., 2019), forest damage assessment (Hamdi et al., 2019), the extraction of Antarctic glacier and ice shelf fronts (Baumhoer et al., 2019), and archaeological studies (Bundzel et al., 2020) to name a few. Our annotated training data has been generated by mapping erosion sites on aerial images using OBIA for a valley in the Central Swiss Alps (Urseren Valley, Canton of Uri). We compare U-Net results to OBIA mapping for a held-out test region (area of 17 km^2), which was not used for training (9 km^2) for the years 2000, 2004, 2010, and 2013. Additionally, we investigate both the temporal and the spatial transferability of the U-Net method by mapping a new aerial image not seen during training (2016). Our main objectives of this study are: firstly, to show that the fully automated U-Net approach is capable of reproducing the high-quality soil erosion mapping and the temporal trends as they were attained with OBIA for the same study site; secondly, to show that the U-Net approach generalises well to new aerial images, i.e., can be used in a predictive manner to perform adequate segmentation of previously unseen input data. In contrast, the OBIA procedure typically eludes such predictive usage and needs to be adjusted for each new aerial image. The capabilities and the fully automated nature of the U-Net approach make it a highly promising tool for efficient large-scale erosion mapping (e.g., alpine-wide analysis of soil erosion in semi-natural ecosystems such as grasslands and bush-land).

3.2 Study Area

The Urseren Valley (26 km^2) is an alpine valley located in Central Switzerland in the southern part of the Canton of Uri (Figure 3.1). The valley has a NE–SW orientation, and exhibits steep slopes (average angle of 27°) and rough terrain. The valley is geologically divided into two distinct sections and separated by the river Reuss: The northern slope is part of the Aarmassif (granite), and the southern slope belongs to the Gotthard massif (gneiss). Located between these two massifs near the valley floor is the so-called Urseren—Garvera zone (Mesozoic sediments) (Wyss, 1986). The dominant soil types in the catchment are Podzols and Cambisols, with Leptosols commonly found on steep slopes (classified after IUSS Working Group WRB (2006)).

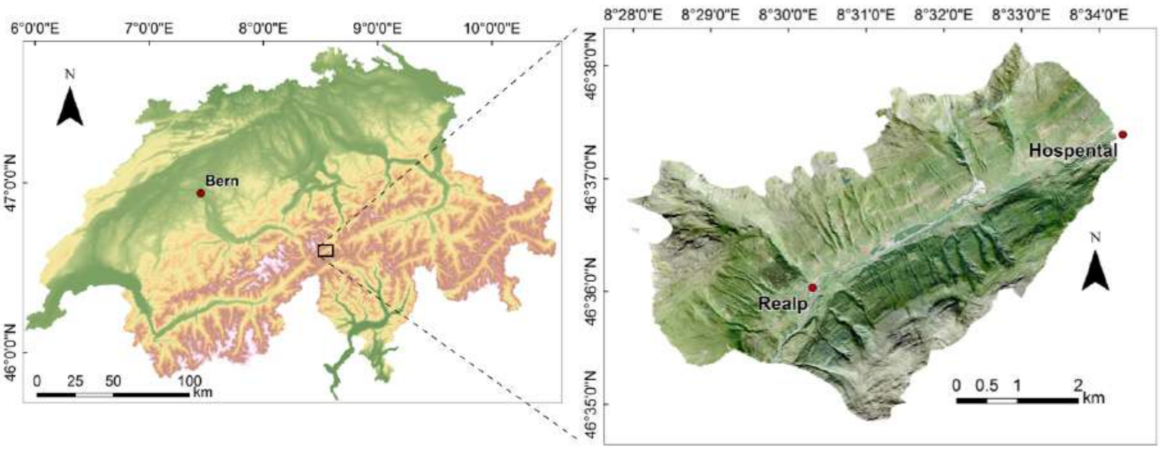

Figure 3.1: *The Urseren Valley is located in the Central Swiss Alps in the Canton of Uri. The left map contains the topographic map of Switzerland (from low elevations in green to high elevations in brown to white). The right image contains an aerial image of the Urseren Valley overlaid on a hill-shade map of the area.*

The 30 year average temperature (1990–2019) of the closest meteorological station in Andermatt (1438 m a.s.l.) is 3.9 °C. The average temperature has increased by 0.7 °C during the last 10 years (compared to the average of 1980-2009). The average rainfall during the last 30 years was 1384 mm with an average maximum 3 day precipitation intensity of 123 mm/3 d. The average seasonal (November–April) snow height is 58 cm with maximum snow heights during February/March (average of 103 cm) (data provided by MeteoSwiss, 2020). The dominant land-covers are grassland (including dwarf-shrubs consisting of Calluna vulgaris, Rhododendron ferrugineum, and Juniperus sibirica), which is mainly used for grazing (i.e., sheep and cattle) and haying and shrubs (mainly Alnus viridis and Sorbus aucuparia), and debris/bare rock areas (Meusburger and Alewell, 2008). Shrub encroachment due to land abandonment and extensification is present in the valley. Avalanches and snow gliding occur frequently in the Urseren Valley, facilitated by the deforested state of the slopes. The dominant erosion processes in this region are (shallow) landslides, sheet erosion, and erosion caused by land-use management (livestock, machinery, and manuring). Additional information on the Urseren Valley and occurring erosion processes can be found in Alewell et al. (2015); Meusburger and Alewell (2008); Zweifel et al. (2019).

3.3 Data Sets

In the following we present the data sets used in our study. Table 3.1 summarises the data sets used for the mapping procedure conducted with U-Net which were also the basis for the training data set produced with OBIA (Zweifel et al., 2019).

Table 3.1: *Summary of raster data sets used in this study. All geodata sets © Swisstopo. ⋆: The aerial image of 2016 was only used for validation purposes of the U-Net model.*

Data Set	Derivative	Bands	Spatial Res.	Recording Date	
Aerial Image		RGB	0.5 m	24. August	2000
		RGB	0.5 m	09. September	2004
		RGB	0.25 m	20. July	2010
		RGB	0.25 m	01. August	2013
		RGB	0.25 m	20. July	2016 ⋆
Digital Terrain	Slope		2 m		
Model (DTM)	Aspect		2 m		
	Curvature		2 m		

3.3.1 Aerial Imagery

The aerial images of SwissImage are high-resolution georeferenced orthophotos (product of Swisstopo (2010)). Five aerial images covering the Urseren Valley were used in the time from 2000 to 2016. These images have a spatial resolution of 0.5 or 0.25 m (Table 3.1). Spectral information is available in the visible range (red, green, and blue spectral bands). All aerial images have slightly different properties (e.g., spatial resolution, colour distribution, and lighting conditions) but were always recorded during the growing season between late July and early September.

3.3.2 Digital Terrain Model

The digital terrain model (DTM) SwissALTI3D is the surface model of Switzerland without vegetation and development and has a spatial resolution of 2 m (product of Swisstopo (2014)). Based on the elevation information of the DTM we derived the slope, aspect, and curvature (plan and profile) using ArcGIS (Version 10.5). The DTM provides valuable information and offers context to the aerial images. Zweifel et al. (2019) have shown that for their study using OBIA, the DTM and its derivatives were essential for successful erosion mapping and classification.

3.3.3 Training Data

The data used to train the U-Net model consists of aerial imagery, DTM information, and training labels (see Section 3.4.3 for the training process). To train our U-Net model, a subsection (9 km^2) of the Urseren Valley (26 km^2) was used with the corresponding OBIA-mapped features (Figure 3.2). Four of the aerial images were used during training, leaving out the year 2016. By separating a subsection for training, we tested the spatial transferability of the model within the larger valley region. In addition, by omitting 2016, we investigated the spatial and temporal transferability when applying U-Net to a different image with properties not known during training.

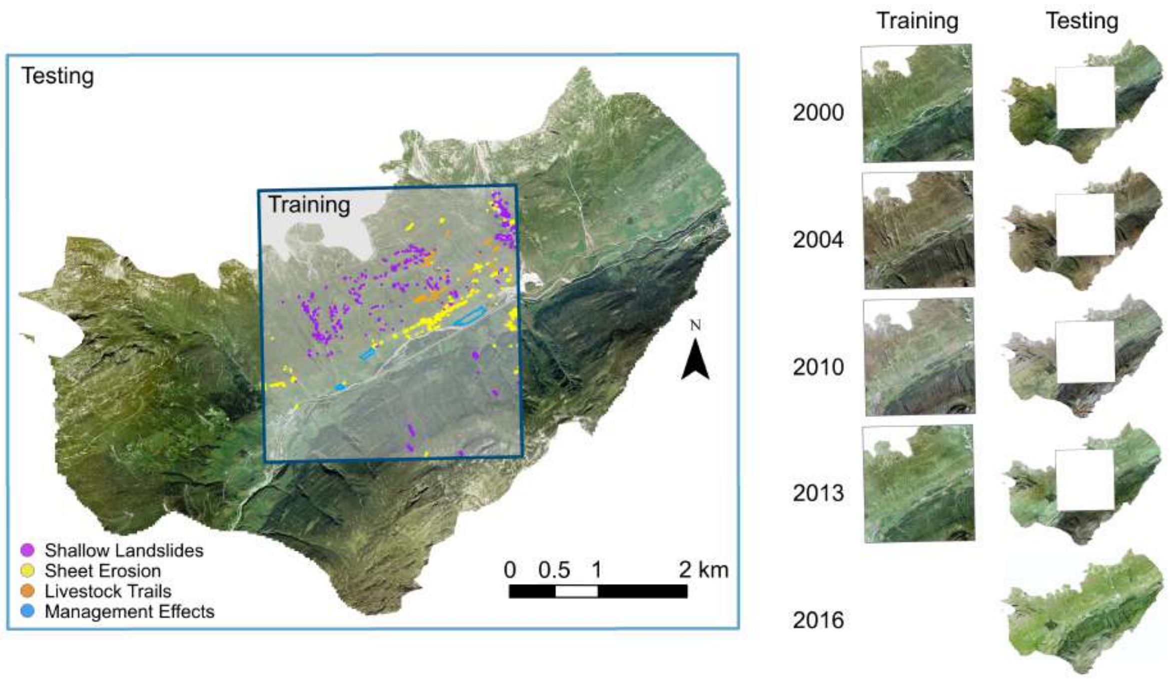

Figure 3.2: *Training (9 km^2) and testing (17 km^2) areas are marked on the aerial image with examples of OBIA training labels for 2000 (map on the left). On the right-hand side is an overview of all available years and the sections used for training and testing. All training areas contain OBIA training labels (not shown) for the respective years (2000–2013). Training labels vary for each year due to the continuous evolution of soil erosion sites. The entire area of the image taken in 2016 was used only for testing.*

Training Labels

The training labels come in the form of mapped erosion sites with attributed erosion classes from a previous study by Zweifel et al. (2019). This data set was created with a semi-automatic method using an OBIA approach described in Section 3.4.1, which made use of the same aerial imagery and DTM information as used for U-Net. Mapped erosion objects are available for the entire Urseren Valley for all five aerial images (2000, 2004, 2010, 2013, and 2016). Based on random sample evaluation by experts, this data set has an average overall accuracy score of 85.4% (Zweifel et al., 2019). The training labels consist of four different erosion classes: shallow landslides (areas with displaced topsoil layers and clear boundaries to the surrounding vegetation), livestock trails (elongated tracks caused by livestock trampling, mostly perpendicular to the slope), sheet erosion (patches with reduced vegetation cover), and management effects (large areas damaged by heavy machinery, over-fertilisation, or intense grazing in fenced-off areas) (see Figure 3.3).

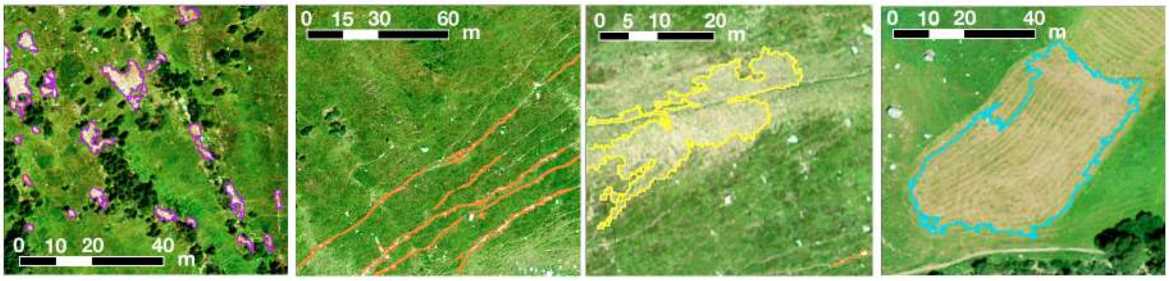

Figure 3.3: *Examples for the labels used for training the U-Net model. From left to right: shallow landslides, livestock trails, sheet erosion, management effects.*

3.4 Methods

Our methodology consists of two major parts: the training process and the prediction process, with an overview depicted in Figure 3.4. To train the U-Net model we use OBIA labels together with the respective aerial image information (RGB) and DTM information for a dedicated training area (9 km^2). U-Net assigns pixel-wise probability values and thus provides information about the likelihood of pixels belonging to a specific erosion class. Based on these probabilistic assignments, hard segmentations are produced by thresholding. The following sections will describe the methodology in further detail.

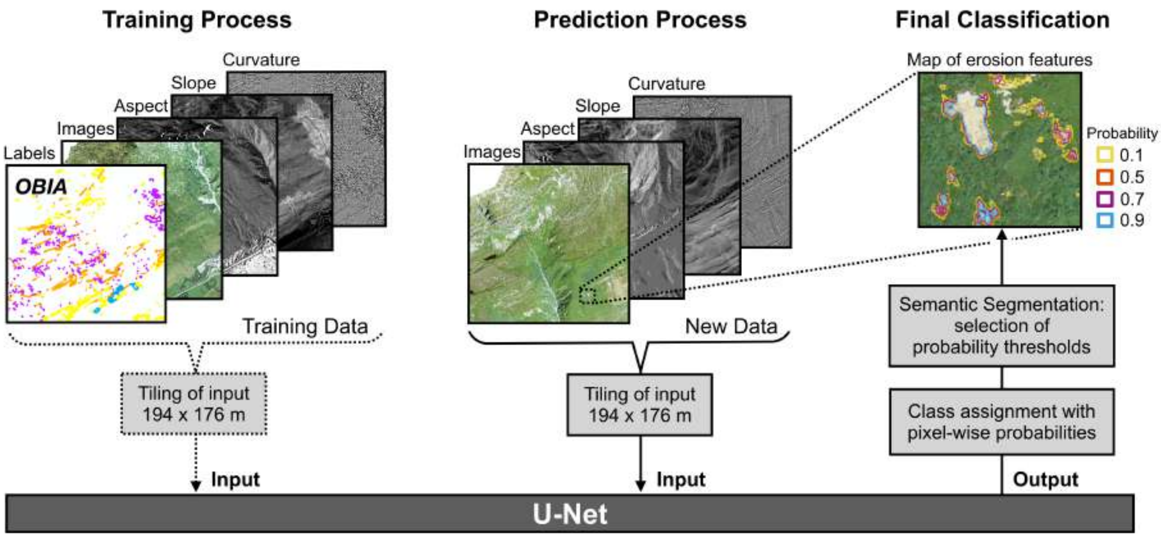

Figure 3.4: *An overview of the developed workflow on the basis of U-Net showing examples of input files for training and prediction purposes. The output shows one of four erosion classes, namely, shallow landslides, with four different probability thresholds.*

3.4.1 Object-Based Image Analysis

Object-based image analysis (OBIA) combines a segmentation algorithm with classification techniques ranging from decision trees to various supervised machine learning algorithms which assign generated segments (or object primitives) to erosion classes. We used the software eCognition Developer (version 9.3.2) implementing a multi-resolution segmentation algorithm for grouping pixels with similar properties to object primitives. Input data consisted of aerial imagery (RGB), the excess green vegetation index, and information from the DTM and its derivatives (slope, aspect, and curvature). The object primitives contained information on their spatial, spectral, textural, and contextual properties based on all input data. Given these extracted feature sets, a random forest classifier was trained on manually selected samples in order to identify bare soil sites or sites with reduced vegetation cover. Subsequently, an additional decision tree was assigned specific erosion classes based on the typical appearances of objects previously identified containing bare soil or reduced vegetation cover. These erosion classes consist of shallow landslides, livestock trails, sheet erosion, and management effects. Note that the entire workflow needed to be performed on every input image to accommodate for varying image properties. Therefore, OBIA-labels for different input images can be considered to be obtained from independent models (i.e., differently calibrated settings). A detailed description of the workflow is presented in Zweifel et al. (2019).

3.4.2 Neural Network Architecture

In this study, we make use of the U-Net architecture (Ronneberger et al., 2015) illustrated in Figure 3.5. U-Net is a fully convolutional neural network which consists of a contracting part and an expansive part. See Section S1 (Supplement) for more details on the main components of the neural network which are used in the following description.

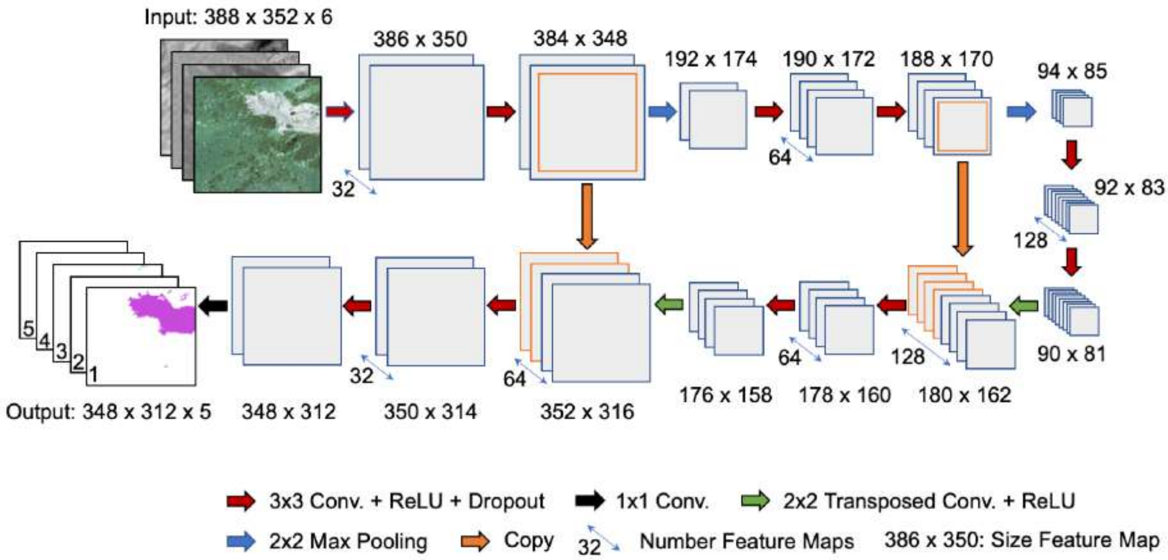

Figure 3.5: *The employed U-Net architecture: In the first (upper) part, the input is contracted into a compressed representation (right). In the second (lower) part, the compressed representation is expanded into a segmentation map with pixel-wise class probabilities. The input consists of the input RGB image (three channels) and the DTM derivative maps for the aspect, curvature, and slope (one channel each). The resulting output provides a segmentation map for each considered class: Shallow landslides (indicated by 1 in the output), livestock trail (2), sheet erosion (3), management effects (4), and a class for non-assignable pixels (5).*

In the contracting part (upper part in Figure 3.5), a sequence of two convolutional layers with ReLU activations followed by max pooling layer processes the input. With each max pooling application, the sizes of the resulting feature maps are halved, while the number of features is doubled for the subsequent convolutional layer. In the expansive part (bottom part), a sequence of transposed convolutional layers with ReLU activations followed by two convolutional layers and ReLU activations is applied to restore the original image size. Feature maps from the contracting part are appended to the feature maps obtained through the transposed convolutions to provide fine-detail features in the expansive part. Finally, a 1×1 convolutional layer followed by a pixel-wise softmax activation function provides the final segmentation output where each channel represents the segmentation map for the individual classes. The softmax function rescales the activations for each pixel to the $[0,1]$ interval. More explicitly, for a pixel f in the output map F, the softmax yields a prediction $p_c(f)$ which can be interpreted as the probability of pixel f to belong to class $c \in \{1,...,C\}$. The neural network is trained with the cross entropy loss which penalises incorrect class assignments with

$$-\frac{1}{N} \sum_{f \in F} \sum_{c \in C} y_c(f) \log(p_c(f)) \tag{3.1}$$

where $N = |F|$ is the number of pixels and $y_c(f)$ is the ground truth class assignment for pixel f, i.e., 1 if c is the correct class and 0 otherwise. For any pixel f in the input image, the softmax prediction $p(f) = \big(p_1(f), p_2(f), ..., p_C(f)\big)$ provides the probabilities for the classes $c \in$ {shallow landslide, sheet erosion, livestock trail, management effect, non-assignable}—e.g.,

$$p(f) = \big(\underbrace{0.55,\ 0.1,\ 0.2,\ 0.05,}_{\text{erosion class probabilities}}\ 0.1\big). \tag{3.2}$$

In addition to the four erosion classes, a class for non-assignable pixels is introduced which represents the class for all remaining (potentially ambiguous or vegetation covered and thus stable) objects. U-Net provides pixel-wise class probabilities like in Equation 3.2 as the probabilistic output. In the following, for each erosion class we will refer to the full-probability result when only entries for the specific class of this output are considered without applying a threshold (e.g., the first entries for shallow landslides). For the final hard segmentation, we would like to obtain the dominant erosion class and apply different probability thresholds that control to which extent candidate segments are obtained. We only consider the erosion classes and identify the class with the largest probability for pixel f as the dominant erosion class. If the selected erosion class probability does not meet the threshold, the respective pixel is considered as a background pixel. For example, in Equation 3.2, argmax$\{0.55,\ 0.1,\ 0.2,\ 0.05\}$ implies that shallow landslide is the dominant class and pixel f is predicted to be a shallow landslide pixel with a probability of 55%. At a threshold of 0.5, the class probability exceeds the threshold and pixel f is assigned to the shallow landslide class, while with a stricter threshold of 0.6 the pixel is considered to be a background pixel. With this kind of threshold segmentation, the final erosion class labels are obtained.

3.4.3 Training Process

In order to learn how to identify erosion sites, precise boundaries for the different erosion classes are required for training U-Net. Inadequate training labels can deteriorate the spatio-temporal generalisation capability of U-Net. In this study, we used high-quality training labels provided by the OBIA approach (see Section 3.3.3), and we considered the resulting erosion class areas as the ground truth segmentation in this investigation. To process the input images efficiently, we divided the aerial images into tiles of size 194 $\times$ 176 m which correspond to 388 $\times$ 352 pixels at 0.5 m resolution (2000, 2004) and 776 $\times$ 704 pixels at 0.25 m resolution (2010, 2013, 2016). The same is done for the maps of the DTM derivatives aspect, curvature, and slope.

Adjacent tiles overlap such that a 20 m (40 and 80 pixels, respectively) margin of one tile is contained in an adjacent tile. Figure 3.6 illustrates the resulting tiles for different years. The higher resolution tiles were down-sampled so that all input tiles are of size 388 × 352 pixels. No data augmentation was employed, as we expect object size and orientation (e.g., north/south exposure) to be relevant features. As described previously, U-Net was trained from scratch with tiles extracted from the training area of the years 2000 to 2013, with a total of 1292 training samples. A U-Net of depth 3 with initially 32 (root) filters was used (see Figure 3.5), resulting in 467,525 network parameters. The network was trained for 300 epochs with a batch size of 20, using the Adam optimizer (Kingma and Ba, 2015) with a learning rate of 0.001 and a dropout rate of 0.1. We used TensorFlow version 1.10 Abadi et al. (2016) for our implementation which is based on the U-Net implementation by Akeret et al. (2017). The full source code of our analysis pipeline is available under the GNU public license (`https://github.com/bmda-unibas/ErosionSegmentation`).

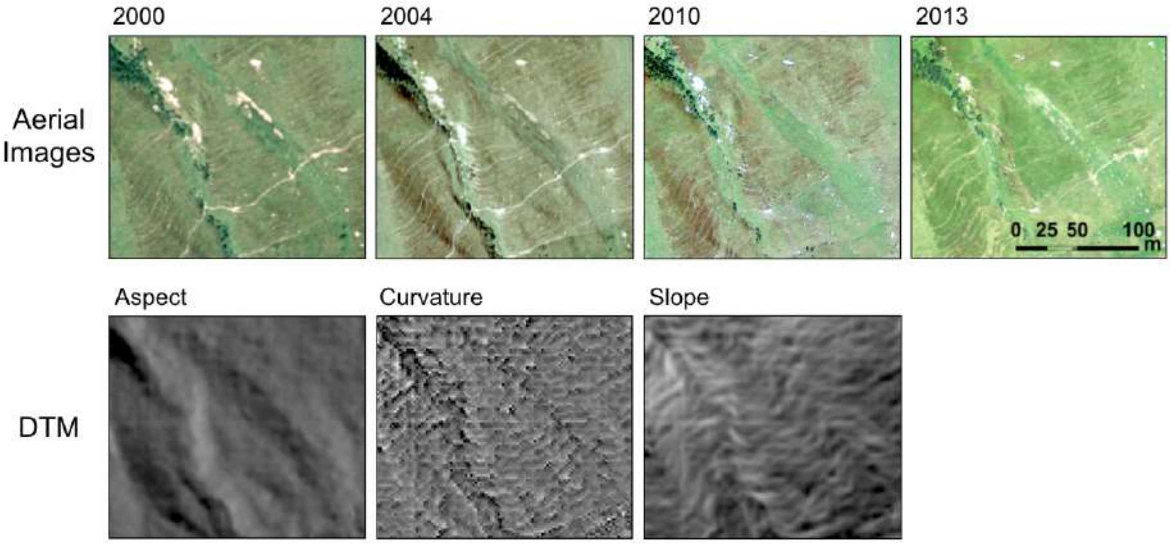

Figure 3.6: *Example of input RGB images for training for the years 2000, 2004, 2010, and 2013 with a size of 194 × 176 m (corresponding to 388 × 352 pixels at 0.5 m resolution). The images show examples of eroded area on grassland slopes (livestock trails, shallow landslides). Below, the corresponding aspect, curvature, and slope maps are displayed (for all years the same DTM information is used). To obtain the samples, the aerial images of the respective years (Figure 3.2) and the DTM derivatives were divided into smaller tiles.*

3.4.4 Details on the Evaluation

For the evaluation, only sites with an area of at least 4 m^2 were considered, which we treated as the minimum reasonable object size, and this is in line with the definition used in Zweifel et al. (2019). After choosing an appropriate probability threshold, the quality of the segmentation results was assessed with the precision score (producer's accuracy), recall score (user's accuracy), and their harmonic mean, the F_1 score. We considered objects which overlap in both the OBIA and U-Net results as true positives and weigh true positives, false positives, and false negatives by the areas of the respective segments. Ultimately, our goal was to evaluate the total degraded area on the held-out test area of the training years (2000, 2004, 2010, and 2013) and the validation year 2016 in comparison to the OBIA ground truth results. The emphasis here was to study the temporal trend and relative increase in degraded area as obtained from the different methods. We performed a linear regression to provide the linear trend over the time period from 2000 to 2016.

3.5 Results & Discussion

U-Net provides pixel-wise probabilities for each erosion class, which allows for assessing the certainty of predictions by studying the resulting heatmaps (see Figure 3.7 for an example). In practice, this rich information is further post-processed by applying a threshold on the pixel-wise probabilities to form well-delineated segments. In the following, we present both results on the (full-probability) heatmaps and results obtained with a selection of different probability thresholds. The latter enables a more direct comparison to the segmentation results obtained with OBIA. All results were obtained on the held-out test area (see Figure 3.2). Note that the data from 2016 was not used for training.

3.5.1 Segmentation of Soil Erosion Sites

The trained U-Net provides satisfying segmentation results which are demonstrated in Figure 3.7 for exemplary segments of shallow landslides and livestock trails. The heatmaps illustrate the full-probability output of U-Net and display the certainty in the class assignment (upper panel). By selecting different thresholds, hard class assignments can be achieved which lead to slightly different segment shapes depending on the threshold (lower panel). We selected thresholds of 0.2 and 0.8 to display the impacts of a wide range of probability thresholds on the delineation of segments. In general, choosing lower thresholds allows for the identification of a large number of potential erosion sites, while a higher threshold reduces the number of segments and also has an effect on the margins of these object, i.e., shrinks the segments to the most certain area. The probability threshold is a free parameter which can be chosen guided by application requirements or user preferences, or in our case to match baseline results (OBIA).

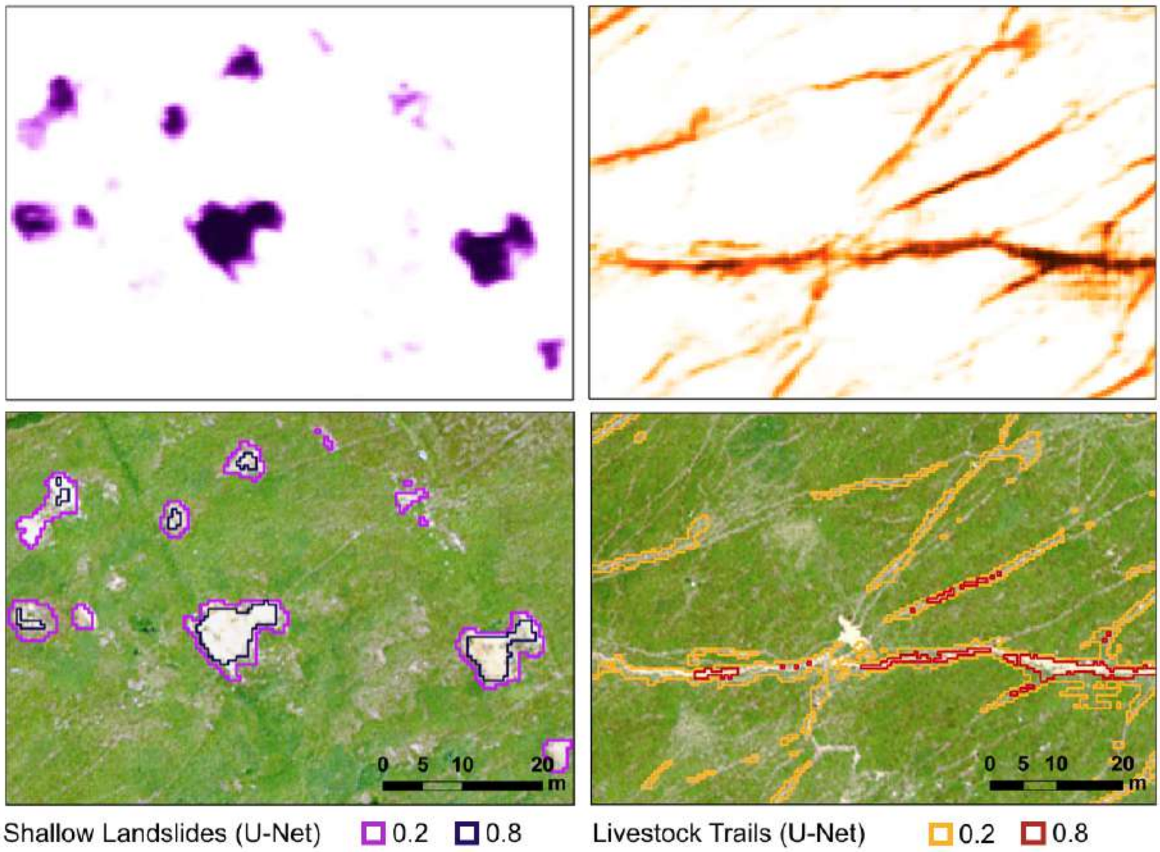

Figure 3.7: *Visualisation of U-Net mapped shallow landslides (left) and livestock trails (right) for 2016. The lower panel shows segmentation results with different probability thresholds: the lighter colour indicates a lower probability threshold (0.2) and the darker colour indicates a higher probability threshold (0.8). Lower thresholds lead to larger and more numerous segments. For the same region (background omitted for better visualisation), the upper panel shows the full-probability heatmap output of U-Net: darker colours indicate higher probabilities.*

In order to evaluate the accuracy of the proposed U-Net approach, we consider the OBIA results for 2016 as the ground truth baseline, which are independent of all other years, as OBIA was separately applied to the aerial image of 2016. For the comparison, we selected a threshold value of 0.3, as this led to the best agreement between U-Net and OBIA segments with respect to the total degraded area (see Section 3.5.2). OBIA relies on a dedicated, multi-resolution segmentation algorithm which provides clear objects to start with, which can then be classified. In contrast to OBIA, the U-Net approach does not have such a procedure and thus provides less control over segment shapes, as these are determined by pixel-wise thresholding. Consequently, there are cases in which both OBIA and U-Net identify areas as erosion sites but the boundaries of these objects might differ slightly. In that respect, our results for U-Net show that erosion sites with clear, unambiguous boundaries such as shallow landslides (and some very clear cases of livestock trails) generally have better overlaps with the OBIA baseline and contiguous objects are better identified (see Figure 3.8 on the left). Boundaries of more diffuse erosion sites predicted by U-Net show a slight mismatch with the OBIA baseline (see Figure 3.8 on the right). In these cases, the correct delineation of sites belonging to management effects or sheet erosion is in general a challenging task which is mirrored in the less accurate matching of the segmentation results from the different methods. Additionally, these erosion classes have similar appearances and are comprised of either bare soil or vegetation areas with strongly reduced vegetation cover which are prone to similar erosion processes (mainly erosion by water run-off), and they differ only in the origin of the damage. Management affected sites are mostly located near the foot of the slope, are mainly used for the production of hay, and can show signs of heavy machinery usage. Sheet erosion, on the other hand, can be found throughout the entire valley and can be caused not only by livestock trampling and grazing, but also climate-related factors, such as drought, precipitation, and snow-melt (Alewell et al., 2008; Meusburger and Alewell, 2014; Konz et al., 2010, 2012; Zweifel et al., 2019). Still, both methods are able to identify a great majority of overlapping objects. More quantitatively, we obtained scores for a threshold value of 0.3, as presented in Table 3.2.

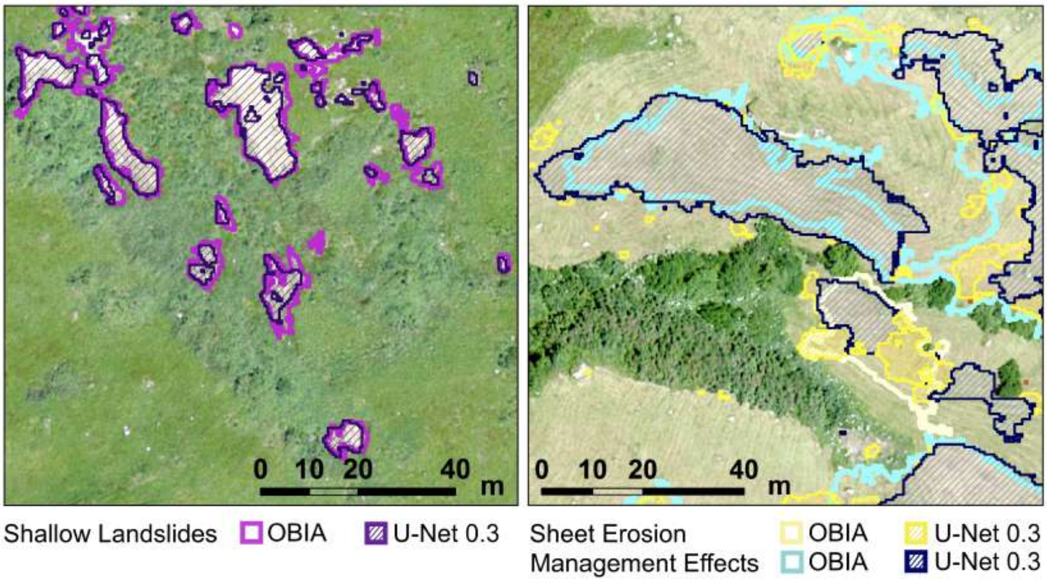

Figure 3.8: *Comparison of segmentation results of OBIA and U-Net (probability threshold of 0.3) for the aerial image of the year 2016. This aerial image was not used during training of the U-Net model and depicted sections are located in the held-out test area. Lighter colours show OBIA results; darker colours (shaded) are results of U-Net.*

Table 3.2: *Scores for U-Net with a threshold value of 0.3 for the validation aerial image of 2016. U-Net results are compared to OBIA baseline results.*

Scores	U-Net
Recall	84%
Precision	73%
F_1	78%

The precision score indicates that 73% of the predicted U-Net segments have corresponding OBIA segments, and about 27% of predicted U-Net segments do not directly correspond to any OBIA segments. On the other hand, the recall displays that 84% of the OBIA segments are maintained and the remaining 16% of OBIA segments are not identified by U-Net. Both these findings suggest that U-Net successfully identifies a majority of OBIA segments (recall score), but provides more segmented erosion sites than OBIA (false positives). Segments contributing to the 27% false positives still can be valid erosion sites which are not captured by OBIA, as it is known that OBIA tends to give a conservative estimate of the degraded soil (Zweifel et al., 2019). Therefore, it is important to note that these scores mainly highlight the difference between U-Net segmentation with respect to the OBIA segmentation baseline, and it is possible that one method captures valid erosion sites which the other method misses (see example shown in Figure 3.9 on the right).

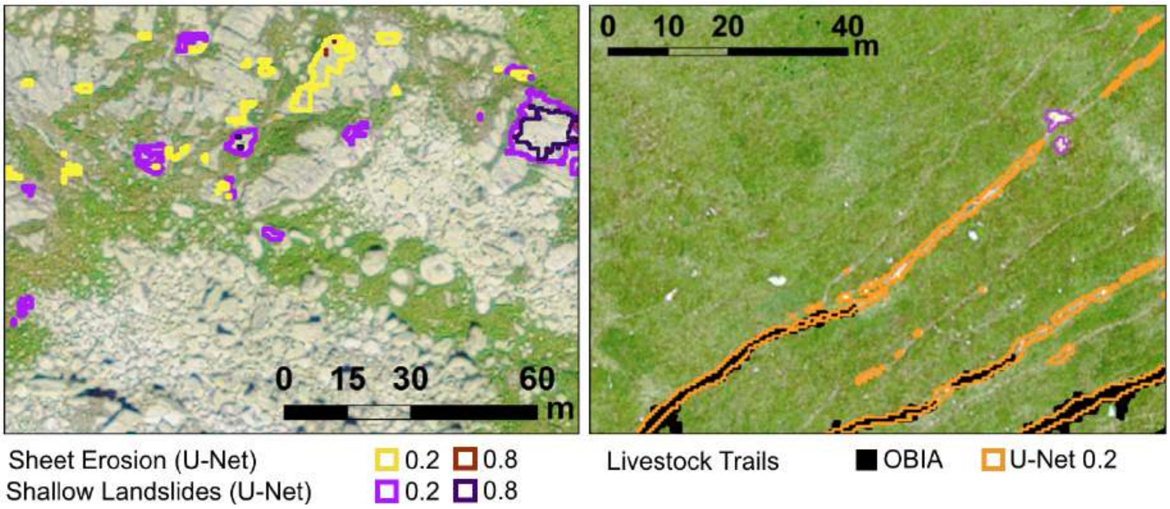

Figure 3.9: *Examples of two different types of false positives: On the left-hand side, U-Net identifies some rock surfaces as sheet erosion (yellow) and shallow landslides (purple). For both erosion classes, thresholds of 0.2 and 0.8 are shown. Lower threshold choices are linked to more of such false positives. Depicted on the right-hand side are livestock trails with OBIA and U-Net (threshold of 0.2). Here, U-Net is capable of identifying more livestock trails correctly compared to OBIA.*

Most cases of false positive predictions can be related to objects which are similar in appearance to the erosion classes, and the reason for misclassification can be recognised in many cases upon manual inspection. False positives are typically patches with rocks located at higher elevations which are classified as shallow landslides (see Figure 3.9 on the left), or varied classification of sites affected by management and sheet erosion. Nonetheless, singular rocks on grassland areas are successfully left unclassified. These kinds of disagreements are inherent to the U-Net approach, which attempts to identify regularities in the training data and thereby includes objects which share some similarities. In clear cases, such as very small object sizes or predictions at certain altitudes where a particular class of erosion phenomena is not expected, a post-processing step can address these erroneous classifications. Another way of avoiding segmentation ambiguities is to employ pre-processing steps to identify sub-regions of interest for target objects which share some kind of regularity in their appearance, for instance, in the shape of the objects (Guirado et al., 2017). For the purpose of this study, however, no pre-processing steps were used in U-Net training to ensure objective comparison with OBIA.

Threshold Selection

In similar studies, the matter of threshold selection is usually not addressed or a fixed threshold value is used. This can be suitable for studies with binary output classes (e.g., (Baumhoer et al., 2019; Zhang et al., 2018b)), but can also be problematic for gradual transitions of classified objects, as discussed by Kattenborn et al. (2019). Other studies employ deep learning approaches for classification of the object primitives in the OBIA framework where object boundaries are already well-defined (Fu et al., 2019; Zhang et al., 2018a; Lu et al., 2020). In our setting, threshold selection can be used to adjust segmentation results in relation to pre-existing knowledge (i.e., segmentation results of other methods such as OBIA), which led to the best fit with a threshold selection of 0.3 for this study (with respect to the total degraded area; see Section 3.5.2). Additionally, varying thresholds may be applied to make necessary adjustments for different classes with varying appearances. As a standard comparison, a held-out data set of the ground truth segmentation required for training can be used to determine appropriate probability thresholds if necessary. In the absence of appropriate pre-existing knowledge or in cases where visual assessment is not possible, it is advisable to use a range of probability thresholds which capture a variety of segment estimations and assess uncertainty ranges of the estimates.

3.5.2 Trend Analysis of Soil Erosion Sites

In order to study the temporal trend in the extent of soil degradation, we applied U-Net to the series of five aerial images of the Urseren Valley between 2000 and 2016 (see Section 3.3.3). We compare the full-probability U-Net results and the results for the different thresholds to the baseline results of the OBIA approach in Figure 3.10. In the first case, the heatmap results are added up to form an estimate of degraded area per erosion class. The resulting outcomes of the full-probability U-Net output match the OBIA results closely with respect to the total degraded area. Due to their methodological differences, slight deviations in the segmentation results and the resulting (total) degraded area were expected. The same holds true for the U-Net results with a threshold of 0.3. This threshold was identified to exhibit the most suitable agreement with OBIA segmentation results with respect to the total degraded area. It can be observed that for validation year 2016, the OBIA and U-Net threshold 0.3 results agree very well (in the shaded area in right plot of Figure 3.10). As expected, the U-Net results display an increase in degraded area for decreasing thresholds. Nevertheless, in all considered U-Net results, the same temporal trends of decrease and increase from one year to another are observed, as in the OBIA baseline. This observation is also supported by the linear regression results, which in all cases provide similar linear temporal trends.

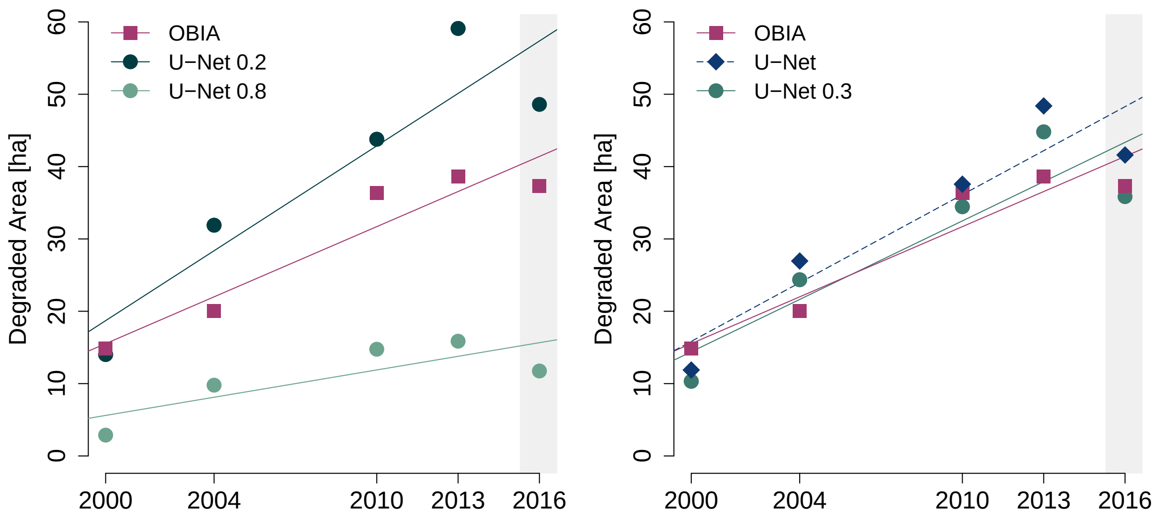

Figure 3.10: *Linear trend of the total degraded area in the held-out test region (see Figure 3.2) as obtained with the OBIA and U-Net approaches. On the left, the results for a range of different threshold values are displayed; on the right the results for the suitable threshold value 0.3 and the full-probability results are given. Qualitatively, a similar increase or decrease of degraded soil in the individual years is retained in all models. The linear interpolation provides a similar temporal trend of increase in degraded soil in all cases. In particular, the full-probability and threshold 0.3 results of the U-Net approach show good agreement with the OBIA baseline. The linear trends with lower and higher thresholds surround the OBIA result. The years 2000 to 2013 provide a result on the spatial generalisation of U-Net (years used for training), while the result for 2016 (shaded column) in addition provides a temporal generalisation result (aerial image of 2016 was not used for training). Note that the OBIA approach needs to be trained on all aerial images.*

In order to quantify the relative increase in degraded area, we consider the values for 2000 and 2016 obtained from the linear regression line. Again, the threshold dependency with respect to the total degraded area is observed (top panel in Figure 3.11). However, for the relative increase in degraded area (quotient of values for 2016 and 2000), the results become mostly independent of the selected threshold (bottom panel in Figure 3.11). To assess the statistical uncertainty of the linear regression fit and thus the relative increase, one standard deviation each of the fitted parameters (slope and intercept) is considered to obtain the two most extreme linear trends which are possible within the uncertainty of the fitted parameters. This means the steepest and flattest linear trends with respect to one standard deviation in the parameters are identified, which leads to the error bars for the total degraded area as depicted in Figure 3.11. As the relative increase considers the ratio of these quantities, the error bars are relatively larger for the relative increase of degraded area. In particular, for a threshold of 0.8, the statistical uncertainty increases due to the comparably small degraded area detected. The obtained U-Net results show similar relative increases of degraded area which fall within the uncertainty range of each other depicting the statistical uncertainty in the linear regression fit (one standard deviation). The U-Net results are in good agreement compared to the baseline method, with an increase of 167% in the test region. This in turn is in line with the increase of $156 \pm 18\%$ reported in Zweifel et al. (2019) for the full Urseren Valley, where $\pm 18\%$ depicts the estimated propagated error based on expert accuracy assessment (and not the statistical uncertainty in the linear regression fit). Importantly, it has been established that OBIA tends to underestimate the extent of degraded soil (Zweifel et al., 2019). Therefore, the steeper relative increase obtained by the U-Net results is plausible and potentially reflects the increase of degraded area more accurately. Furthermore, the fact that the relative increases for the different probability thresholds coincide with each other within the statistical uncertainty of one standard deviation of the linear regression fit is further evidence for the applicability and robustness of the U-Net approach. Assessing the relative development of aggregated measures, such as the total area of degraded soil, is therefore less sensitive to the choice of threshold. The results on the linear trend (Figure 3.10) and the relative increase of total degraded area (Figure 3.11) highlight that the probabilistic output of U-Net aligns with the OBIA results very well, and to study these quantities by choosing a threshold, i.e., hard segmentation, is not required. In our investigation we assess predictions in the held-out test region (see Figure 3.2) for two validation cases: (i) testing the erosion site prediction of the test region for years for which conditions (colour, shading, vegetation, etc.) were available during training (2000–2013) and (ii) testing the predictions for a new year for which conditions were unknown during training (2016). In the first case, our results provide evidence that the trained U-Net transfers well to adjacent regions with similar conditions, as observed during training, and that shows the spatial generalisation capability of the U-Net approach. Furthermore, the latter validation case gives evidence of suitable erosion site segmentation with the U-Net approach in completely new aerial images with conditions not encountered during training, which in addition highlights the temporal generalisation capability of the approach.

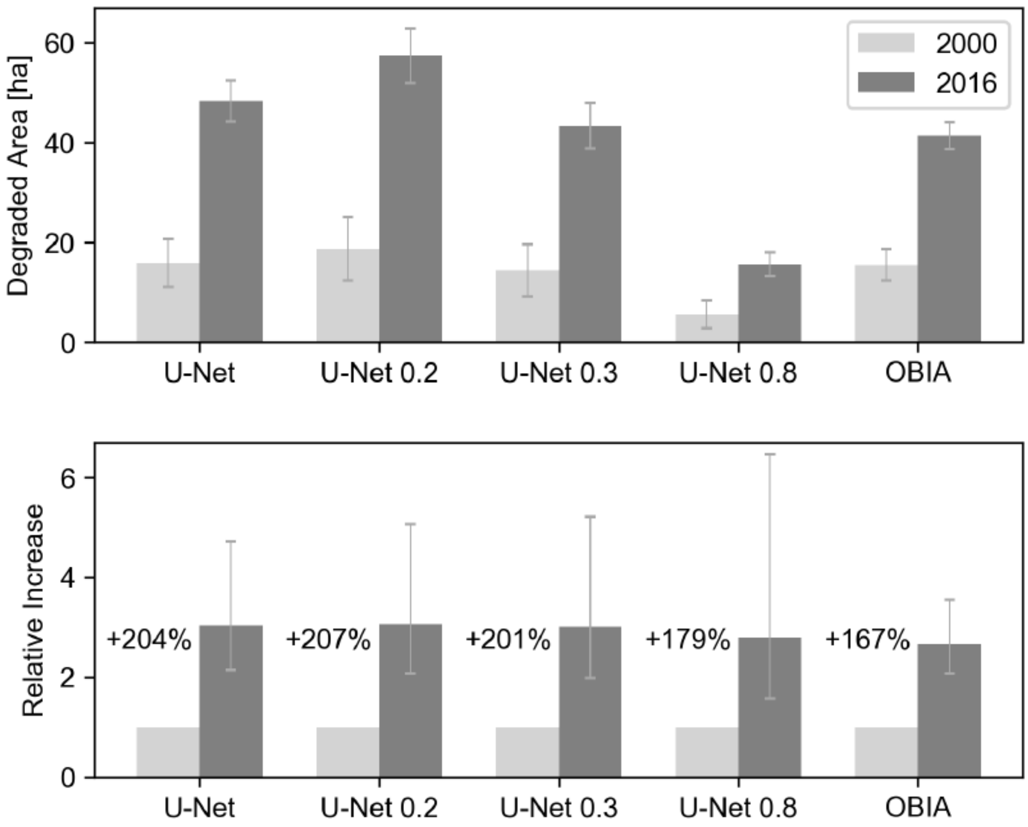

Figure 3.11: *Comparison of total degraded area in years 2000 and 2016 for the baseline (OBIA) and the U-Net approach with different thresholds. The total degraded area was obtained from the interpolation results of each year (top panel). In all approaches, an increase of degraded area in the Urseren Valley is observed with threshold-specific differences in the total extent. However, the relative increase in degraded area (bottom panel) shows that assessing the trend of soil degradation can be done independently of the threshold, as all results fall within the statistical uncertainty of the linear regression fit. Note that the statistical uncertainty for U-Net 0.8 increases due to the comparably small total degraded area detected. The error bars depict the statistical uncertainty of one standard deviation.*

For the individual erosion classes, we examine the results for the full U-Net model output and for a threshold of 0.3 (see Figure 3.12). Especially for sheet erosion and management effects, which contribute to a great amount of the total degraded area, the choice of 0.3 as a threshold for the hard segmentation is appropriate. In the case of livestock trails, the full-probability U-Net results capture the behaviour in the baseline more appropriately. The individual results highlight that an erosion-class-specific choice of the probability threshold can be reasonable in applications such as ours. We provide a result on such a mixture of thresholds for the linear trend for the years 2000 to 2016 such a mixture of thresholds in Supplementary Figure S2. The linear trend for the years 2000 to 2016 exhibits good agreement with the OBIA baseline (similar to Figure 3.10 on the right). Therefore, although the temporal development of aggregated measures is less dependent on the threshold, choosing different probability thresholds enables flexibility in the number of identified segments and segment boundaries in the U-Net approach. This is especially the case when examining the temporal development with regard to the degraded area per individual erosion class (Figure 3.12).

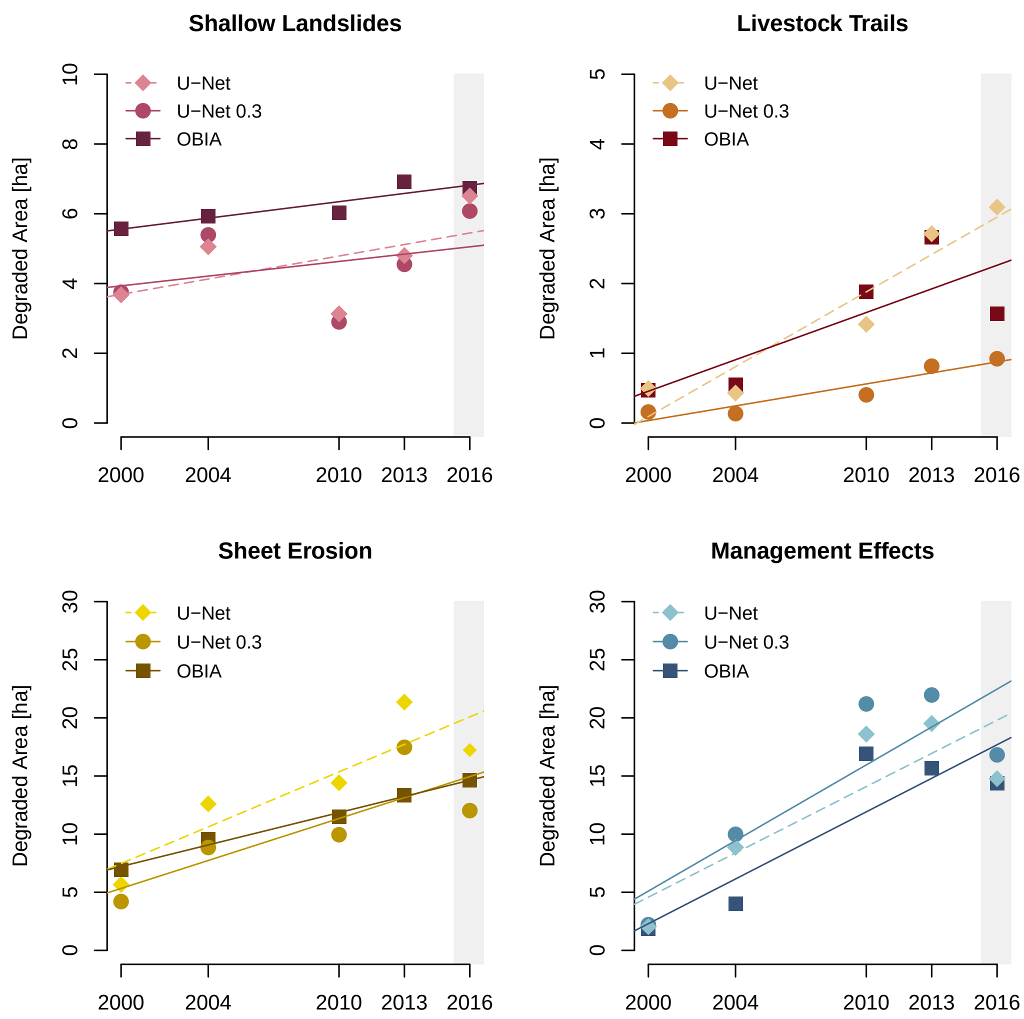

Figure 3.12: *Mapped degraded area in the test region by erosion class for both the OBIA and U-Net methods (full-probability results and threshold value 0.3). Comparing the two methods, class-specific differences for the yearly degraded area and linear trends can be observed. Moreover, by selecting appropriate thresholds for each erosion class, similar linear trends in both methods can be attained (see supplement Figure S2). The years 2000 to 2013 provide a result on the spatial generalisation of U-Net (years used for training), while the result for 2016 (shaded column) in addition provides a temporal generalisation result (aerial image of 2016 was not used for training).*

3.5.3 Deep Learning and OBIA

Deep learning methods for similar applications are predominantly trained with manual labels, and often the objects of interest are precisely defined, such as roads, buildings, or damaged trees in forests (Zhang et al., 2018b; Mboga et al., 2019; Hamdi et al., 2019). In our application, the objects are less clearly defined, and some of the segment boundaries concerning both the mapped and omitted areas might be more disputable. The boundaries of objects are often ambiguous due to smooth transitions, especially for erosion sites with reduced vegetation cover. Imprecise delineation of the objects of interest negatively impacts the generalisation capability and applicability of deep learning techniques, and can potentially be a limiting factor for this kind of approach. In particular, it can have a detrimental effect on the accuracy of the U-Net approach if the ground truth misses a great number of relevant objects. Therefore, we do not rely on manual labels of the objects of interest, which might suffer from subjective assessments, require labour-intensive work, and usually are unable to achieve pixel-level precision. Instead, we showcase that any kind of segmentation technique, such as OBIA in our study, can be used as a basis to provide training data to successfully employ a convolutional neural network for segmentation of natural features, such as the erosion sites in our application.

Similar studies have compared OBIA to deep learning approaches for the detection of landslides on remotely sensed data with the goal of enabling large-scale analysis. In Prakash et al. (2020) the comparison was done on the basis of landslide inventories. A study of different machine learning and deep learning methods was conducted by Ghorbanzadeh et al. (2019), who used field observations with manual corrections as the ground truth segments. These studies show that deep learning approaches improve segment detection by comparison of the segmentation performances of the different methods. In our study, we leverage the fact that OBIA is a well-suited approach for segmentation tasks on small scales, and thus derive our baseline trends and the ground truth segments from it. Other work like the detection of shrubs on high resolution satellite imagery by Guirado et al. (2017) similarly shows that CNN approaches can outperform OBIA in certain cases. That study relied on manually delineated ground truth segments and used dedicated pre-processing steps to identify regions of interest to perform classification of candidate patches. Combining OBIA and CNN approaches was also studied with regard to using CNNs in the classification step of the OBIA framework (Fu et al., 2019) or using features learned by the CNNs to improve inputs to the OBIA workflow (Pan et al., 2019). In our study, OBIA provides the necessary high-quality ground truth segmentation, but our workflow is not bound to OBIA, and any other reliable approach can be used for this too.

The presented results of this study substantiate that the U-Net approach can perform on a par with OBIA. Moreover, the transferability to new data, the insensitivity of trends in aggregated measures to threshold selection, and the flexibility of fitting the U-Net results to existing knowledge or competing segmentation methods—apart from manual inspection of segmentation results—render the proposed approach advantageous for a great variety of applications. Furthermore, large-scale analysis is facilitated by improved running times. For training and prediction, a Nvidia GeForce Titan X Pascal GPU was used. In our study, training required a running time of approximately 6.5 h, while the prediction for the full Urseren Valley took 12 min. This is a significant improvement over the semi-automatic OBIA approach, which takes up to a few days to achieve satisfying results for the Urseren Valley. For large-scale studies (e.g., alpine-wide analysis) the process can efficiently be parallelised using several GPUs, resulting in even faster prediction times.

3.6 Conclusions

While OBIA is the state-of-the-art approach for mapping objects on remotely sensed images, it suffers from limitations that render this approach unsuitable for larger-scale studies. High-quality segmentation results come at the expense of a lack of transferability of parameter settings from one input image to another, manual adjustments, and a need for expert knowledge in applying the method to the specific task which together lead to long processing times. In particular, the first aspect generally hinders OBIA in a predictive setting for new images. To overcome these shortcomings and enable large-scale analysis, we compared OBIA to a fully convolutional neural network approach which learns relevant features for segmentation by itself and thereby emulates some of the expert knowledge necessary to apply OBIA. We demonstrated that the U-Net approach is capable of performing as well as OBIA with respect to identifying trends in the spatial and temporal development of degraded soil, and can therefore replace OBIA in large-scale studies. Spatial patterns and temporal trends of both methods agree well; nevertheless, some generated segmentation results might partially not overlap ($F_1 = 78\%$). Specifically, we show that U-Net (threshold 0.3) provides a potentially more accurate relative increase of total degraded area in the Urseren Valley than the more conservative estimates of OBIA (201% vs. 167%). This novel approach allows for individual threshold choices for the most successful representation of ongoing soil erosion processes. This is typically possible if some prior knowledge about erosion processes and the spatial extent of degraded soil is available, or if visual assessment is feasible, to which probability thresholds can be calibrated. In our study, we made use of training labels generated with OBIA. However, any kind of (high-)quality training labels can be used, and the U-Net erosion site segmentation is not limited to combined use with OBIA. In summary, we show that with our approach we can perform erosion site prediction close to similar approaches such as OBIA which provide accurate segmentation results on small scales. A particular strength of the proposed approach is that similar trends are achieved with a more efficient, automatic, and objective method for mapping erosion sites. We require the U-Net approach to be trained only once and obtain much better transferability of the method to new images. Moreover, the approach is insensitive to the threshold choice with respect to trends of aggregated measures, and the improved running times make large-scale analysis of soil erosion is Swiss alpine grasslands feasible.

Still, our model is only as good as the training data; i.e., high-quality training data are important for adequate U-Net performance. Future studies should include a variety of different sample regions to incorporate relevant erosion-type-specific conditions during training (e.g., orientation of erosion sites). Furthermore, U-Net can use as many layers of information as required. A unique feature of fully convolutional neural networks is that inputs of any size and any number of channels can be used, i.e., RGB images with DTM derivatives. Additional maps can be easily incorporated (see Figure 3.5), which might include more information, such as environmental properties or images with additional spectral information. In that regard, U-Net has the advantage of continual learning; i.e., it can be trained further to incorporate conditions of completely new regions and erosion-type-specific properties. Generally, the U-Net model can be employed in a similar fashion for other segmentation tasks in remote sensing and other inputs, such as UAV or satellite imagery. The requirement for the input data is that the spatial resolution allows for identifying the target objects well enough.

Acknowledgements

The authors would like to thank the Swiss National Science Foundation for supporting the research. Calculations were performed at sciCORE (`http://scicore.unibas.ch/`) scientific computing core facility at University of Basel. We also want to acknowledge Swisstopo and MeteoSwiss for providing the data sets we used. Furthermore, we would like to thank the anonymous reviewers for their comments and suggestions which helped us to improve the paper.

High Alpine Landscape
Photo: Max Itin

4

Investigating Causal Factors of Shallow Landslides in Grassland Regions of Switzerland

Abstract

Mountainous grassland slopes can be severely affected by soil erosion, among which shallow landslides are a crucial process, indicating instability of slopes. We determine the locations of shallow landslides across different sites to better understand regional differences and to identify their triggering causal factors. Ten sites across Switzerland located in the Alps (8 sites), in foothill regions (1 site), and the Jura mountains (1 site) were selected for statistical evaluations. For the shallow landslide inventory, we used aerial images (0.25 m) with a deep learning approach (U-Net) to map the locations of eroded sites. We used logistic regression with a Group Lasso variable selection method to identify important explanatory variables for predicting the mapped shallow landslides. The set of variables consists of traditional susceptibility modelling factors and climate-related factors to represent local as well as cross-regional conditions. This set of explanatory variables (predictors) are used to develop individual site models (local evaluation) as well as an all-in-one model (cross-regional evaluation) using all shallow landslide points simultaneously. While the local conditions of the ten sites lead to different variable selections, consistently slope and aspect were selected as the essential explanatory variables of shallow landslide susceptibility. Accuracy scores range between 70.2 and 79.8% for individual site models. The all-in-one model confirms these findings by selecting slope, aspect as well as roughness as the most important explanatory variables (Accuracy = 72.3%). Our finding suggest that traditional susceptibility variables describing geomorphological and geological conditions yield satisfactory results for all tested regions. However, for two sites with lower model accuracy, important processes may be under-represented with the available explanatory variables. The regression models for sites with an east-west oriented valley axis performed slightly better than models for north-south oriented valleys, which may be due to the influence of exposition related processes. Additionally, model performance is higher for Alpine sites, suggesting that core explanatory variables are understood for these areas.

Study published as Zweifel, L., Samarin, M., Meusburger, K., Alewell, C., 2021. *Investigating Causal Factors of Shallow Landslides in Grassland Regions of Switzerland.* Nat. Hazards Earth Syst. Sci. 1-24.

4.1 Introduction

Soil erosion is an issue affecting many regions of the world and can have severe consequences for the environment and humanity (e.g., water pollution or food production) (Pimentel et al., 1995; Pimentel and Burgess, 2013; O'Mara, 2012; Alewell et al., 2009, 2020). In Switzerland, grasslands of mountain and hill slopes can be strongly affected by soil erosion, which can be caused by natural (e.g., precipitation events) and anthropogenic processes (e.g., land-use management) (Tasser et al., 2003; Meusburger and Alewell, 2008; Zweifel et al., 2019; Geitner et al., 2021; Lepeška, 2016). The most visible form of erosion in grassland soils showing bare soil areas can be categorised as shallow erosion (Geitner et al., 2021) (Figure 4.1). These shallow erosion sites are mainly triggered by prolonged and intense rainfall events (shallow landslides) or through abrasion by snow (snow gliding, avalanches) (Wiegand and Geitner, 2010b; Geitner et al., 2021). However, in many cases, a combination of these processes can lead to shallow erosion sites and triggering processes cannot be distinguished from aerial photos. Therefore, we use the term *shallow landslides* in our regions and the frame of this study with no implication of the triggering event.

Figure 4.1: *Images showing examples of shallow landslides. Shallow landslide sites show displaced topsoil layers and have a distinct boundary to the vegetation. A) taken in the Urseren valley showing a larger section of a south-east facing slope area affected by many shallow landslides (light coloured patches). B) taken in Val Piora showing a close up of a shallow landslide facing south. C) showing an image taken with a UAV in Val Piora with an approximate length of 10m.*

The aim of our study is to statistically evaluate shallow landslide occurrence for 10 different sites (between 16 and 54 km^2) across Switzerland. In the past, shallow landslide susceptibility studies have mainly focused on one or two study sites while often testing multiple modelling techniques (Gómez and Kavzoglu, 2005; Meusburger and Alewell, 2009; Vorpahl et al., 2012; Tien Bui et al., 2016; Oh and Lee, 2017; Lee et al., 2020; Nhu et al., 2020a) except for Persichillo et al. (2017), who evaluated four sites in different catchments. For our shallow landslide inventory we map the eroded sites on aerial images (0.25 m resolution) using a *U-Net* deep learning approach (Ronneberger et al., 2015). The U-Net tool was trained by Samarin et al. (2020) to identify and map the extent of soil erosion features on grassland. While this mapping tool is able to distinguish between different erosion processes/appearances (i.e., shallow landslides, livestock trails, sheet erosion and management effects Samarin et al. (2020)), here, we focus on shallow landslides, as we aim to understand their causal factors and spatial patterns better. With the U-Net mapping tool, we can identify locations of shallow landslides in a very efficient and precise manner, increasing the possibilities for mapping but also future model validation of soil erosion studies (Samarin et al., 2020). The mapped shallow landslide sites are subsequently evaluated with a statistical model to identify the most important explanatory variables and gain a better understanding of causal factors as well as regional differences. For this purpose we use the *Group Lasso* approach for logistic regressions (Tibshirani, 1996; Yuan and Lin, 2006; Meier et al., 2008). The Group Lasso can deal with continuous and categorical variables and is able to estimate coefficients of classes within a categorical variable. In addition to estimating coefficients, the Lasso can do variable selection simultaneously (Section 4.3.2). The Lasso tends to yield sparse and interpretable models, avoids over-fitting and is tolerant towards possible collinearity of variables (Dormann et al., 2013). Despite these advantages, the Lasso has only been applied a small number of times for landslide susceptibility modelling (Camilo et al., 2017; Lombardo and Mai, 2018; Amato et al., 2019; Gao et al., 2020; Lombardo and Tanyas, 2021; Tanyaş et al., 2021). We evaluate the shallow landslides within each study site (10 models) and across all 10 study sites simultaneously (all-in-one model) and consider only grassland surfaces. Our aim is to identify explanatory variables that have local importance but also identify variables, which may explain regional differences in shallow landslide occurrence. The selected study sites are a combination of alpine (above 1500 m asl), foothill regions (below 1500 m asl) as well as one site in the Jura mountains (below 1500 m asl). The explanatory variables we use are the same for all sites and consist of a combination of classic landslide susceptibility variables (Budimir et al., 2015) as well as climate-related variables (Karger et al., 2017, 2018), which may aid in explaining regional differences of shallow landslide occurrence (Section 4.4.2). To understand how well the selected variables and their coefficients perform, we evaluate the models on held-out test data. We determine Receiver-Operator-Characteristics (ROC) curves and the corresponding Area-Under-Curve (AUC) as well as the Brier score, which is suitable for binary variables (presence/absence shallow landslides) (Section 4.3.3).

4.2 Study Sites

A total of 10 sites were selected to produce shallow landslide inventories (mapping of shallow landslides) and perform subsequent statistical evaluations of explanatory variables. We only consider grassland areas, which were identified with the aid of the surface cover information of the product *SwissTLM* (Swisstopo, 2019). The sites were selected to represent different mountain and hill regions and different geological conditions, valley expositions and slope angles. Figure 4.2 shows the locations of all study sites within Switzerland, and Table 4.1 summarises important site information. Most permanent grassland surfaces in Swiss mountain regions are used either for grazing (pastures) or haying (meadows) (FSO, 2013; Stumpf et al., 2020). Of the 10 sites, nine are located across the Swiss Alps, and one was selected in the Swiss Jura mountains (Baulmes, below 1500 m asl). The sites located in the Swiss Alps represent a range of alpine (above 1500 m asl) regions as well as foothill regions (Hornbachtal, below 1500 m asl). Val Cluozza is located in the Swiss National park and shows no signs of anthropogenic influences, and also contains only a small amount of grassland area (8%, rest mostly shrubs and rocks). For other sites in the Alps, grassland covers 34-55 % of the valley. The rest of the land-cover consists of forest area, rock/debris area or, in some cases, urban areas. The shallow landslide densities (shallow landslide affected area in relation to total grassland surfaces) range from 0.06% (Baulmes) to 2.31% (Chrauchtal). Figure 4.2 shows the locations of all study sites within Switzerland and Table 4.1 summarises important site information.

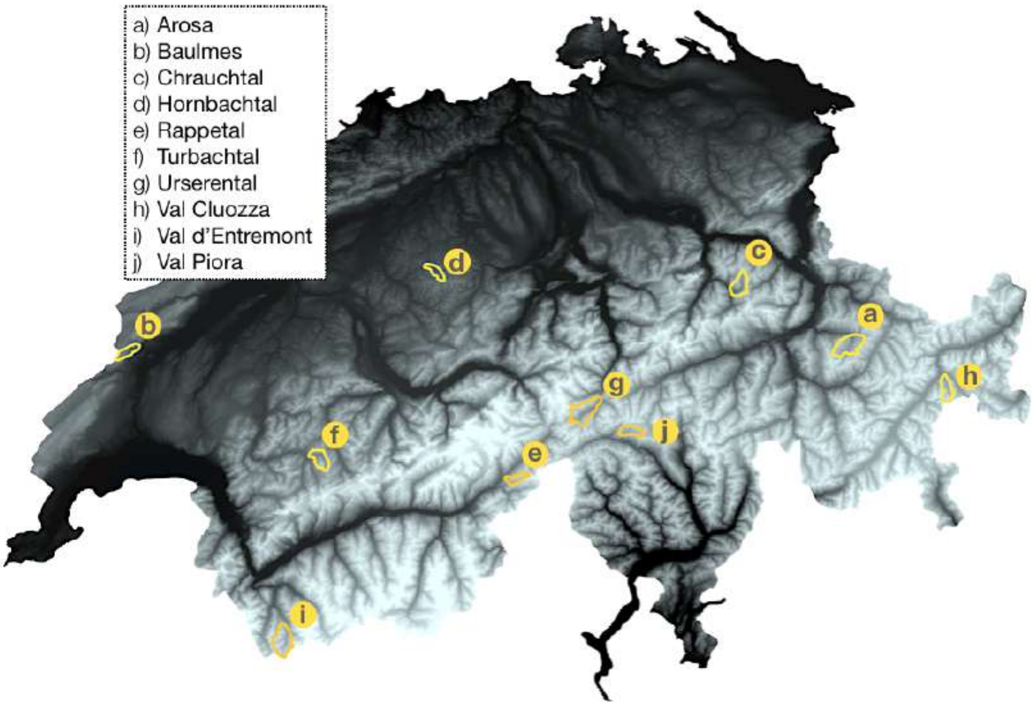

Figure 4.2: *Map of Switzerland showing the 10 selected study sites (outlined in yellow). Colours of the map show lower elevations in dark and higher elevations in lighter colours. Digital terrain model obtained from © swisstopo.*

Table 4.1: *List of Study sites and descriptive information: Elevation range, Total area of the study site, Grassland area within study site in percent, average slope of grassland area, orientation of the main valley axis, number of shallow landslides and shallow landslide density on grassland areas. The max. precipitation events (monthly values) of the previous 5 and 10 years are averaged over the study site. Note that both time spans might include the same events. GL = Grassland, SLS = Shallow Landslides, P = Precipitation.*

Study Site	Year of Image	Elevation (m asl)	Total Area	GL %	GL Slope average	Orient. of Valley	No. SLS $\geq 4m^2$	GL SLS Density	P. max. 5 years	P. max. 10 years
Arosa	2014	1613 - 2535	50 km^2	34 %	20.8°	NNE-SSW	896	0.24 %	281 mm	284 mm
Baulmes	2014	615 - 1512	21 km^2	19 %	14.5°	NE-SW	26	0.06 %	306 mm	306 mm
Chrauchtal	2014	1421 - 2432	32 km^2	53 %	27.2°	N-S	8073	2.31 %	378 mm	378 mm
Hornbach	2015	800 - 1256	17 km^2	35 %	21.7°	NW-SE	438	0.52 %	323 mm	368 mm
Rappetal	2015	1427 - 2533	16 km^2	50 %	27.4°	NE-SW	1023	0.54 %	384 mm	384 mm
Turbach	2013	1208 - 2367	28 km^2	55 %	25.7°	NNW-SSE	3010	0.97 %	432 mm	432 mm
Urseren	2013	1514 - 2840	54 km^2	48 %	25.1°	NE-SW	3702	0.70 %	293 mm	295 mm
Val Cluozza	2015	1643 - 2603	25 km^2	8 %	30.5°	N-S	177	0.46 %	181 mm	218 mm
Val d'Ent.	2013	1808 - 2823	50 km^2	44 %	24.5°	N-S	1823	0.41 %	410 mm	410 mm
Val Piora	2015	1848 - 2554	21 km^2	43 %	20.8°	E-W	1116	0.49 %	322 mm	347 mm

4.3 Methodology

4.3.1 Shallow Landslides Inventory

To identify the locations of shallow landslides across the 10 study sites, we use a deep learning approach based on the U-Net architecture (Ronneberger et al., 2015). These mapped shallow landslides are then used for statistical evaluations of causal factors (Section 4.3.2). This fully convolutional neural network approach for semantic segmentation in images allows for objective and efficient mapping. The U-Net model was trained to identify and map erosion sites on aerial images (Swisstopo, 2010) with the aid of digital terrain model information (Swisstopo, 2014), as described in Samarin et al. (2020). The U-Net model was trained on a small area of 9 km^2 and tested on an area of 17 km^2 in the Urseren Valley (Samarin et al., 2020). For this study we use the same U-Net model without further training to map the new study sites and focus only on the erosion class *shallow landslides*, as defined in the introduction. The mapping results were carefully examined for all study areas and corrected manually when necessary. The trained U-Net used in this study has an overall precision of 73%, a recall of 84%, and a F1-score of 78% (Samarin et al., 2020). We only consider shallow landslides of at least 4 m^2 located on grassland (see Figure 4.4 for examples of mapping results and in the supplemental material Figure S11 for an example of one fully mapped study site).

4.3.2 Logistic Regression with Group Lasso

With the statistical evaluation of the shallow landslide sites, we aim to understand possible causal factors. We evaluate the 10 study sites individually (evaluation within each site) as well as across all of the sites simultaneously (all-in-one model). The aim of this is to test, whether the same causal factors are important on different spatial scales. For each of the 10 sites an equal number of shallow landslide and non-landslide points constitute the binary response variable (no=0, yes=1) with a set of corresponding explanatory variables (see Section 4.4). Our aim is to use a method that generates sparse models that are easy to interpret and avoid over-fitting. To achieve this, we use a logistic regression estimated with the *Least Absolute Shrinkage Selection Operator* (Lasso) (Tibshirani, 1996). The Lasso regression performs variable selection and coefficient estimation simultaneously. This is obtained by applying a penalty term (II.) to the log-likelihood function of the logistic regression (I.) (Hastie et al., 2016):

$$\ell_\lambda(\beta) = \underbrace{-\sum_{i=1}^{n}(y_i z_\beta(\mathbf{x}_i) - \log(1+e^{z_\beta(\mathbf{x_i})}))}_{I.} + \lambda \underbrace{\sum_{j=1}^{p}|\beta_j|}_{II.}. \tag{4.1}$$

We consider the linear model $z_\beta(\mathbf{x}) = \beta_0 + \sum_{j=1}^{p}\beta_j x_j$ on a data set of size n with p features, i.e. $x_i \in \mathbb{R}^p$, and binary response $y_i \in \{0,1\}$. The penalty term is determined by the parameter λ which is estimated by minimising the model error. The weight of λ determines how many variables are selected, and in turn, the model shrinks coefficients of variables that contribute to the error (Hastie et al., 2009, 2016). By shrinking the coefficients of unimportant variables to zero, they are removed from the model and thereby variable selection is performed. To achieve the least complex model in terms of selected variables, we chose λ to be one standard error larger than the minimal mean square error (Hastie et al., 2009). As some of the explanatory variables are categorical (i.e., geology, aspect) we use the *Group Lasso* approach. All levels within a categorical variable (encoded as dummy variables) are treated as a group and all coefficients within that group become zero (dismissed) or non-zero (selected) simultaneously (Yuan and Lin, 2006; Hastie et al., 2016). This leads to a new objective function with modified penalty term,

$$\ell_\lambda(\beta) = -\sum_{i=1}^{n}(y_i z_\beta(\mathbf{x}_i) - \log(1+e^{z_\beta(\mathbf{x_i})})) + \lambda \sum_{g=1}^{G}\alpha_g\|\beta_g\|_{G_g}, \tag{4.2}$$

where α_g is a scaling factor depending on the number of parameters in β_g and $\|\eta\|_K = (\eta^T K \eta)^{1/2}$ is a norm depending on the group structure of the G different groups. For more details on the

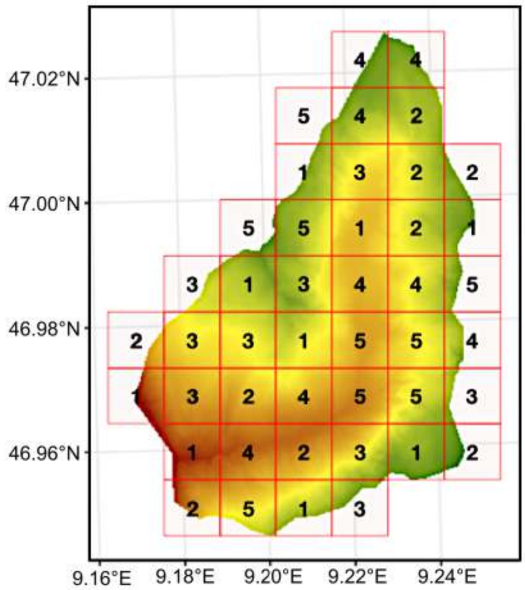

Figure 4.3: *Spatial blocks for 5-fold cross-validation shown with the example of Chrauchtal. Blocks have a size of 1 km^2. Blocks are assigned randomly and determined with the R-package blockCV (Valavi et al., 2019).*

mathematical extension of the Group Lasso we refer to Meier et al. (2008). We implement the Group Lasso for logistic regression with the R-package *grpreg* (Breheny and Huang, 2015). Due to the spatial relationship of geographic data sets, we divide the data into spatially separated blocks of 1 km^2, randomly numbered from 1 to 5 (Valavi et al., 2019) (see Figure 4.3). These blocks are used for 5-fold cross-validation of the model. Every block is held out once for testing, while the others are used for model training (e.g., while blocks labeled with 2/3/4/5 are used for training, blocks labeled with 1 are used for model testing). During each fold, coefficients are estimated for the explanatory variables. Note that the explanatory variables have been standardised to allow for easier comparisons between variables. The estimated values of the coefficients, therefore, give an indication of their relative importance to model the response variable (shallow landslide and non-shallow landslide points). With higher absolute values of an estimated coefficient, the influence of this explanatory variable is stronger. A linear transformation would be performed to ultimately get the coefficients for the variables on their original scale (Lombardo and Mai, 2018). The process of coefficient estimation is repeated 20 times (bootstrapping) with different randomly selected blocks, generating 100 estimates of coefficients for every site (20 times 5-fold cross-validation) (Goetz et al., 2015; Steger et al., 2016). We assess the model-selected coefficients by evaluating the range of the coefficient estimates (boxplots) as well as their inclusion rate (number of times selected by models) as the number of ideal variables can vary in each fold.

4.3.3 Model Evaluation

To evaluate the accuracy and the predictive ability of the logistic regression models, we use performance measures described in the following. All model performances are based on test set estimations (predictions evaluated on held-out test data blocks). The Receiver-Operator-Characteristic (ROC) curve is a continuous curve showing the relationship between the True Positive Rate (TPR) and False Positive Rate (FPR) for every probability threshold of the model predictions (Hosmer and Lemeshow, 2000). The accompanying Area-Under-Curve (AUC) is the integrated area under the ROC curve and describes the model skill across all possible probability thresholds. Values of the AUC above 0.5 (equivalent to a random model) are better, while a score of 1 indicates a perfect model. Additionally, we compute confusion matrix performance scores for a fixed probability prediction threshold of 50 %. To summarise the accuracy of the models, we assess the magnitude of the error in the probability predictions using the Brier score (BS) (Equation 4.3) (Brier, 1950; Wilks, 2006).

$$BS = \frac{1}{N}\sum_{t=1}^{N}(f_t - o_t)^2, \tag{4.3}$$

where N are the number of mapped shallow landslides, f_t are the predicted probabilities for shallow landslide occurrence (between 0 or 1), and o_t are the observed (mapped) of shallow landslides (either no=0 or yes=1). The Brier score (BS) is equivalent to the Mean-squared error, yet is valid for binary observations. A BS of zero indicates perfect model performance, while 1 is the worst possible score (prediction is opposite of observation). Probability predictions that are further away from the observation are penalised more heavily. If the model predicts a 50 % chance of shallow landslide every time (random), a score of 0.25 is achieved for a balanced data set (Steyerberg et al., 2010; Raja et al., 2017). We re-estimate the BS with bootstrapping (500 repetitions, sampled with replacement) to achieve confidence intervals.

4.4 Data Sets

4.4.1 Shallow Landslide and Non-Landslide Points

To perform the mapping of shallow landslide sites with the U-Net model (Section 4.3.1), we require aerial (ortho-)images (SwissImage, Swisstopo (2010)) and a digital terrain model (DTM; SwissALTI, Swisstopo (2014)). The aerial images have a spatial resolution of 0.25 m and red, green and blue spectral bands. The aerial images for the study sites were collected during the years 2013 (Turbach, Urseren, Val d'Entremont), 2014 (Arosa, Baulmes, Chrauchtal) and 2015 (Hornbach, Rappetal, Val Cluozza, Val Piora). From the DTM, the derivatives slope, aspect and curvature (plan and profile) are required, which are calculated with ArcGIS (10.5). Additionally, we use data set with land-cover information (SwissTLM, Swisstopo (2019)) to assure only sites with grassland are being mapped. For the mapped shallow landslides, we extract the centre points with ArcGIS of sites with a minimum size of 4 m^2. Non-landslide points were extracted randomly within the grassland area and with a minimum buffer distance to mapped shallow landslides of 5 m. This shallow landslide data set contains an equal number of landslide to non-landslide points for each study site (Figure 4.4) (Frattini et al., 2010; Petschko et al., 2014).

4.4.2 Explanatory Variables

The explanatory variables selected for the statistical evaluation of the shallow landslide points are a combination of variables commonly found in landslide or shallow landslide susceptibility studies (Budimir et al., 2015; Chen et al., 2017; Cignetti et al., 2019; Kavzoglu et al., 2014; Lee et al., 2020; Meusburger and Alewell, 2009; Persichillo et al., 2017; Nhu et al., 2020b,a) and climate-related variables that may explain differences between the sites (e.g., strong precipitation events) from the

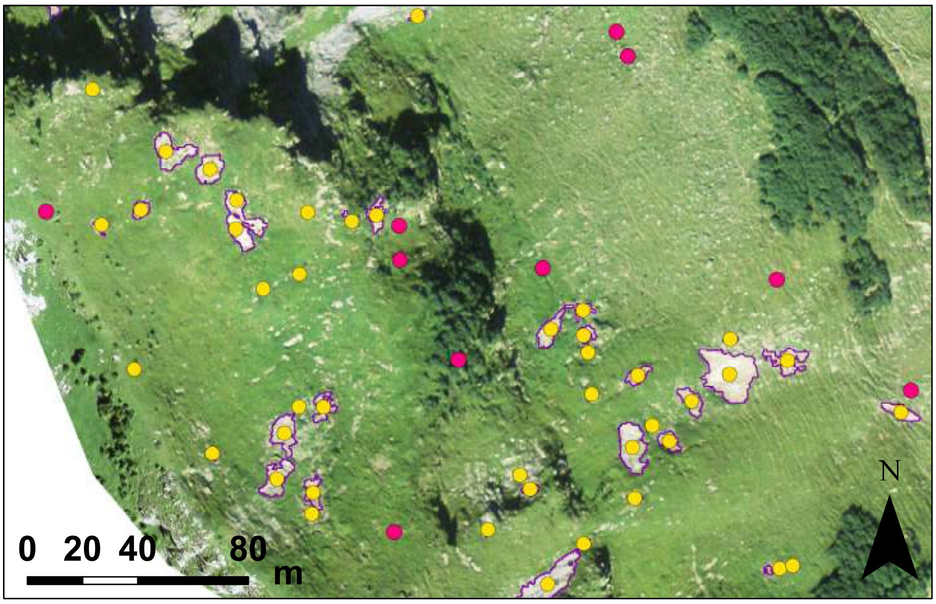

Figure 4.4: *Example of mapped shallow landslides in the Turbach valley (purple). The centred points (yellow) represent shallow landslide locations for the Lasso model evaluation. Only sites with an area larger than 4 m^2 were used for the evaluation. Red points represent randomised non-landslide points. Aerial image (2013) obtained from © swisstopo.*

Table 4.2: *Table containing the variables used for the logistic regression with information on the type of variable (continuous/categorical), spatial resolution and which data set the variable was originally based on.*

Variable	Type	Resolution	Based on
Elevation	continuous	2 m	SwissALTI
Slope Gradient	cont.	2 m	SwissALTI
Curvature plan	cont.	2 m	SwissALTI
Curvature profile	cont.	2 m	SwissALTI
Roughness	cont.	2 m	SwissALTI
Flow Accumulation	cont.	2 m	SwissALTI
Topographic Wetness Index	cont.	2 m	SwissALTI
Distance to Roads	cont.	10 m	SwissTLM
Distance to Streams	cont.	10 m	SwissTLM
Road Density (500 m radius)	cont.	25 m	SwissTLM
Stream Density (500 m radius)	cont.	25 m	SwissTLM
Max. Precipitation Event (10 y)	cont.	1 km	CHELSA
Max. Precipitation Event (5 y)	cont.	1 km	CHELSA
Snow Days	cont.	1 km	CHELSA
Snow Cover Days	cont.	1 km	CHELSA
Growing Season Length	cont.	1 km	CHELSA
Frost Change Frequency	cont.	1 km	CHELSA
Geology (4 classes)	categorical	1:500’000	Geological Map
Aspect (8 classes)	cat.	2 m	SwissALTI

CHELSA data set (Karger et al., 2017, 2018). Variables related to land-cover and vegetation are not considered as we filter our study sites to contain only grassland areas.

For every shallow landslide and non-landslide point the variables listed in Table 4.2 were extracted. The same variables are used for evaluating all 10 sites as well as the all-in-one model. The continuous variables have been standardized to allow for comparing coefficients of variables. The categorical variables were converted in to dummy variables (all classes of a categorical variable encoded as 0 or 1). Most variables can be derived from the DTM (elevation values, SwissALTI) which has a spatial resolution of 2 m. *Slope* (in degrees) describes the maximum change in elevation to neighboring cells. *Aspect* is included as a categorical variable containing eight exposition sectors (North, North-East, East, South-East, South, South-West, West, and North-West). For *Curvature* we use *plan* and *profile*. Plan curvature describes the slopes concave (positive values) or convex (negative values) properties perpendicular to the direction of the maximum slope, while profile curvature indicates the same but parallel to the maximum slope. A value of zero indicates a flat surface. Plan curvature characterizes the convergence and divergence of surface flow and profile curvature describes the acceleration of the surface flow (Zevenbergen and C., 1987). *Roughness* expresses the difference between maximum and minimum elevation values between a cell and all of its neighboring cells (Wilson et al., 2007). Higher roughness values indicate rougher terrain. Based on flow direction (direction of the steepest descent) we determine the *Flow Accumulation*, which describes the number of cells flowing into a cell. The *Topographic Wetness Index TWI* gives indications of where water accumulates on slopes and is calculated with $\ln(\alpha/\tan\beta)$, where α is the upslope area draining through a certain point per unit contour length (Flow Accumulation) and β is the slope (Beven and Kirkby, 1979). *Distance to Roads* and *Road Density* are variables that are often included in landslide susceptibility studies, as they represent constructional interference (Meusburger and Alewell, 2009; Nhu et al., 2020a). *Distance to Streams* and *Stream Density* can give further information on rainfall drainage and runoff processes (Nhu et al., 2020a). These variables were calculated based on the SwissTLM data set (Swisstopo, 2019), containing information on road and stream locations using the distance and line density tool (search radius of 500m (Meusburger and Alewell, 2009)) of ArcGIS. In addition to these terrain-related variables, we use variables derived from the *CHELSA* data set, which contains monthly values on temperature and precipitation from which many environmental parameters are derived (Karger et al., 2017, 2018). We include the strongest precipitation events of the last 5 years and 10 years prior to the recording year of the aerial images, information on snow fall/cover, growing season length and frost change frequency (5-year average of 2009-2013). While these variables have a comparatively low spatial resolution (30 arc sec, approx. 1 km), they may give a good indication of regional differences of shallow landslide occurrence as they are representative of alpine processes often linked to the triggering of shallow landslides (Meusburger and Alewell, 2008; Wiegand and Geitner, 2010b; Löbmann et al., 2020; Geitner et al., 2021). Specifics on the individual CHELSA variables used can be found in Karger and Zimmermann (2019). Since we analyse 10 different sites as well as all sites in one model, we select a simplified geological data set containing only the three main rock formation classes (igneous, metamorphic, sedimentary) and unconsolidated rocks. This reduces the number of classes in the categorical variable and increases the interpretability of the model, especially when comparing between sites.

4.5 Results and Discussion

The Lasso regression model selects the relevant explanatory variables and estimates their regression coefficients to predict the location of shallow landslides. The statistical evaluation was conducted for all 10 sites individually and for all sites combined in to one large model (all-in-one model). The same explanatory variables were used for both approaches. Due to the 5-fold cross-validation and random re-sampling of 20 times (bootstrapping), the coefficients are estimated 100 times. The *estimated coefficients* should be analysed in combination with the *variable inclusion rate*, which describes how many times the explanatory variable was selected by the Lasso regression model selected the explanatory variables (100 = selected every time) and gives an indication of the importance of the variable.

4.5.1 Individual Site Models

The statistical evaluation of the study sites yields one model per site (10 models). We combine the results of all 10 sites in heat-maps, showing the median estimated coefficients (Figure 4.5) and their inclusion rate (Figure 4.6).

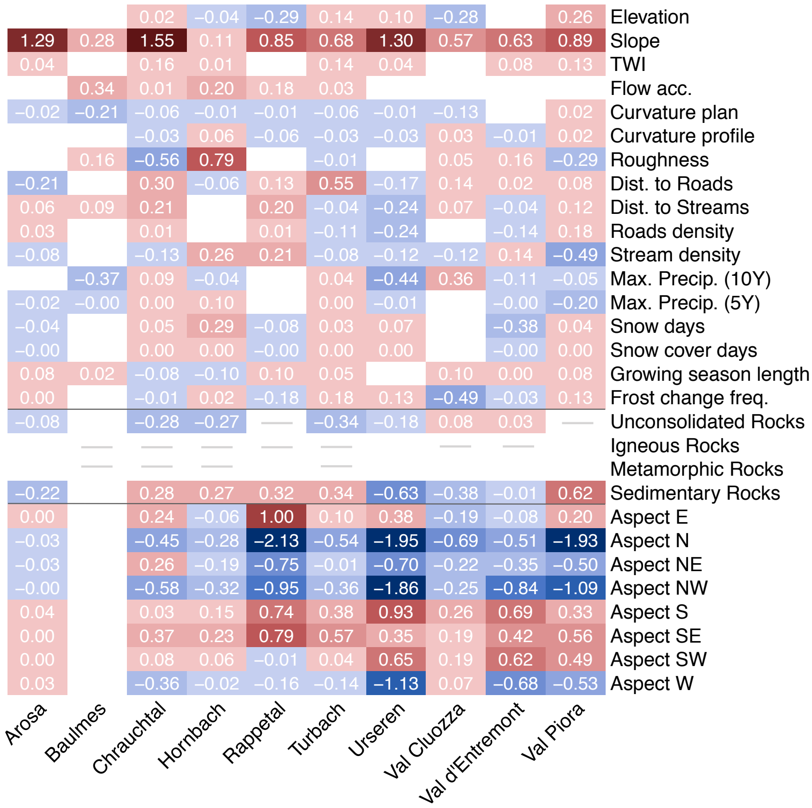

Figure 4.5: *Heat-map displaying estimates of coefficients (median of 100 estimates) for all 10 sites. Note that not all geological rock classes are present at all sites (grey line). White boxes are equivalent to coefficients of zero and were therefore never selected for the models.*

Most sites select slope as the most important variable in terms of coefficient value as well as the inclusion rate. Only the sites Baulmes (29 %) and Hornbach (19 %) rarely select slope and shrink the value of the coefficient towards zero. These sites are both located outside of the Alpine region (Jura mountains and the foothills of the Alps) and on average, have gentler slopes (Baulmes 14° and Hornbach 21°). Steeper slopes tend to be more susceptible to shallow landslides, which is in agreement with other studies that have found slope to be one of their top predictors (Budimir et al., 2015; Goetz et al., 2015; Tien Bui et al., 2016; Oh and Lee, 2017; Persichillo et al., 2017; Lombardo and Mai, 2018; Lee et al., 2020; Nhu et al., 2020b,a).

The aspect was selected most times (84-100 %) for all sites except for Arosa (4 %) and Baulmes (0 %) (Figure 4.6). In Baulmes, this may relate to the fact that there are only 26 mapped shallow landslides

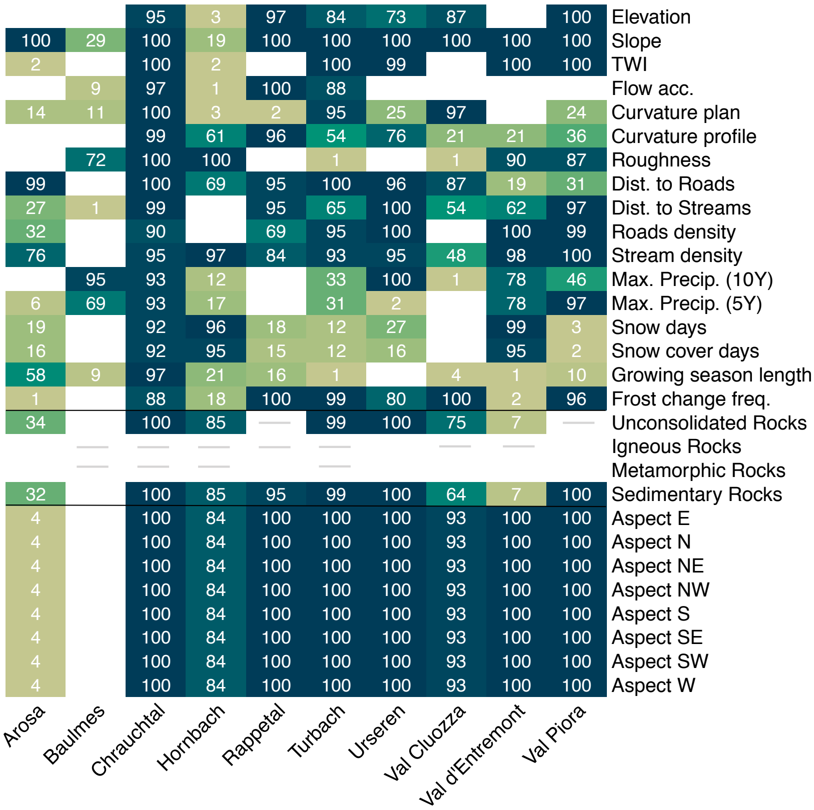

Figure 4.6: *Heat-map displaying the inclusion rate of variables for all 10 sites. The numbers indicate how often variables were selected for the models out of 100 estimates. Note that not all geological rock classes are present at all sites (grey line). Darker colors show variables selected more often. White boxes indicate which variables were never selected for the models.*

available and that all grassland areas in the valley are located on the south-east facing slope, which includes non-landslide points. The rest of this site is covered with forest, which was not considered for our evaluation. Arosa is located in a wide circular-shaped valley with no dominant slope expositions, and no typical aspect for shallow landslides is present. For the remaining eight sites, the sectors ranging from W to NE are strong indicators of no shallow landslides occurring, while E to SW facing slopes are favourable for shallow landslides (Persichillo et al., 2017; Lombardo and Mai, 2018) . The coefficient size of the individual aspect sectors varies slightly from site to site, indicating that aspect may be more predictive in some areas (e.g., Urseren or Val Piora) than in others (e.g., Hornbach or Val Cluozza).

Other important variables, which show a high inclusion rate amongst most sites, yet often do not have a large impact concerning the coefficient values, are Roughness, TWI, Distance to Roads/Streams, Road/Stream Density and Frost Change Frequency. However, these variables were disregarded for some of the sites (low inclusion rates or even excluded completely). The coefficients' values may have a negative or positive correlation to shallow landslide points (SLS points), depending on the sites and the local conditions. Geology is important for most sites, while either sedimentary rocks and unconsolidated rocks are present at the sites or selected for the model from all available classes. Unconsolidated rocks are negatively correlated in most cases. They can often be found near the valley bottom in proximity to streams and lakes, which tend to be located outside of shallow landslide zones. Sedimentary rocks are positively correlated in most cases, but can also show a negative correlation, depending on the site.

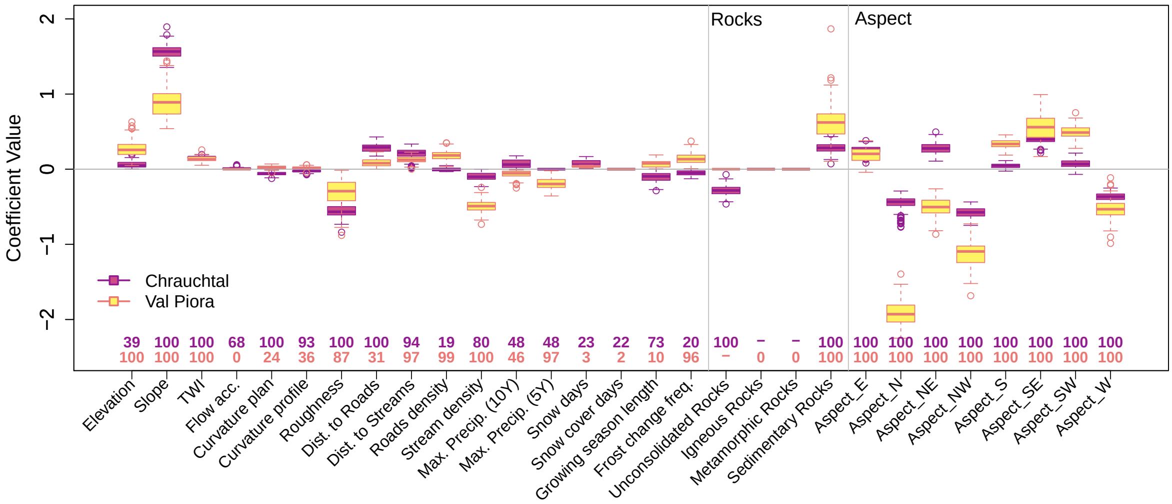

Figure 4.7: *Boxplots (with whiskers and outliers) showing the coefficient range with 100 repetitions. Numbers above variable names indicate the number of times it was selected for the model. Boxes show the interquartile range (25th and 75th percentile), and the line indicates the median of the coefficients. Chrauchtal and Val Piora are selected from 10 study sites as examples.*

Two sites (Chrauchtal and Val Piora) have been selected as examples to show detailed results of the models and how the selection of explanatory variables can differ between sites (Figure 4.7). The boxplots of the estimated coefficients for all 10 sites can be found in the supplemental material (Figures S1 - S10). Chrauchtal is located on the northern side of the Alps, while Val Piora is located on the south side. They have opposing orientations of the main valley axis (N-S and E-W, see Table 4.1). Chrauchtal is the site with the highest shallow landslide density (2.31 % with 8073 SLS points), which affects the very high inclusion rates for all explanatory variables (Figure 4.6). This also affects the spread of the boxplots, which show small variability of the coefficient values (Figure 4.7 in purple). With the high number of shallow landslides the variability of coefficients decreases, which means that the Lasso regression estimates very similar coefficient values for all 100 repetitions. Val Piora has a lower landslide density (0.49 % with 1116 SLS points). Here, the spread of the boxplots shows a higher variability for the estimated coefficients (Figure 4.7 in orange). Interquartile ranges are often much wider, and longer whiskers and outliers are more common than for the Chrauchtal site. For both sites, slope and aspect are very important variables in terms of coefficient size and inclusion rate. Aspect sectors S-SW are susceptible to shallow landslides while N-NW facing slopes are unfavourable. Roughness is negatively correlated for both sites, meaning that rougher terrain is less favourable to shallow landslides. Variables with smaller coefficients may also be selected often by the Lasso regression. However, these variables tend to have different effects depending on local conditions (e.g. Distance to Roads/Road Density, Elevation or TWI).

To assess the prediction skills of the individual site models, we calculate the ROC curves and the corresponding AUC values (Section 4.3.3). Curves closer to the top left corner of the plot show models with higher predictive skills (e.g., Urseren, AUC=0.865), while curves closer to the diagonal line have lower predictive skill (e.g., Baulmes, AUC=0.733). Confusion matrix scores summarised in Table 4.3 are based on a probability threshold of 0.5, which is the best threshold based on ROC curve evaluation (not shown). Brier scores describe the accuracy of the predictions, where values closer to zero indicate better model performance (Section 4.3.3). The Urseren site has the best model accuracy (BS = 0.14), while Baulmes has the lowest score (BS = 0.21, located in the Jura mountains with only 26 SLS points). The remaining eight models have BS values that range between 0.16 and 0.19, which is satisfactory. Models of sites with more SLS points perform better and have a smaller spread of the bootstrapped

BS. Sites with fewer SLS points do not perform as well. One exception is the Chrauchtal site (BS = 0.18), which has 8074 SLS points, yet doesn't perform as well as other sites with fewer points. For models with higher Brier scores the selected explanatory variables might not have been suitable enough to predict the location of shallow landslides. Whereas for sites such as Urseren and Val Piora, the available explanatory variables are well suited to describe the mapped shallow landslides.

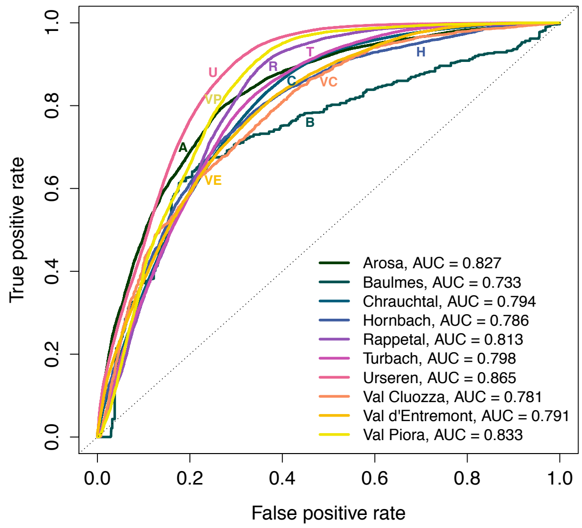

Figure 4.8: *ROC performance measure of the models for all 10 sites. Plot displays ROC curves with corresponding AUC values.*

Table 4.3: *Confusion matrix derivations using 0.5 for the prediction threshold. Perfect scores are Accuracy = 1, Bias = 1 (above 1 is over-predicted, while below 1 is under-predicted), True Positive Rate (TPR = 1 and False Positive Rate (FPR) = 0. Site names are abbreviated.*

Site	A.	B.	C.	H.	R.	T.	U.	V. C.	V. E.	V. P.
Accuracy	0.760	0.716	0.727	0.723	0.758	0.741	0.798	0.702	0.717	0.770
Bias	1.023	0.851	1.071	1.066	1.123	1.098	1.081	0.989	1.029	1.083
TPR	0.772	0.641	0.763	0.756	0.819	0.790	0.838	0.697	0.731	0.812
FPR	0.251	0.209	0.308	0.310	0.303	0.308	0.243	0.293	0.298	0.271

Generally, the number of shallow landslides available at a site does not necessarily affect the mean estimated value of coefficients, but the variability of the estimates is smaller, and the inclusion rates are higher for sites with more data points. Low performing models are either for sites located outside of the Alpine region (Baulmes, Hornbach) or in the National Park (Val Cluozza, only 8% grassland in the valley) and have the lowest number of shallow landslides. This may be because different processes govern shallow landslides that are not covered by available variables. Alpine sites perform better, although performance measures can vary here too. Sites with better Lasso regression model performance may be better explained with the available explanatory variables than other sites. Additionally, the better performing models are for sites with an east-west orientation of the valley, independent of the number of shallow landslides. Because the latter implies that more slope surfaces are facing either south or north. South-facing slopes tend to be more susceptible to shallow landslides in the Alps as the exposition determines the amount of solar radiation (solar angle and duration). This, in turn, affects parameters such as evapotranspiration or soil moisture, but also affects snow characteristics such as snow cover, snow movement or snow melt, which have a strong influence on

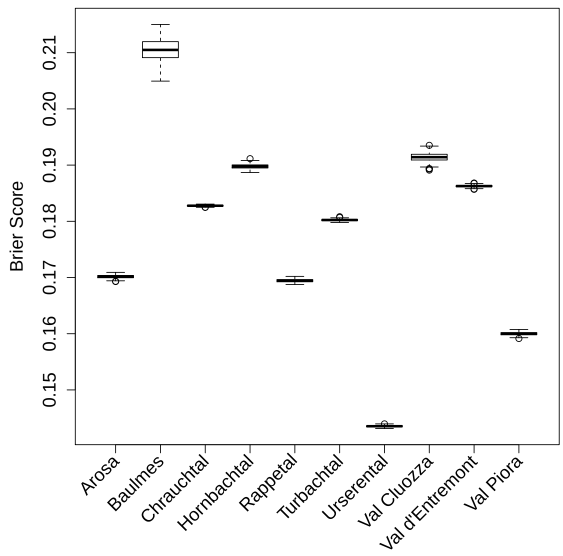

Figure 4.9: *Performance measure expressed with the Brier score for the models for all 10 sites. Plot shows boxplots of Brier scores where lower Brier scores are indicative of better model performance.*

the occurrence of shallow landslide (Schauer, 1975; Moser and Hohensinn, 1983; Tasser et al., 2003; Meusburger et al., 2010b; Wiegand and Geitner, 2013; Höller, 2014; Leitinger et al., 2018).

4.5.2 Performance of Slope-only model

As the slope is always the most important predictor for shallow landslides in terms of coefficient size and model inclusion rates, a Slope-only model was tested for all sites. The application of the Slope-only model indicates how well slope predicts shallow landslides and how important additional explanatory variables can be. We, therefore, compare the results of Slope-only models for all sites to the full-variable models based on their Brier scores (Table 4.4). Additionally, a no-Slope model containing all predictors except for slope was included in the evaluation, demonstrating the additional importance of slope (full model) in comparison to all other predictors. Interestingly, for Baulmes with only 26 SLS points, the Slope-only model performs slightly better than the full model. Arosa has only a slightly higher BS result for the full model compared to the Slope-only model, which indicates that additional explanatory variables do not improve the model for Arosa very much. The importance of slope for Arosa can already be seen in Figures 4.5 and 4.6. For all remaining sites, additional explanatory variables included in the model increase the model performance substantially. This is further supported by the higher BS results of the no-Slope models. The differences between the Slope-only, no-Slope and the full models are statistically significant for all sites (paired t-test with p-values ≤ 0.05).

4.5.3 Performance of All-in-one Model

With the all-in-one model, we evaluate whether the same explanatory variables are important for cross-regional evaluations as for individual site evaluations. As all sites included in the all-in-one model have different numbers of SLS points, the sites with more points have a stronger influence on the model's outcome.

Table 4.4: *Brier scores for the Slope-only model compared with Brier scores of the no-Slope and full models for all sites. The values displayed are median values of the bootstrapped Brier scores (500 repetitions). Lower scores are better (bold font) than higher scores.*

Site	Slope-only	no-Slope	Full Model
Arosa	0.17031	0.17589	**0.17017**
Baulmes	**0.19803**	0.20926	0.21049
Chrauchtal	0.20170	0.19294	**0.18277**
Hornbach	0.20348	0.19085	**0.18979**
Rappetal	0.22223	0.17324	**0.16944**
Turbach	0.20377	0.18349	**0.18023**
Urseren	0.18088	0.14894	**0.14354**
Val Cluozza	0.22741	0.19268	**0.19141**
Val d'Entremont	0.21468	0.18634	**0.18627**
Val Piora	0.19847	0.16873	**0.16000**

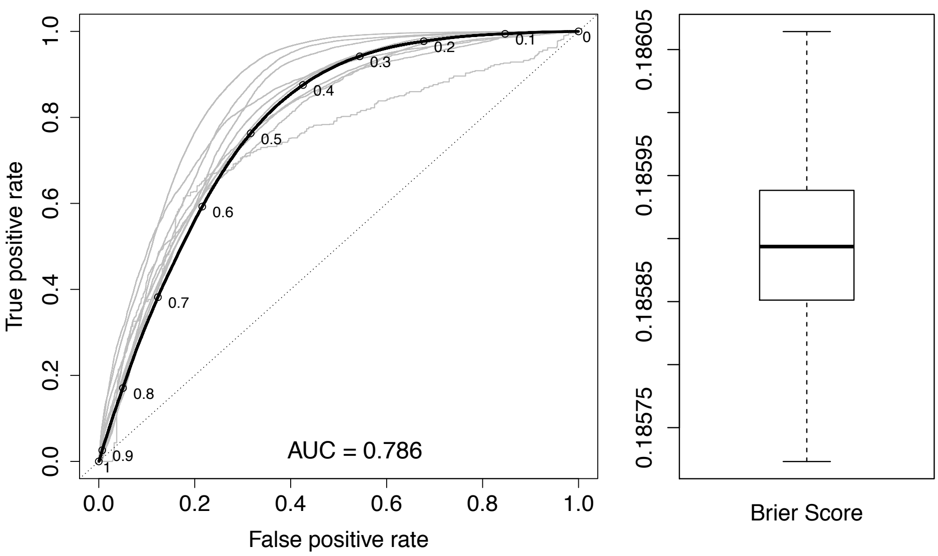

Figure 4.10: *On the LHS, the ROC Curve is displayed with the AUC value for the all-in-one model in black (including locations of probability thresholds) superimposed over the individual site models in grey. On the RHS is the bootstrapped Brier score for the all-in-one model.*

The all-in-one model places the ROC curve at roughly the centre of the individual site models (Figure 4.10), which is confirmed by the AUC value of 0.786. The same can be stated for the BS result (BS=0.186). With a Bias of 1.079, the all-in-one model only slightly over-forecasts shallow landslide points, while the overall accuracy of 72.3 % is slightly below the average for the individual site models (74.1 %). The True Positive Rate lies at 76.3 % and the False Positive Rate at 31.6 %, which is slightly higher than all individual site models. Generally, the individual-site models perform better in most cases, as local conditions are important for the overall accuracy of models. However, the variability of the estimated coefficients of the all-in-one model is relatively low (Figure 4.11) indicating, that the coefficients were estimated similarly when selected. The most important variables are comparable to the individual site models, with slope and roughness having the largest coefficients for continuous variables (Goetz et al., 2015). The categorical variables aspect and geology show similar behaviour to the individual site models. The CHELSA climatology variables (Max. Precipitation Events, Snow Days/Snow Cover Days, Growing Season Length and Frost Change Frequency) were originally included with the idea that these might have a stronger impact when doing cross-regional evaluations such as this all-in-one model. From these variables, frost change frequency was selected the most times (88 %). Frost change frequency describes the number of daily events for which the temperature encompasses zero (Karger and Zimmermann, 2019), yet the estimated coefficient is very small. This variable was tested as it may represent snow movement processes related to freezing/thawing cycles, yet, it was too ambiguous. Other climate variables were rarely selected. The inclusion of climate variables may prove helpful when comparing different regions in a "bulk" perspective (e.g. average landslide density per site), but seemingly not when explaining locations of individual shallow landslides across different regions. Additionally, the comparatively low spatial resolution of the CHELSA data set (30 arcsec) may not be suitable for such detailed analysis, and the variables might not represent triggering landslide processes well enough.

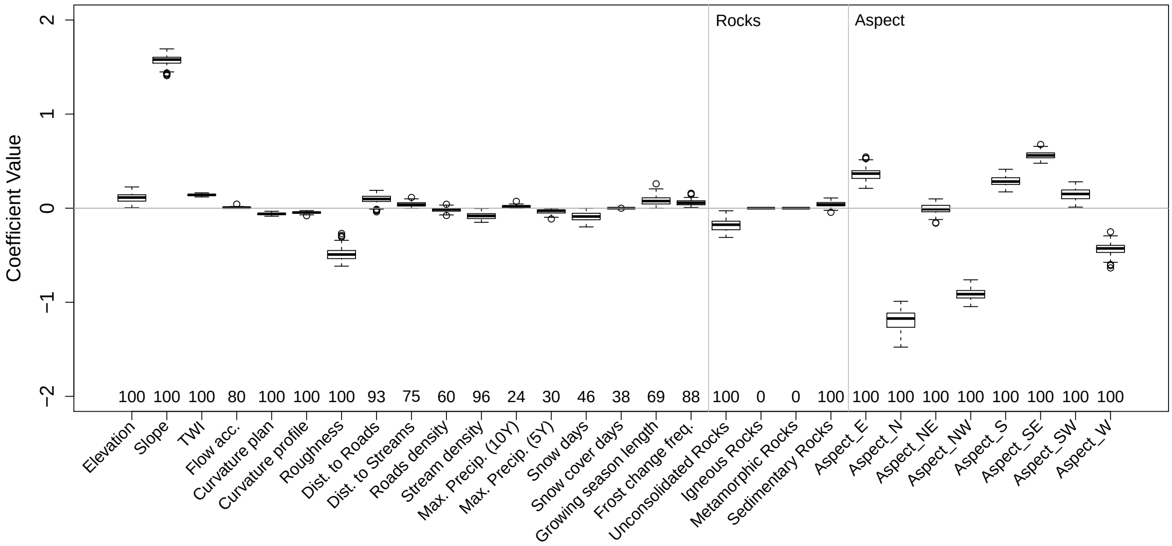

Figure 4.11: *Boxplots showing the coefficient range with 100 repetitions. Numbers above variable names indicate the number of times it was selected for the model.*

Additionally, shallow landslide causes can be manifold and singular triggering processes are difficult to assign and the timing of the occurrence is often unknown. If possible, it would be useful to differentiate between triggering factors of shallow landslides based on visual appearance, as was suggested by Geitner et al. (2021). With the U-Net approach used to map the shallow landslide sites on aerial images (0.25 m), it is impossible to distinguish between triggering factors (Samarin et al., 2020; Zweifel et al., 2019). With higher spatial resolutions of climate variables and a temporal component to the mapped shallow landslides, it may become possible to assign triggering processes with such evaluation techniques. Additional variables such as land-use information (e.g., grassland management) could be of great importance if available in appropriate spatial resolution and high enough accuracy for all regions (Meusburger and Alewell, 2009; Budimir et al., 2015). While the explanatory variables for this study were chosen based on data availability, this is not an exclusive list of possible predictors. Many studies have worked towards identifying triggering factors in varying Alpine regions, such as the effects of land-use, snow processes, precipitation events or vegetation cover (Newesely et al., 2000; Tasser et al., 2003; Rickli and Graf, 2009; Wiegand and Geitner, 2010b, 2013; Meusburger and Alewell, 2008; Meusburger et al., 2013; Von Ruette et al., 2013; Höller, 2014; Ceaglio et al., 2017; Fromm et al., 2018; Geitner et al., 2021). Therefore, it is difficult to fully quantify all ongoing processes simultaneously in such a complex system, as triggering factors are often interlaced (Zweifel et al., 2019). To ideally represent causal factors for statistical evaluations of shallow landslides, these important processes need to be represented with high spatial resolutions and a temporal component needs to be included (Meusburger and Alewell, 2009).

Susceptibility Map

The calculated coefficients of the logistic regression may be used for spatial predictions of shallow landslide occurrence yielding a susceptibility map of the region for the remaining grassland areas. These susceptibility maps are useful to identify areas that may likely be affected by shallow landslides in the future (Barbb, 1984). As an example we used the site Chrauchtal to apply both the coefficients of the local model as well as the cross-regional all-in-one model (Figure 4.12). As the coefficients are estimated 500 times per model, we use the mean coefficient values for the prediction process. The results are very similar, however, to highlight the differences between the local and cross-regional *all-in-one* model, a map showing the differences between the two maps is shown, where red regions show slightly higher probabilities of shallow landslides in the cross-regional *all-in-one* model and blue areas show slightly higher probabilities in the local model. The blue areas mainly cover areas at higher elevations, whereas the red areas are located at lower elevations but are facing south. Working with cross-regional models allows for catching the general pattern, however, local hot-spots might be missed.

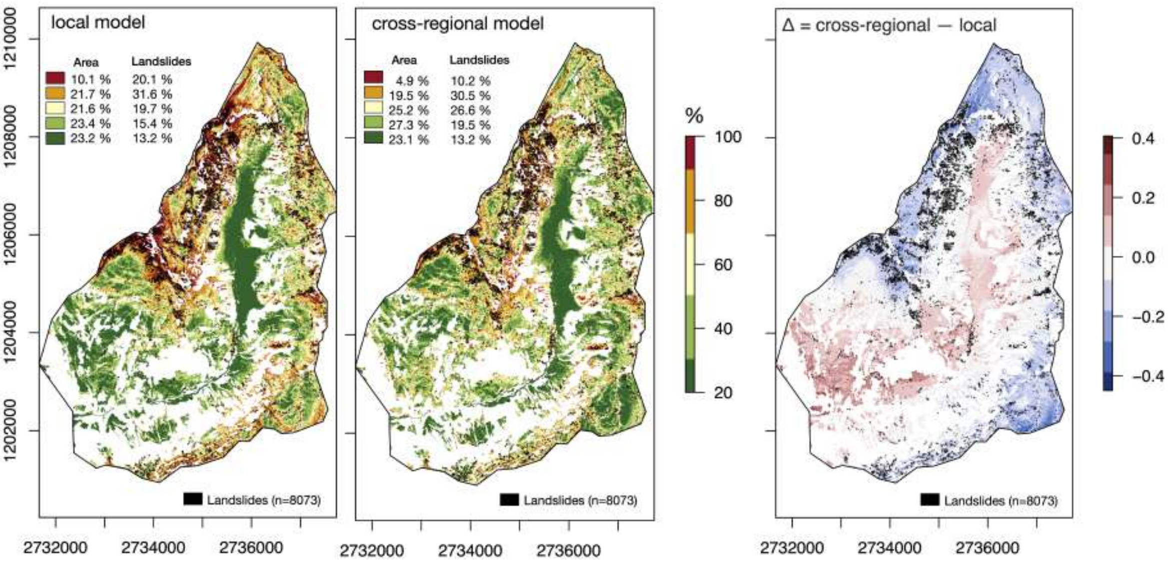

Figure 4.12: *Susceptibility maps for the study site Chrauchtal based on the local model and the cross-regional all-in-one model. The susceptibility maps show the probability of shallow landslides occurring at a specific pixel on the map. The difference between the two applied models are shown on the RHS. White areas on the map are not grassland and therefore not considered.*

4.6 Conclusions

In this study we located shallow landslides across 10 study sites spread across Switzerland. We use the term shallow landslides to describe the erosion sites which classifies the erosion feature without implication to the triggering event. Using the Lasso regression model, we identified the most important explanatory variables for these shallow landslides located on grassland slopes. Due to the different local conditions of the varying sites, different explanatory variables were identified as important. Slope and aspect are among the most important variables. Shallow landslides of sites with an east-west orientation of the valley axis as well as alpine sites were better explained by the available explanatory variables (Urseren, Val Piora, Rappetal and Arosa). This concludes that exposition-related processes in mountainous regions are essential for understanding regional patterns (e.g., snowmelt, snow movement). For the remaining sites, the available selection of explanatory variables was not as well suited and, therefore, important processes could be missed. Sites outside of the main Alpine region (Baulmes and Hornbach) or located in the National Park (Val Cluozza) have a small number of SLS points, which were not well explained by the available variables. Performance scores for individual site models range between BS = 0.144, AUC = 0.865 (Urseren) and BS = 0.210, AUC = 0.733 (Baulmes). Although we find that slope was the most important variable, predictions using only slope yield lower accuracies, indicting that additional variables are important to explain local shallow landslide occurrence. An all-in-one model evaluating all 10 sites simultaneously found comparable results to the individual-site models (i.e. slope and aspect) with performance values of BS = 0.186 and AUC = 0.786. Additionally, this model showed a relatively strong negative correlation for roughness, indicating that smooth grassland surfaces are more susceptible to shallow landslides. The decisive causal factors identified are generally related to static variables (e.g., geomorphological, geological), while the available climate-related data sets have proven to be less informative on both local and cross-regional scales. Nevertheless, data sets representing triggering shallow landslide conditions and processes in appropriate spatial resolutions would likely improve model performance. Studies focusing on understanding small scale processes are therefore of great importance, and with data availability shifting towards open access and higher spatial resolutions as well as large spatial coverage, such statistical evaluations may improve in the future.

Acknowledgements

This study was funded by the Swiss National Science Foundation (Project No. 167333) as part of the National Research Program NRP75 – Big Data. Calculations were performed at sciCORE (http://scicore.unibas.ch/) scientific computing core facility at University of Basel.

Snow covered mountain slopes
Photo: Robert Topulos

5

Snow Gliding as a Cause for Soil Erosion

5.1 Introduction

Snow gliding is defined as the downward motion of a snow cover layer over the ground surface (Blechschmidt, 1990; Höller, 2014; in der Gand, 1968). The effects of snow gliding consist of uprooting of vegetation and soil erosion by abrasion (Leitinger et al., 2008; Freppaz et al., 2010; Ceaglio et al., 2012; Meusburger et al., 2013; Höller, 2014). Snow gliding is therefore a major contributor to soil erosion during winter months. Ancey and Bain (2015) have identified the following conditions favourable to snow gliding in their review article, which can be roughly summarised as: steep slope angles (generally above 28°, although less is possible), smooth ground surface (low roughness) free of obstacles (mainly grassy slopes, bare rocks) , liquid water must be present at the interface between the surface and snow layer (temperatures $\geq 0°$ C). The latter can be caused by rain water percolating the snow pack, soil temperatures above freezing during snow fall, or by snow melt (in der Gand, 1968; Höller, 2014). Additionally, snow gliding often occurs on SE-SW facing slopes (Leitinger et al., 2008; Newesely et al., 2000). With the aid of a Spatial Snow Glide Model (SSGM) (Leitinger et al., 2008, 2018; Meusburger et al., 2014) we aim at identifying connections between regions with higher expected snow glide rates and higher erosion density. We calculate the expected snow glide distances using the SSGM for the entire Switzerland. We subsequently compare the snow glide distances to the location of shallow landslides, which were mapped on aerial images using a U-Net deep learning approach (Samarin et al., 2020) for 10 sites within Switzerland (Zweifel et al., 2021).

5.2 Spatial Snow Glide Model (*SSGM*)

To identify areas susceptible to snow gliding, Leitinger et al. (2008) developed a Spatial Snow Glide Model which was later revised by Meusburger et al. (2014) and Leitinger et al. (2018). This model used information based on forest stand, vegetation roughness, slope angle and aspect as well as winter precipitation amounts and yields the modelled snow glide distances (Leitinger et al., 2018). The modelled snow glide distances $\hat{y}$ (mm) are calculated as described in equation 5.1.

$$\begin{aligned}\hat{y} = \exp(&-1.07 - 0.967 \cdot x_1 + 0.091 \cdot x_2 + 0.01 \cdot x_3 + 0.971 \cdot x_4 + \\ &0.705 \cdot x_5 + 0.124 \cdot x_6 + 4.004 \cdot x_7 - 3.645 \cdot x_7^2) \cdot \alpha,\end{aligned} \tag{5.1}$$

Preliminary results of study under development.

where x_1 is the forest occurrence (0,1), x_2 is the slope angle (degrees °), x_3 is the winter precipitation sum between December and March (in mm), x_4, x_5 and x_6 are the slope aspects east, south and west, respectively (0,1), x_7 is the vegetation roughness, and α is the model error (α=1.29).

5.3 SSGM for Switzerland

The SSGM, which was developed for the Austrian Alps, has already successfully applied to the Urseren Valley in the Swiss Alps by Meusburger et al. (2014). Here, we thus assume a general transferability of the model to Swiss Alpine terrain.

5.3.1 Data Sets used for SSGM calculations

The data sets used to calculate the SSGM for Switzerland are summarised in Table 5.1.

Table 5.1: *Summary of data sets used as input for the SSGM for Switzerland.*

Model Component	Data source	Resolution	Year
x_1 Forest Stand	CORINE Land-cover	100 m	2012
x_2 Slope Angle	SwissALTI3D	4 m	2014
x_3 Winter Precipitation	CHELSA	1 km	1982–2013
x_4 Slope Aspect: East	SwissALTI3D	4 m	2014
x_5 Slope Aspect: South	SwissALTI3D	4 m	2014
x_6 Slope Aspect: West	SwissALTI3D	4 m	2014
x_7 Vegetation Roughness	CORINE Land-cover	100 m	2012

The specific vegetation roughness values are taken from Leitinger et al. (2018) for the individual land-cover classes based on the CORINE land-cover information (Copernicus, 2012). These values were estimated based on field measurements (Meusburger and Alewell, 2009; Leitinger et al., 2018). For the winter precipitation values we used a 30-year climatology mean for the years 1982/83-2012/13 based on precipitation raster maps of the CHELSA data set (Karger et al., 2017, 2018). The digital terrain model information was reduced from a 2 m grid to a 4 m grid to reduce computational effort. Based on the smallest spatial resolution of the data input to the SSGM, the final result has a spatial resolution of 4 m.

5.3.2 SSGM Map

Figure 5.1 shows the result of the SSGM for Switzerland using the data sets described in Section 5.3.1. Areas outside of the mountainous regions are not steep enough to encounter snow gliding (below 15°) and are therefore not considered (Leitinger et al., 2018). The modelled snow glide distances are grouped into four classes from low to high glide distances to match the visualisation of Leitinger et al. (2018) and Meusburger and Alewell (2009).

The regions with high modelled snow glide distances are mainly located in the northern part of the Alps. Notably, high alpine regions in the east (Canton Grisions) and south-west (Canton Valais) show lower snow glide distances, despite the steep terrain.

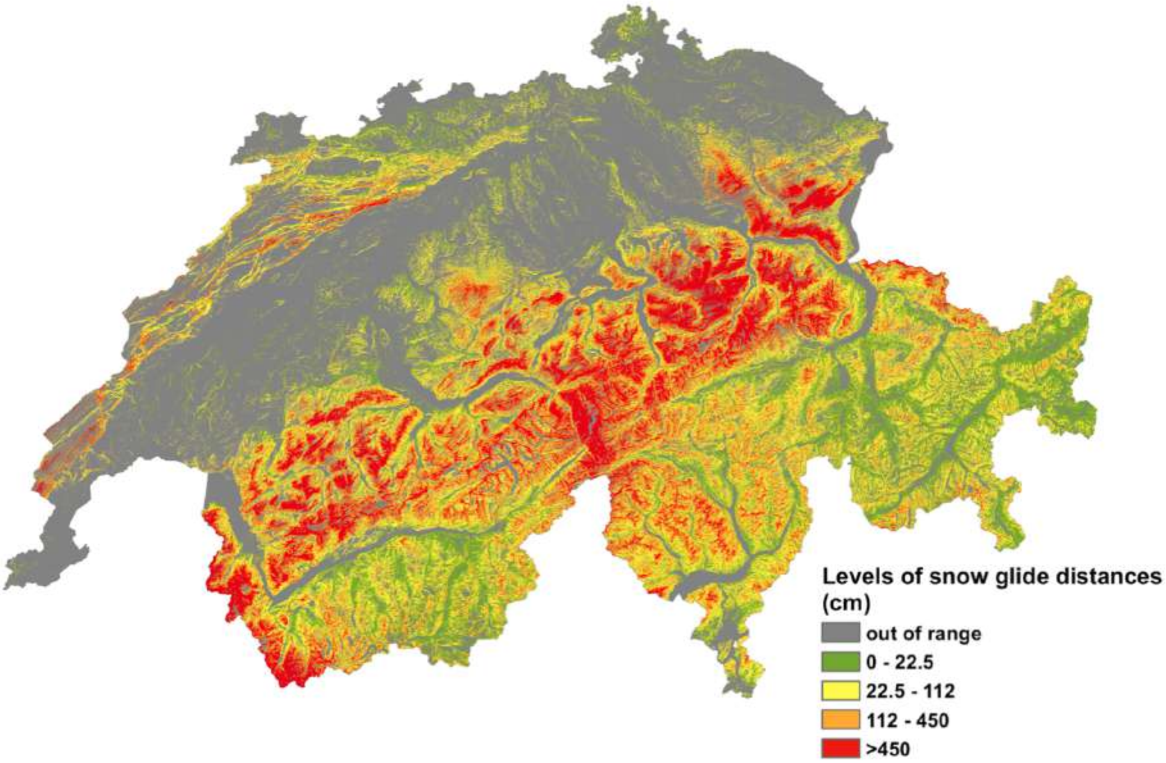

Figure 5.1: *Spatial Snow Glide Model for Switzerland with a spatial resolution of 4 m. Gray areas are located out of range (slopes below 15°). Colours indicate different snow glide distance (in cm) classes from green (low expected glide distance, below 22.5 cm) to red (high expected snow glide distance, above 450 cm).*

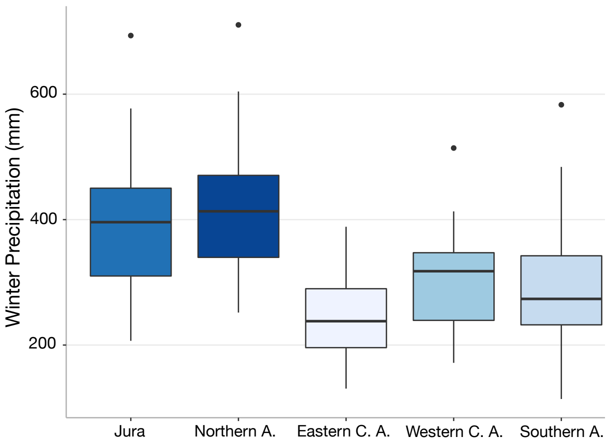

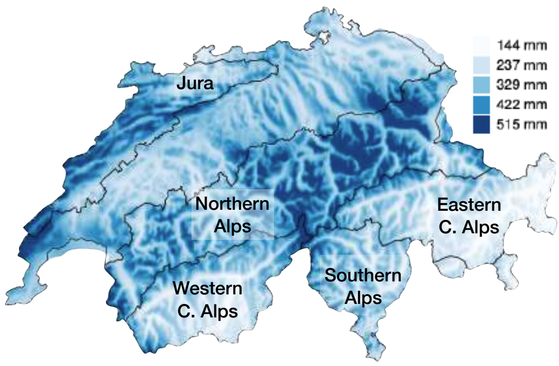

Figure 5.2: *30-year winter precipitation mean (December-March) from 1982/83 to 2012/13 divided into climate regions. LHS shows boxplots of the average precipitation amount within the region and on the RHS the precipitation pattern of Switzerland with regional boarders is visualised. Darker shades of blue indicate high precipitation amounts.*

When comparing the winter precipitation map of Switzerland to the SSGM map, it becomes clear, that the major pattern of the SSGM map is mainly controlled by this parameter (Figure 5.2). Regional evaluations of average winter precipitation indicate, that the Northern Alps receive much more precipitation than other regions in the Alps. This is due to the most frequent weather system flowing from western to north-eastern directions (68 % of the time) (MeteoSwiss, 2021). In these cases the

Alps can act as a climate barrier and lead to orographic precipitation on the northern side (MeteoSwiss, 2021).

5.4 Shallow Landslide Density

We analyse mapped shallow landslides for 10 sites located in different mountain regions of Switzerland (Jura, foothills and Alpine regions) which are located in different climate regions (Figure 5.3) (Zweifel et al., 2021).

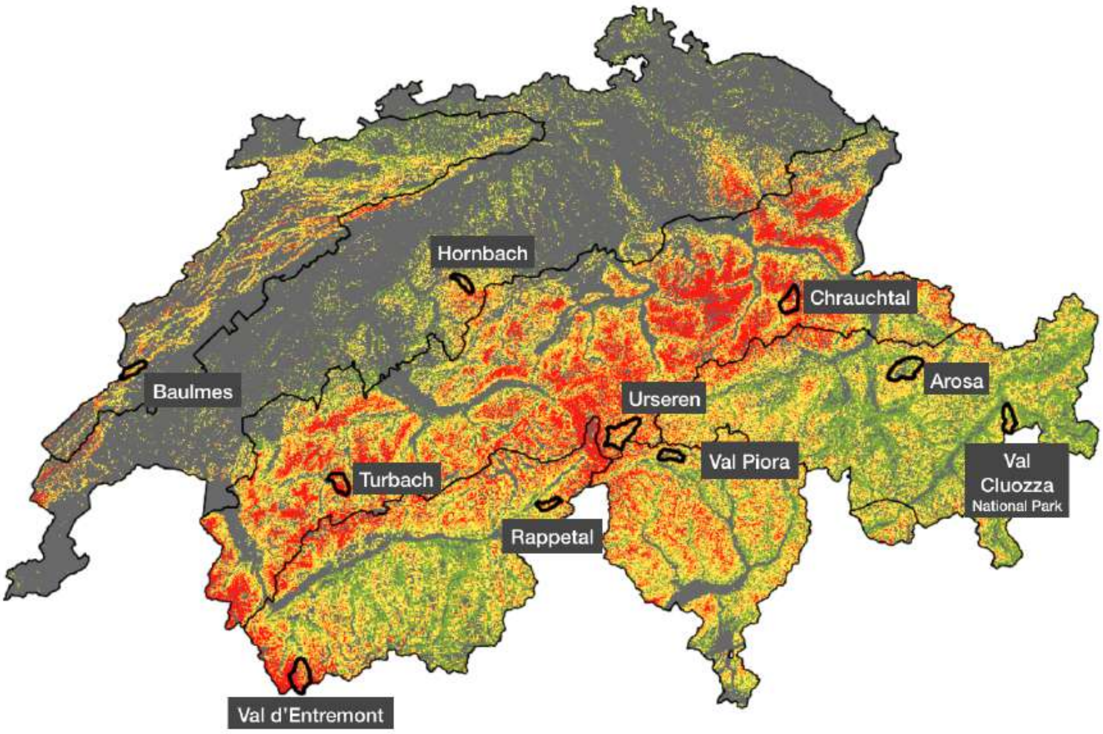

Figure 5.3: *Location of sites used for soil erosion evaluation. For more details on study site information refer to Zweifel et al. (2021) Section 4.2.*

For the shallow landslide mapping we use aerial images at the end of the 30-year winter precipitation period, which corresponds to the years 2013, 2014 and 2015, depending on the location (see Section 4.2 of Zweifel et al. (2021) for more details). The sites are all located above the average winter snowline height of 800 m (Hantel et al., 2012). By choosing locations in different regions across Switzerland we cover sites with higher amounts of winter precipitation and higher expected snow glide distances and vice versa. These shallow landslide sites were mapped using a U-Net deep learning approach (Ronneberger et al., 2015; Samarin et al., 2020) which was applied to aerial images (0.25 m spatial resolution) with the help of digital terrain model information (2 m spatial resolution). This U-Net model is trained to identify different soil erosion processes on grasslands (Samarin et al., 2020). In this study, the term *shallow landslide* refers to the visual appearance of these erosion sites on aerial images and describes the bare soil patches where the vegetation layer has been removed (Zweifel et al., 2021). Different triggering factors can be related to these erosion sites, such as strong precipitation events, abrasion by snow or often a combination of both (Wiegand and Geitner, 2010b; Geitner et al., 2021).

To calculate the shallow landslide density, the proportion of eroded area to total grassland area was calculated. We test, whether sites with lower shallow landslide densities correlate with lower modelled

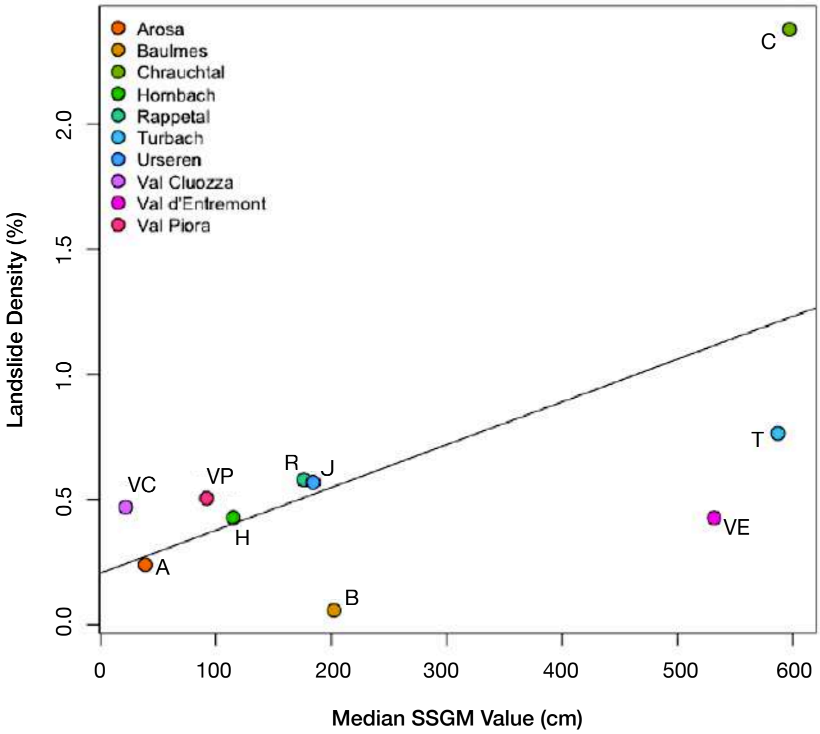

Figure 5.4: *Average shallow landslide density versus the median values of modelled snow glide distances for 10 sites across Switzerland.*

snow glide distances and vice versa (Figure 5.4). For most sites with lower shallow landslide densities, the modelled snow glide distance is also low. While the site Chrauchtal shows a connection between high shallow landslide densities and high snow glide distances, the sites Turbach and Val d'Entremont do not reflect this connection, as snow glide distances are high, yet landslide densities are comparatively low.

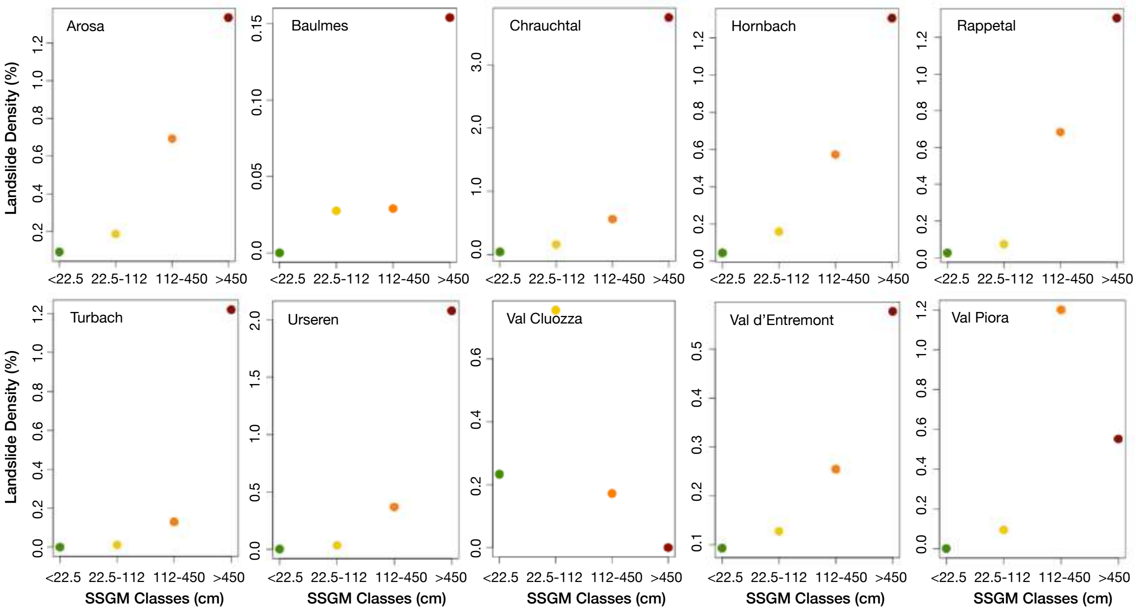

Figure 5.5: *Shallow landslide density per study site in relation to the modelled snow glide distances sectioned in to SSGM classes.*

A detailed evaluation of sites with landslide density displayed against modelled snow glide distances binned into classes (low to high modelled snow glide distance) is shown in Figure 5.5). Most sites show an increase in expected snow glide distances with increasing shallow landslide density. Exceptions are found for Val Cluozza, which is located within the National Park with only very little grassland surfaces (mainly shrub cover and rocks). Val Piora, which is located in the Southern Alps (Canton Ticino), shows an unusual behaviour with higher shallow landslide density in the second highest class.

5.5 Discussion & Outlook

The results presented in this chapter are from a preliminary study still in development. The SSGM was developed as a tool to model snow glide distances and to determine corresponding risks, such as soil erosion, damage to vegetation or glide avalanches (Leitinger et al., 2008). We assess the relationship of modelled snow glide distances to mapped shallow landslides for 10 sites across Switzerland. The results of the shallow landslide density evaluation shows, that for most sites a correlation can be seen between high glide distances and high shallow landslide densities. This can also be found vice versa with lower values. However, this does not fully prove, that snow gliding is the cause of soil erosion at these locations. Snow gliding tends to occur in steep terrain, however other triggering processes can also lead to erosion in steep terrain (gravitational mass movements) (Wiegand and Geitner, 2010b; Geitner et al., 2021). Additionally, using a 30-year average winter precipitation for the model input may indicate which regions are susceptible to snow gliding, yet this may not reflect the observed damage of mapped soil erosion sites. While Leitinger et al. (2018) also used a climatology mean for their SSGM (1980-2010), they stated, that the variation in precipitation pattern should be accounted for in some way. Additionally, frequent snow gliding events often occur during so-called *glide winters* caused by particular meteorological conditions (Ancey and Bain, 2015; Höller, 2014; Geitner et al., 2021). Such glide winters may be the cause of soil erosion by snow abrasion. Adding a temporal aspect to this study may provide crucial insights. This may be achieved by performing erosion mapping for all aerial images during a given time period and analysing changes with the help of tailored snow glide models (adapted winter precipitation input). Another approach may be to specifically analyse aerial images before and after snow glide winters, which have been summarised by Höller (2014). The SwissImage product used for this study is updated every 3-years for a specific location (Swisstopo, 2010). Therefore, it is not possible to conduct such an analysis from one year to the next using this product. Alternatives, such as UAV images, may provide solutions for selected sites. In future, if spatial resolutions of aerial images increase, it may also be possible to distinguish between shallow erosion caused by abrasion or by landsliding and assign categories accordingly. This differentiation would increase the accuracy of studies identifying causal factors of mapped erosion sites (Zweifel et al., 2021).

However, the SSGM for Switzerland is an interesting product to identify areas susceptible to snow gliding, although the quality of the results may be limited to regions with similar conditions to the original study area of the Tyrolean Alps and may be increased when incorporating more details on winter precipitation values (Leitinger et al., 2018).

Mountain grassland landscape
Photo: Henry Gillis

6 Conclusions

Within the framework of this thesis we were able to develop a soil erosion monitoring tool, which is able to successfully map different soil erosion processes on high-resolution aerial images on large scales (catchment scale, potential for alpine scale). The conclusions regarding the monitoring tool are summarised in Section 6.1. By mapping the locations and extent of soil erosion sites, the analysis of spatial and temporal developments of these sites becomes possible. The main conclusions for the soil erosion assessment are summarised in Section 6.2.

6.1 Monitoring of Soil Erosion

With the soil erosion monitoring tool developed in the framework of this thesis we aimed to map soil erosion sites on grasslands visible on aerial images and to assign erosion classes to the mapped sites. This tool allows for a holistic approach to better understand ongoing soil erosion processes in Alpine terrain over space and time. While we are not able to quantify the amount of lost soil (e.g., t/ha y), we are able to map the extent of eroded sites (e.g., ha) and by introducing a temporal component we can assess and quantify relative changes over time. During the work on this thesis two approaches were developed to map soil erosion features on aerial images. It is important to note that the second more advanced approach (Deep Learning, Chapter 3) builds on the findings and results of the first approach (Object-Based Image Analysis, Chapter 2).

Object-Based Image Analysis (OBIA) has been the state-of-the-art technique for many years for segmenting and classifying remotely sensed images. By applying OBIA, objects are created from similar pixels which can subsequently be classified with the help of machine learning classifiers and/or rule-set classifiers. We applied OBIA for the Urseren Valley (Canton Uri) to map soil erosion on five aerial images over a 16-year period (2000-2016) (Chapter 2). We were able to identify four different erosion classes in the Urseren Valley and assign their prevailing erosion process (shallow landslides, sheet erosion) or main triggering factor (livestock trails, management effects). This approach allows for better understanding of all visible erosion processes on grasslands in both a spatial and temporal context. The approach is suitable for smaller scale studies and generally has a high accuracy. It is, however, very labour intensive and requires manual work-steps and adjustments. These drawbacks make the method unsuitable for large-scale soil erosion assessment studies.

With the aim of overcoming these methodological shortcomings, we developed a deep learning approach. The deep learning approach uses a fully convolutional neural network with the *U-Net* architecture (Chapter 3). We train the U-Net model to perform semantic segmentation on the aerial images, labelling each pixel with a class probability. The high-quality results obtained from the first study using OBIA (Chapter 2) served as the basis to train the U-Net model (9 km^2 training area of the Urseren Valley). Therefore, the U-Net was trained to assign the following classes to pixels: shallow landslides, livestock trails, sheet erosion, management effects, and non-assignable (no erosion site). By applying an appropriate probability threshold, segmentation of erosion sites is performed.

Table 6.1: *Table highlighting the main differences and similarities of the two approaches for soil erosion monitoring.*

	Object-based Image Analysis	**Deep Learning**
spatial scale	catchment scale	catchment scale, large scale
accuracy	high	high
control, flexibility	flexibility during work-flow	flexibility with probability threshold selection
transferability	work-flow adjustments needed	high level of robustness and reliability
objectivity	higher level of subjectivity due to manual adjustments	higher level of objectivity due to automatic application
production time	labour intensive	fast computation
automation	semi-automatic	fully automatic (after training)
software	mainly commercial software	open access software
additional requirements	expert knowledge (erosion processes) during application	super-computing/GPU for large scale studies

We showed in Chapter 3, that the U-Net model is capable of reproducing the mapping results obtained with OBIA in terms of erosion classes and boundaries of erosion sites. Also, the same temporal trends which were obtained with OBIA (between different years) are reproduced with the U-Net, showing the robustness of this method. For the accuracy assessment OBIA mapping was used as ground-truth data for a held-out test region (17 km^2), where both spatial and temporal transferability of the U-Net was tested. The accuracy assessment showed, that the U-Net performs on par with OBIA, however, visual assessments made clear, that the U-Net can even outperforms OBIA in many cases. The main improvements provided by the deep learning approach are the high level of automation, low computational time with a high level of accuracy (Table 6.1). However, a major limiting aspect of this method is the requirement of high quality training data, which is difficult to attain for natural objects but was available thanks to the OBIA study presented in Chapter 2.

Another advantageous property is the possibility to transfer the U-Net mapping tool to other sites located in different regions. The U-Net was applied to 10 study sites (size between 16 and 54 km^2) for the studies presented in Chapter 4 and 5. With this, unprecedented spatial scales were reached. While all erosion classes can be mapped, only shallow landslides were further analysed. As no ground truth data is available, great care was taken to visually asses the mapped shallow landslides of all study sites. For many sites the transfer of the erosion monitoring tool was highly successful. For some sites with previously unknown conditions (not covered by training data), such as those located in foothill regions of the Alps or the Jura mountains, more manual corrections were necessary than for sites with similar conditions to the Urseren Valley (Alpine site). Reasons may include different topography (hilly characteristics as opposed to mountain slopes with predominant orientation and steep slopes) or different appearances of erosion sites, such as patchy erosion sites containing a combination of bare soil and vegetation, making the definition of boundaries difficult.

Generally, both OBIA and the U-Net deliver conservative estimates in terms of the mapped affected area. A quantification of the mapping accuracy needs to be completed in future work for all erosion classes (see Outlook in Section 6.3).

6.2 Assessment of Soil Erosion Processes

By mapping soil erosion sites on high-resolution aerial images, we can conduct evaluations on different spatial scales (plot-level to large-scale) as well as temporal developments of the affected sites in a holistic manner. Chapter 2 focuses on the Urseren valley for which a method was developed to identify all visible soil erosion sites and assign one of the four major erosion classes (shallow landslides, livestock trails, sheet erosion, management effects). Mapping was conducted for five different aerial images across a 16 year period (2000-2016). This resulted in a high-quality data set with the location and extent of erosion sites for which further information, such as topographic conditions, was assigned.

The results presented in Chapter 2 show, that soil degradation has increased in the Urseren Valley over the study period for all mapped erosion classes. Differences were found for regions at higher elevations as opposed to lower elevations. Slopes at lower elevations, which are located closer to the valley bottom and therefore closer to farms, are more strongly affected by erosion caused by land-use management. These include an increase in observed livestock trails, sheet erosion and sites with management effects (e.g., haying). Higher elevations, which are more remote and therefore seldom or never used for grazing, show increases in shallow landslides and sheet erosion. Possible reasons for these increases can be related to changing climate conditions, such as an increase in extreme events (e.g., precipitation as snow or rain, prolonged droughts) or changing snow dynamics (e.g., snow melt, snow gliding).

While Chapter 2 and Chapter 3 focus on the Urseren Valley and different erosion classes over time (spatio-temporal analysis), in Chapter 4 shallow landslides located across ten different sites in Switzerland at one point in time (aerial images taken between 2013 and 2015) are evaluated. By applying a logistic regression model, the most important explanatory variables were identified for the occurrence of shallow landslides for the individual sites as well as across all ten sites simultaneously. The analysis was conducted for shallow landslides located on grassland slopes. Local conditions of the ten sites varied in terms of topography, orientation, geological bedrock and climate, and therefore different explanatory variables were found to be important for different sites. Generally, slope and aspect were the most important explanatory variables. The logistic regression models performed better for sites with an east-west orientation and located in the Alps, indicating that the explanatory variables available to describe shallow landslide occurrence are especially well suited for these locations. These may include processes connected to the exposition and solar radiation, such as snow melt and snow gliding. The logistic regression for the all-in-one model identified a strong correlation to topographic roughness, indicating that smooth surfaces are generally more susceptible to shallow landslides. While additional variables describing climate related factors may be of great importance for such landslide evaluations, the data set included in this study (CHELSA climate data with 30 arcsec resolution, Karger et al. (2017, 2018)) was too coarse to successfully help explain the shallow landslide patterns.

As winter processes, such as snow gliding, have been linked to soil erosion in Alpine terrain many times in the past, we implemented a Spatial Snow Glide Model (SSGM) which is presented in Chapter 5. The SSGM was calculated for the entire area of Switzerland and indicates the expected (modelled) snow glide distances (in cm) per pixel. The modelled snow glide distances were analysed for the same ten sites presented in Chapter 4 as an additional potential cause for shallow landslides. For most sites a correlation between the modelled snow glide distance and the number of shallow landslides has been found. This is true for both higher snow glide distances and higher shallow landslide densities as well as for lower snow glide distances and lower shallow landslide densities. However, as snow gliding is expected to be higher in steep terrain, which is generally susceptible to shallow landslides (e.g. mass movement), as also demonstrated in Chapter 4, a definitive causality cannot be established without further evaluations. The findings of Chapter 5 indicate promising results for future studies on snow gliding as a cause for soil erosion, especially when considering a temporal component.

6.3 Outlook

Within the framework of this project we were able to develop an efficient soil erosion monitoring tool to capture the location, extent and type of soil erosion. While the U-Net tool was applied to ten different sites within Switzerland, the application possibilities are vast. The high efficiency will allow for nation wide soil erosion monitoring in space and time. This will facilitate the development of land-use mitigation strategies.

Good results are achieved for grassland sites with similar conditions to those of the training area (Urseren Valley, Alpine site). For areas with different conditions more training data may be required to further improve the transferability and reliability of the U-Net tool. New training data extending to geographic conditions and soil erosion processes unknown to the model can be produced manually or with methods such as OBIA.

Accuracy assessments are generally very difficult to conduct for tasks with no ground truth availability. While attempts have been made to quantify the accuracy of OBIA and U-Net, these methods are still limited. It was possible to assess shallow landslides in the Urseren Valley thanks to previous work yielding manually mapped landslides to which results could be compared. Future work should focus on attaining additional information to better assess the quality of the monitoring tools applied. This may be achieved with independent higher resolution data provided by UAV flights accompanying the official aerial images during the same recording season. Their high spatial resolution will allow for accuracy assessments of selected sites.

Additionally, the monitoring tool is configured to handle aerial images with RGB spectral information and spatial resolutions of 0.25 - 0.5 m. Future work may trial data sets with more spectral information (e.g., NIR channel) or higher spatial resolutions.

Future projects may also focus on evaluating causal factors for all soil erosion processes on larger scales, as for this thesis only shallow landslides were evaluated. Also, more detailed and higher resolved data sets which may be used as explanatory variables (e.g., snow data), should be considered when these become available.

Studies estimating soil erosion rates on the basis of erosion models are applied on varying scales for different regions of the world (from small scales up to global scale). However, the issue of validating such erosion models has yet to be solved. The mapped soil erosion sites provided by the monitoring tool developed in the framework of this thesis may be the ideal accompaniment to soil erosion modelling studies. The information gained may be used for model verification or may possibly be included as additional information for soil erosion models. As stated above in Section 6.1 the mapped erosion sites do not deliver a quantitative assessment of lost soil in terms of soil amount (e.g., t/ha y). The spatial extent of soil erosion sites provided by the mapping may, however, be combined with local soil erosion measurement studies to further improve interpolation techniques for scaling up soil loss quantities.

Foot path along hill-slope
Photo: Patrick Robert Doyle

A

Supplemental Material: Spatio-Temporal Pattern of Soil Degradation in a Swiss Alpine Grassland Catchment

Random Forest Classifier Results

The Random Forest classifier was used in eCognition to identify bare soil areas. Figure A.1 shows the relative importance of the variables to achieve the classification.

Rule Set: Soil Erosion Classes

The bare soil areas are categorised in to four different soil erosion classes based on the following rule set listed in Table A.1.

Table A.1: *List of object features and their corresponding thresholds used in the rule set to assign specific erosion categories to soil erosion objects.*

Erosion Category	Object Features and Thresholds
Shallow Landslides	Mean Slope $>= 25°$; Border Contrast of ExG $>= -0.18$ and $<= -0.04$; Border Index $>= 3$; Shape Index $<= 3$; Rel. Border to Class *'Vegetation'* $>= 0.5$
Livestock Trails	Length/Width $>= 4$; Density $>= 1.2$; Main Direction of objects perpendicular to the slope (range of $\pm 20°$)
Management Effects	Area $>= 20'000$ *px*; Mean Slope $<= 25°$
Sheet Erosion	Remaining *'Soil Erosion'* Objects

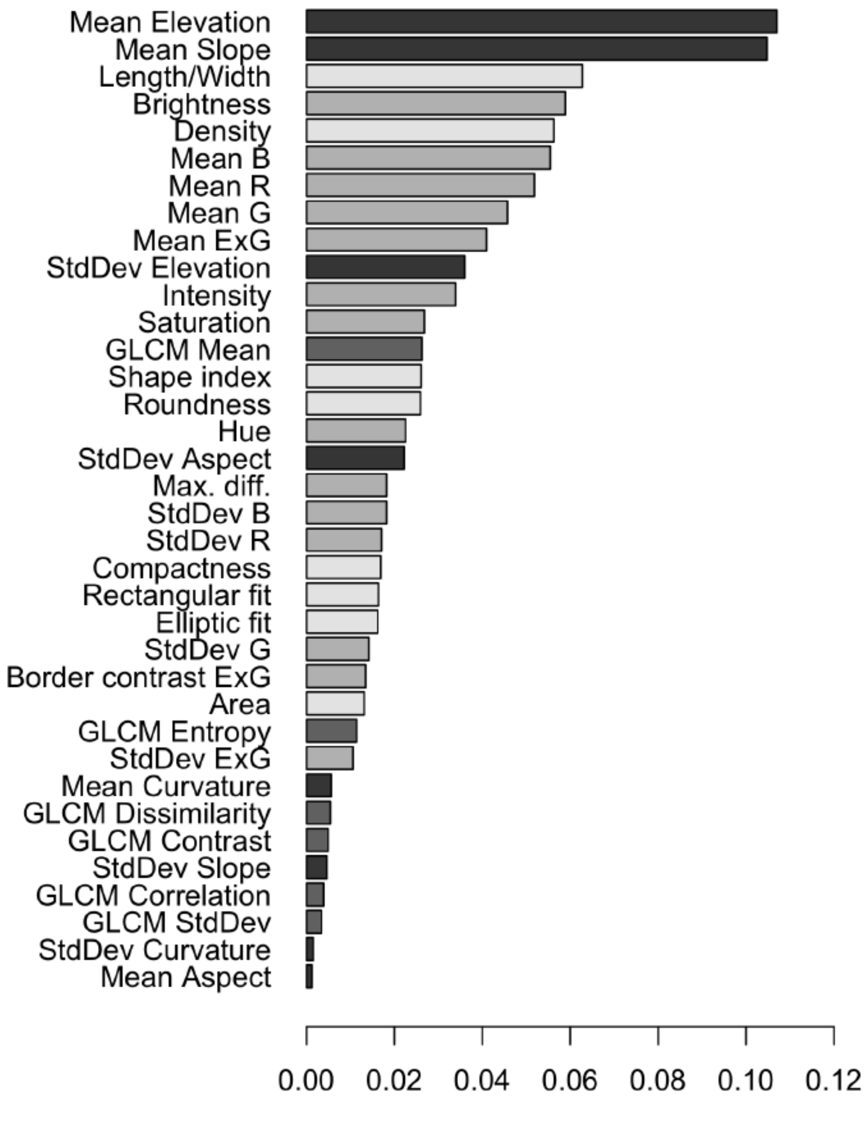

Figure A.1: *Graph showing the feature importance results of the random forest classifier. Features are categorized into groups represented by different grey levels. From dark to light grey: Digital Terrain Model (DTM) related features, Grey Level Co-occurrence Matrix (GLCM) texture related features, color related features, and geometric features. The feature importance shows, that a mix of different categories are required for successful classification. Except for GLCM mean, texture related features generally show the least importance. R=red, G=green, B=blue.*

B

Supplemental Material: Identifying Soil Erosion Processes in Alpine Grasslands on Aerial Imagery with a U-Net Convolutional Neural Network

Details on the Neural Network Architecture

The main components of the U-Net architecture are *convolution*, *max pooling*, *dropout*, and *transposed convolution* operations with *rectified linear unit* (ReLU) activations. In the following, we give some more details on the individual components of the neural network and how these components are combined in the U-Net architecture.

The convolution operation is represented by a *kernel* (typically of size 3×3) which processes the input image leading to an intermediate representation of activations called the *feature map* (illustrated in Figure B.1 (b)). Using several kernels enables identification of different meaningful features in the input images which are learned during the training of the neural network. Pooling operations combine adjacent pixels into a summary statistic and sub-sample feature maps, a process which effectively reduces the size of the feature map. For instance, the max pooling operation with a 2×2 kernel takes the activation of four adjacent pixels in the feature map and stores only the maximum value in the subsequent feature map (depicted in Figure B.1 (a)). Pooling reduces the number of parameters and induces some amount of translational invariance with respect to the position of objects in an input image. A crucial aspect for training neural networks is to use a non-linear activation function such as ReLU which preserves positive activations and sets negative activations to 0, i.e. $f(x) = \max(0, x)$. The transposed convolution (sometimes referred to as up-convolution, fractionally-strided convolution, or deconvolution) can be viewed as an inverse operation to max pooling which uses convolutional filters to upsample pixels from a feature map to several pixels in a subsequent feature map. Finally, the dropout operation allows switching off individual neurons temporarily. For instance, with a dropout probability of 50% per neuron about half of the neurons can be switched off at random for a single training iteration. This usually improves the stability and accuracy of prediction outcomes.

In the first, contracting, part of the U-Net (see Figure 3.5), a sequence of two convolutional layers (3×3 kernels, stride of 1, and valid padding, i.e. no padding) with ReLU activations followed by a max pooling layer (2×2 kernel, stride of 2) processes the input. With each max pooling application, the size of the resulting feature maps is halved while the number of features is doubled for the subsequent convolutional layer. In the expansive part, a sequence of transposed convolutional layers

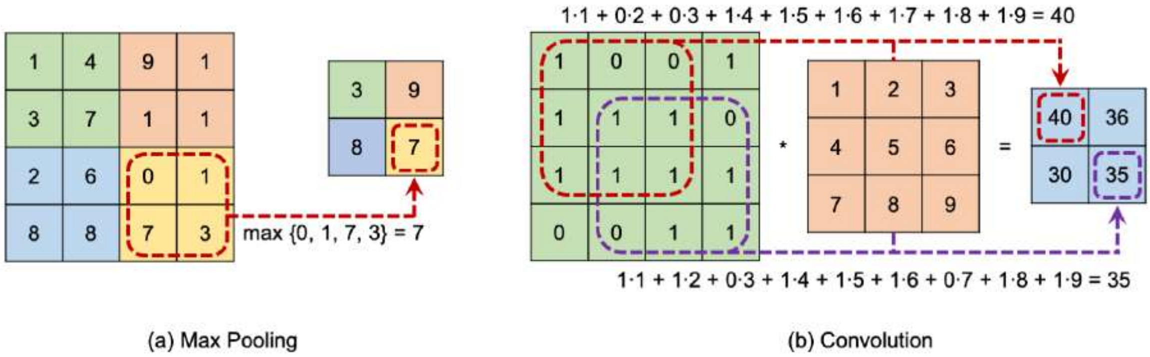

Figure B.1: *Illustration of the max pooling and convolution operation. In this study, for (a) max pooling, a kernel of size* 2×2 *was used with a stride of 2, i.e. the dashed box is shifted to the elements highlighted by the different colours. For (b) convolution, a kernel of size* 3×3 *(highlighted in orange) was used with a stride of 1, i.e. the dashed boxes are shifted by one column / row. The values in a patch of the input map (highlighted in green) are multiplied element-wise with the weights of the convolutional kernel and the results are summed up, forming the feature map. For illustration purposes the weights are chosen from 1 to 9 and are subject to change during training.*

(2×2 kernels, stride of 2, and valid padding) with ReLU activations followed by two convolutional layers (3×3 kernels, stride of 1, and valid padding) and ReLU activations is applied to restore the original image size. Feature maps from the contracting part are appended to the feature maps obtained through the transposed convolutions to provide fine-detail features in the expansive part. Finally, a 1×1 convolutional layer provides the final segmentation output where each channel represents the segmentation map for the individual classes. A pixel-wise *softmax* activation function rescales the activations for each pixel to the $[0, 1]$ interval. More explicitly, for a pixel f in the feature map F and the corresponding activation $a(f)$ which captures the activations for the different classes $c \in \{1, ..., C\}$, the softmax yields $p_c(f) = \frac{\exp\left(a_c(f)\right)}{\sum_{l=1}^{C} \exp\left(a_l(f)\right)}$. Thus, $p_c(f)$ can be interpreted as the probability of pixel f to belong to class c. The neural network is trained with the cross entropy loss which penalises incorrect class assignments with

$$-\frac{1}{N} \sum_{f \in F} \sum_{c \in C} y_c(f) \log(p_c(f)) \tag{B.1}$$

where $N = |F|$ is the number of pixels and $y_c(f)$ is the ground truth class assignment for pixel f, i.e. 1 if c is the correct class and 0 otherwise.

Mixed Thresholds for Trend Analysis

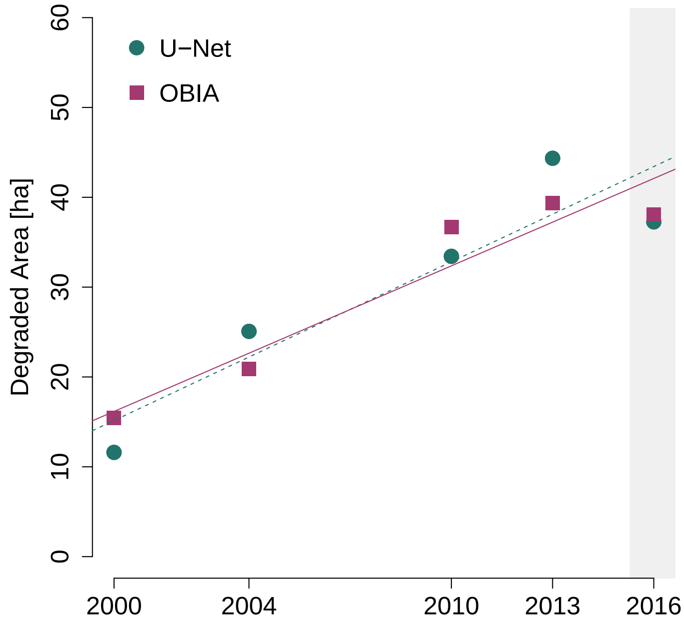

Figure B.2: *Total degraded area prediction of the U-Net with individually selected thresholds best suited for every erosion class on the held-out test region. The thresholds were selected according to a detailed threshold analysis (not shown) to be: 0.2 Shallow Landslides, 0.2 Livestock Trails, 0.3 Sheet Erosion, 0.5 Management Effects. Although deviations in the total degraded area persist, the linear trend of the two methods almost coincides.*

C

Supplemental Material: Investigating Causal Factors of Shallow Landslides in Grassland Regions of Switzerland

Results of Lasso Selection

Boxplots (with whiskers and outliers) of all ten study sites (Figures C.1 - C.10) showing the coefficient range with 100 repetitions (bootstrapping). Numbers above variable names indicate the amount of times it was selected for the model. Boxes show the interquartile range (25th and 75th percentile) and the line within the box indicates the median of the coefficients.

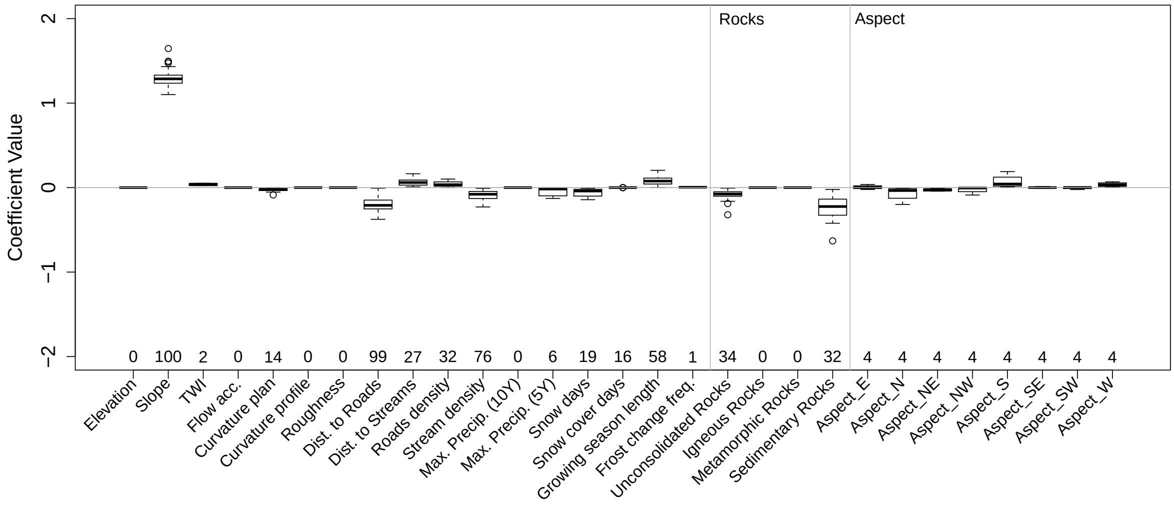

Figure C.1: *Coefficients Arosa*

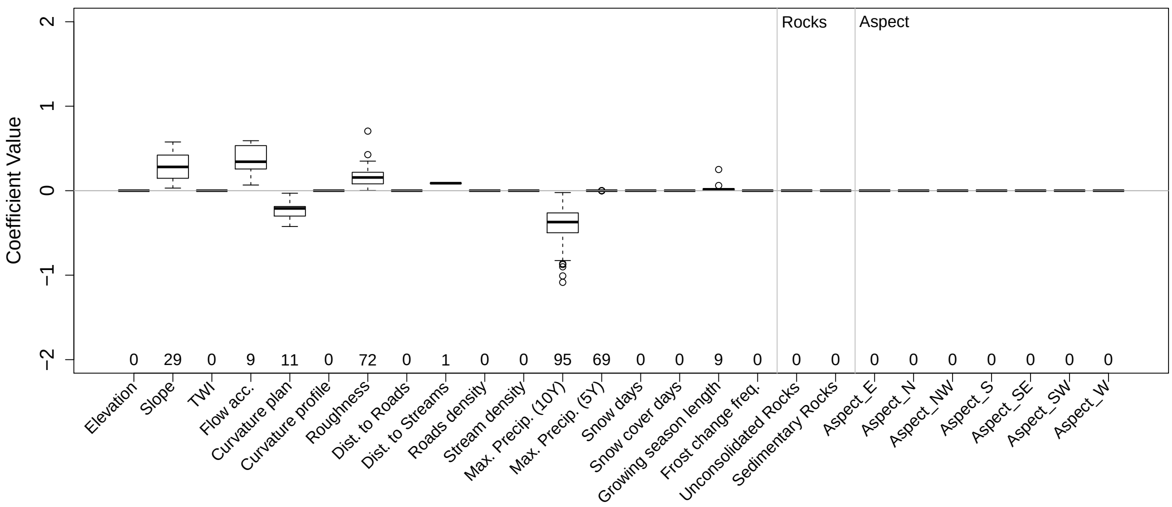

Figure C.2: *Coefficients Baulmes*

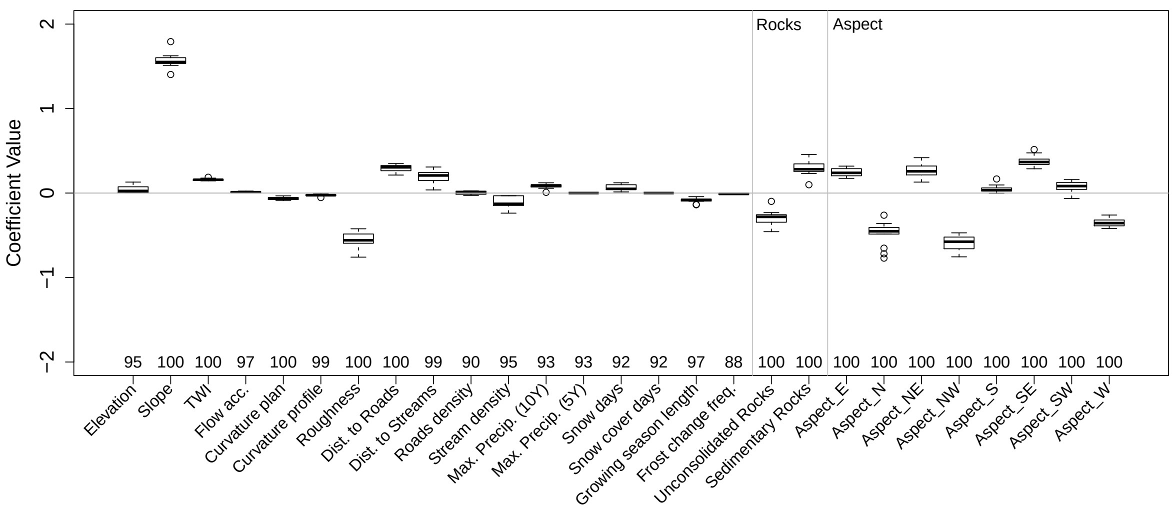

Figure C.3: *Coefficients Chrauchtal*

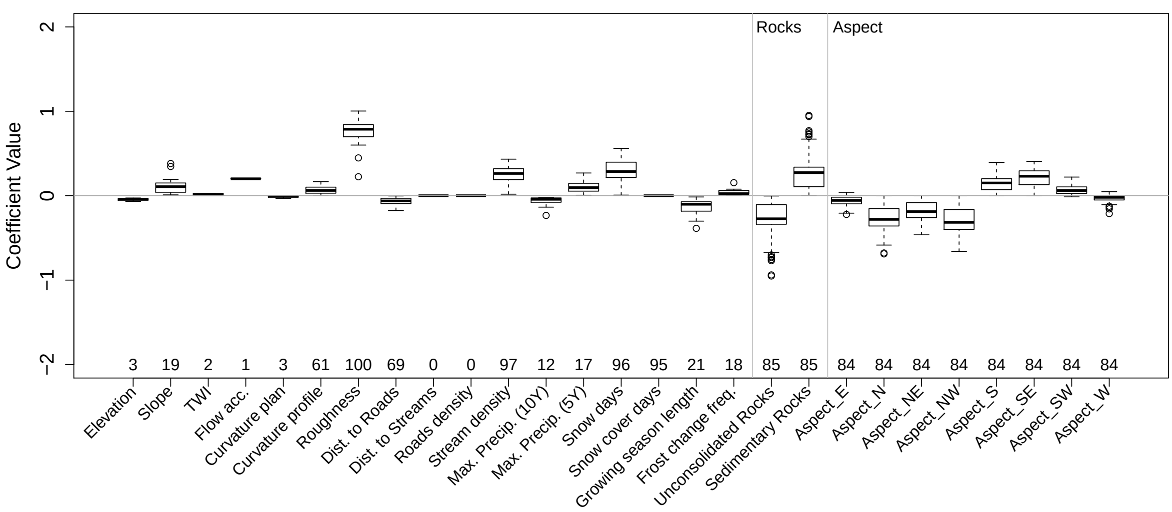

Figure C.4: *Coefficients Hornbachtal*

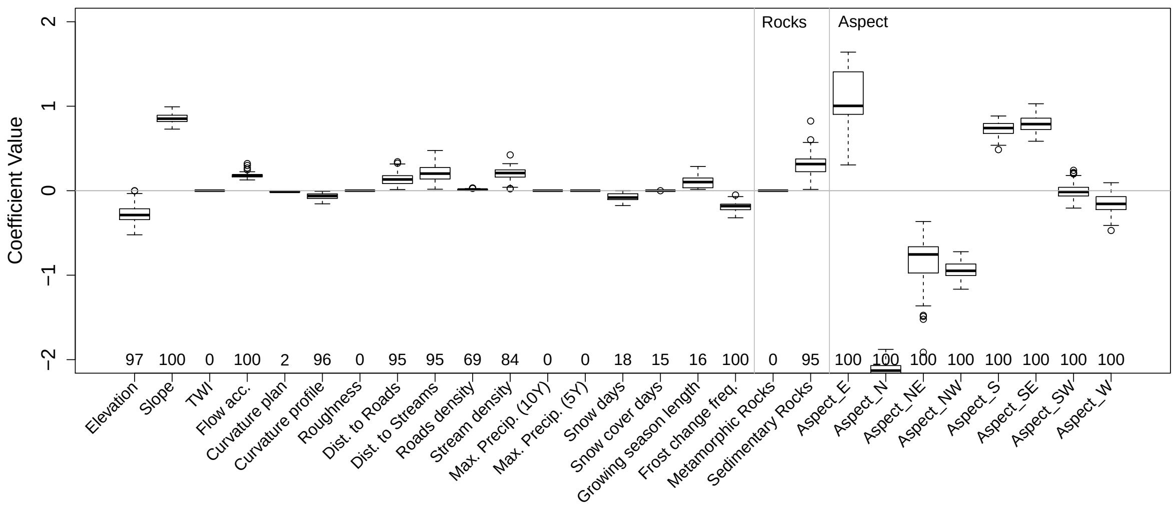

Figure C.5: *Coefficients Rappetal*

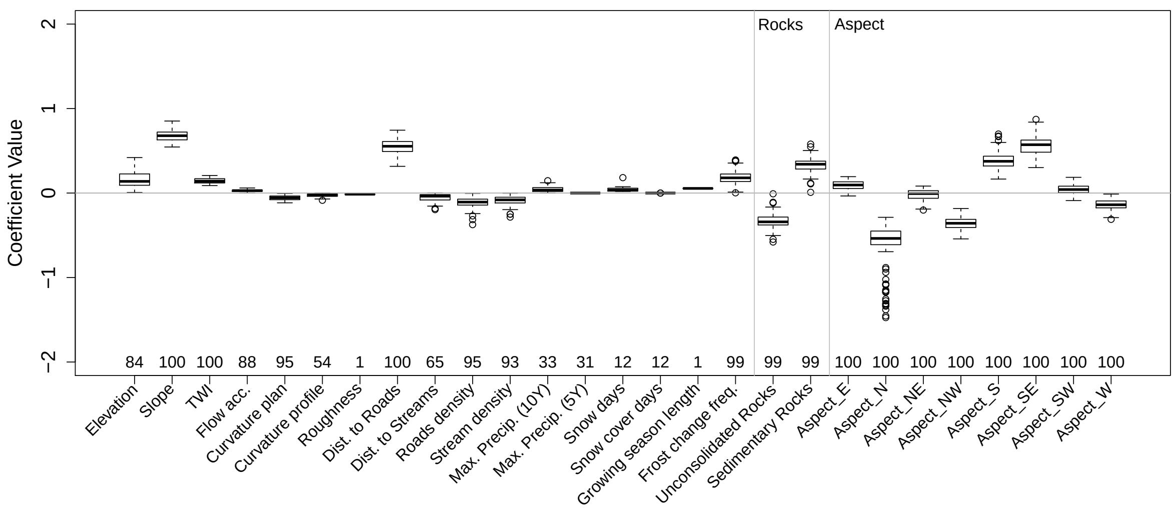

Figure C.6: *Coefficients Turbachtal*

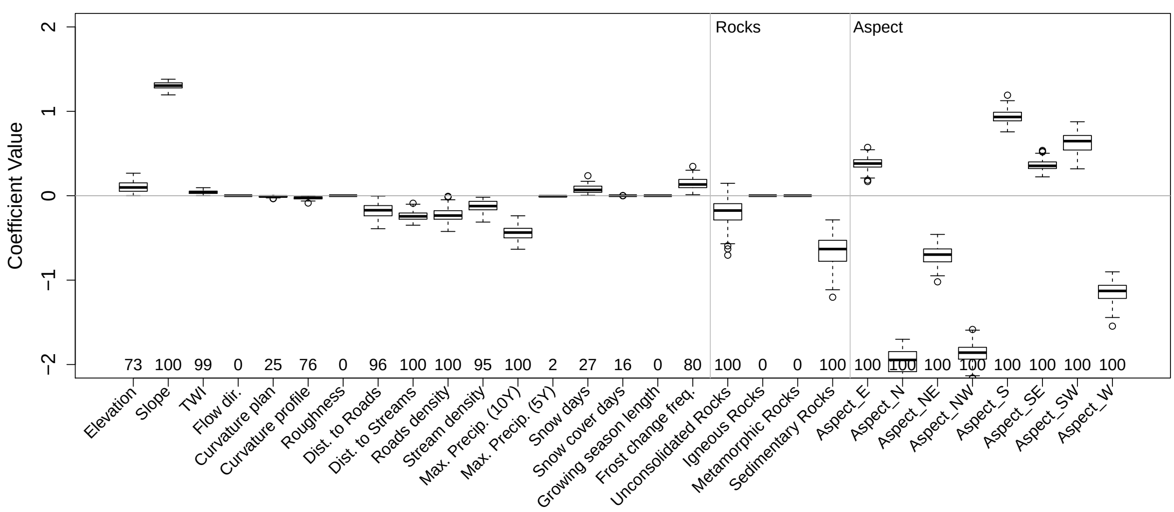

Figure C.7: *Coefficients Urserental*

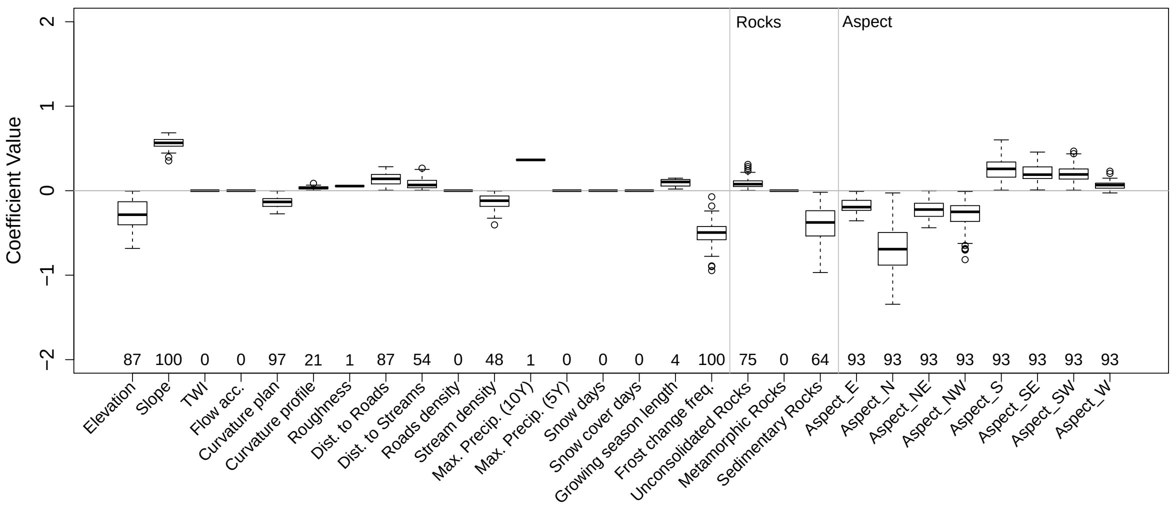

Figure C.8: *Coefficients Val Cluozza*

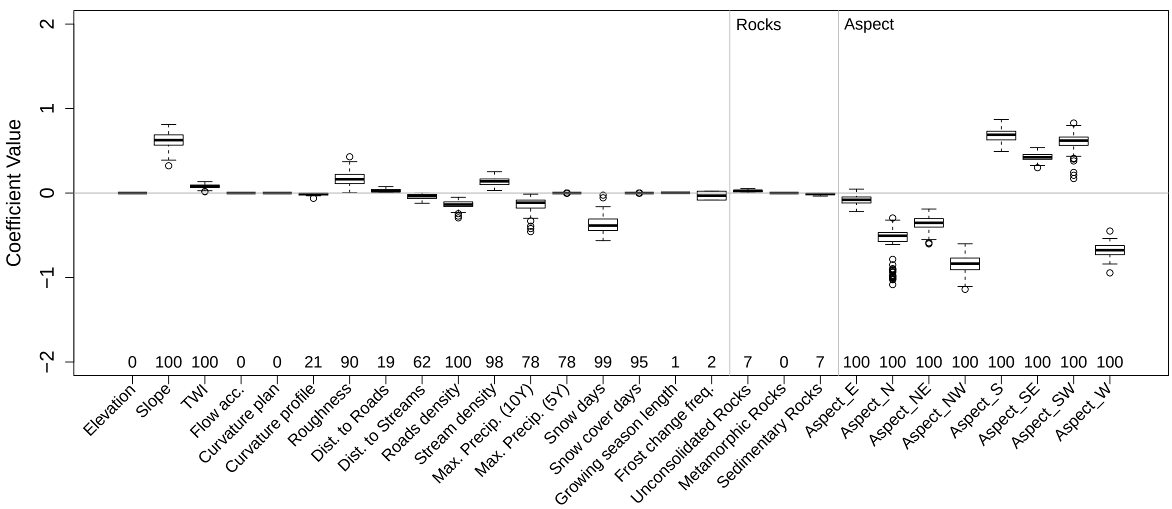

Figure C.9: *Coefficients Val d'Entremont*

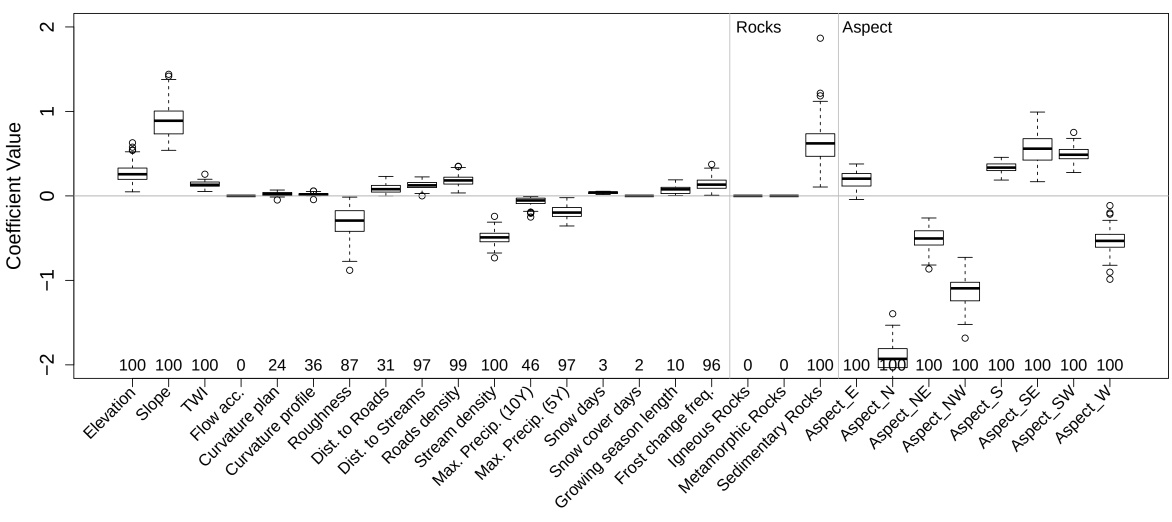

Figure C.10: *Coefficients Val Piora*

Bibliography

Abadi, M., and Coauthors, 2016: TensorFlow: A System for Large-Scale Machine Learning. *Proceedings of the 12th USENIX Symposium on Operating Systems Design and Implementation (OSDI '16)*, 265–283.

Aber, J. S., I. Marzolff, J. B. Ries, and S. E. Aber, 2019: Gully-Erosion Monitoring. *Small-Format Aerial Photography and UAS Imagery*, **(C)**, 259–271.

Akeret, J., C. Chang, A. Lucchi, and A. Refregier, 2017: Radio frequency interference mitigation using deep convolutional neural networks. *Astron. Comput.*, **18**, 35–39.

Alder, S., V. Prasuhn, H. Liniger, K. Herweg, H. Hurni, A. Candinas, and H. U. Gujer, 2015: A high-resolution map of direct and indirect connectivity of erosion risk areas to surface waters in Switzerland-A risk assessment tool for planning and policy-making. *Land Use Policy*, **48**, 236–249.

Alewell, C., P. Borrelli, K. Meusburger, and P. Panagos, 2019: Using the USLE: Chances, challenges and limitations of soil erosion modelling. *Int. Soil Water Conserv. Res.*, **7**, 203–225.

Alewell, C., M. Egli, and K. Meusburger, 2015: An attempt to estimate tolerable soil erosion rates by matching soil formation with denudation in Alpine grasslands. *J. Soils Sediments*, **15**, 1383–1399.

Alewell, C., K. Meusburger, M. Brodbeck, and D. Bänninger, 2008: Methods to describe and predict soil erosion in mountain regions. *Landsc. Urban Plan.*, **88**, 46–53.

Alewell, C., K. Meusburger, G. Juretzko, L. Mabit, and M. E. Ketterer, 2014: Suitability of 239+240Pu and 137Cs as tracers for soil erosion assessment in mountain grasslands. *Chemosphere*, **103**, 274–280.

Alewell, C., B. Ringeval, C. Ballabio, D. A. Robinson, P. Panagos, and P. Borrelli, 2020: Global phosphorus shortage will be aggravated by soil erosion. *Nature Communications*, **11 (1)**.

Alewell, C., M. Schaub, and F. Conen, 2009: A method to detect soil carbon degradation during soil erosion. *Biogeosciences Discussions*, **6**, 5771–5787.

Alshaikhli, T., W. Liu, and Y. Maruyama, 2019: Automated method of road extraction from aerial images using a deep convolutional neural network. *Appl. Sci.*, **9**, 4825.

Amato, G., C. Eisank, D. Castro-Camilo, and L. Lombardo, 2019: Accounting for covariate distributions in slope-unit-based landslide susceptibility models. A case study in the alpine environment. *Engineering Geology*, **260 (August)**, 105 237.

Ancey, C., and V. Bain, 2015: Dynamics of glide avalanches and snow gliding. *Reviews of Geophysics*, **53 (3)**, 745–784.

Angehrn, P., 1996: *Hydrogeologische Grundlagen - Urserental. Geologisches Büro Dr. P. Angehrn AG im Auftrag von: Amt für Umweltschutz - Abteilung Gewässerschutz, Altdorf.*

Apollo, M., V. Andreychouk, and S. S. Bhattarai, 2018: Short-term impacts of livestock grazing on vegetation and track formation in a high mountain environment: A case study from the Himalayan Miyar Valley (India). *Sustainability*, **10**, 951.

Barbb, E., 1984: Innovative approaches to landslide hazard and risk mapping. *Proc. of the IV International Symposiumon Landslides*, Toronto, 307–323.

Baumhoer, C. A., A. J. Dietz, C. Kneisel, and C. Kuenzer, 2019: Automated extraction of antarctic glacier and ice shelf fronts from Sentinel-1 imagery using deep learning. *Remote Sens.*, **11**, 2529.

Beniston, M., 2006: Mountain weather and climate: A general overview and a focus on climatic change in the Alps. *Hydrobiologica*, **562**, 3–16.

Beniston, M., 2012: Is snow in the Alps receding or disappearing? *WIREs Clim. Change*, **3**, 349–358.

Beven, K. J., and M. J. Kirkby, 1979: A physically based, variable contributing area model of basin hydrology. *Hydrological Sciences Bulletin*, **24 (1)**, 43–69.

Bezak, N., and Coauthors, 2021: Soil erosion modelling: A bibliometric analysis. *Environmental Research*, **197**, 111 087.

Bircher, P., H. P. Liniger, and V. Prasuhn, 2019: Comparing different multiple flow algorithms to calculate RUSLE factors of slope length (L) and slope steepness (S) in Switzerland. *Geomorphology*, **346**, 106 850.

Blaschke, T., 2010: Object based image analysis for remote sensing. *ISPRS J. Photogramm. Remote Sens.*, **65**, 2–16.

Blaschke, T., and J. Strobl, 2001: What's wrong with pixels? Some recent developments interfacing remote sensing and GIS. *Geo-Informations-Systeme*, **14 (6)**, 12–17.

Blaschke, T., and Coauthors, 2014: Geographic Object-Based Image Analysis - Towards a new paradigm. *ISPRS Journal of Photogrammetry and Remote Sensing*, **87**, 180–191.

Blaschke, T. M. K. H. R. M., 2015: Object Based Image Analysis: Evolution, History, State-of-the-Art and Future Vision. *Remotely Sensed Data Characterization, Classification, and Accuracies*, 227–289.

Blechschmidt, G., 1990: Die Blaikenbildung im Karwendel. *Jahrbuch des Vereins zum Schutz der Bergwelt*, **55**, 31–45.

Borrelli, P., S. Modugno, P. Panagos, M. Marchetti, B. Sch??tt, and L. Montanarella, 2014: Detection of harvested forest areas in Italy using Landsat imagery. *Applied Geography*, **48 (March)**, 102–111, doi:10.1016/j.apgeog.2014.01.005, URL http://dx.doi.org/10.1016/j.apgeog.2014.01.005.

Borrelli, P., and Coauthors, 2020: Land use and climate change impacts on global soil erosion by water (2015-2070). *Proceedings of the National Academy of Sciences of the United States of America*, **117 (36)**, 21 994–22 001.

Borrelli, P., and Coauthors, 2021: Soil erosion modelling: A global review and statistical analysis. *Science of the Total Environment*, **780**.

Bosco, C., E. Rusco, L. Montanarella, and P. Panagos, 2009: Soil erosion in the Alpine area: risk assessment and climate change. *Studi Trent. Sci. Nat.*, **85**, 117–123.

Breheny, P., and J. Huang, 2015: Group descent algorithms for nonconvex penalized linear and logistic regression models with grouped predictors. *Statistics and Computing*, **25 (2)**, 173–187.

Brier, G. W., 1950: Verification of Forecasts Expressed in terms of Probability. *Monthly Weather Review*, **78 (1)**, 1–3.

Budimir, M. E., P. M. Atkinson, and H. G. Lewis, 2015: A systematic review of landslide probability mapping using logistic regression. *Landslides*, **12 (3)**, 419–436.

Bundzel, M., M. Jaščur, M. Kováč, T. Lieskovský, P. Sinčák, and T. Tkáčik, 2020: Semantic segmentation of airborne lidar data in maya archaeology. *Remote Sensing*, **12 (22)**, 1–22.

Camilo, D. C., L. Lombardo, P. M. Mai, J. Dou, and R. Huser, 2017: Handling high predictor dimensionality in slope-unit-based landslide susceptibility models through LASSO-penalized Generalized Linear Model. *Environmental Modelling and Software*, **97**, 145–156.

Casagli, N., and Coauthors, 2016: Landslide mapping and monitoring by using radar and optical remote sensing: Examples from the EC-FP7 project SAFER. *Remote Sensing Applications: Society and Environment*, **4**, 92–108.

Ceaglio, E., K. Meusburger, M. Freppaz, E. Zanini, and C. Alewell, 2012: Estimation of soil redistribution rates due to snow cover related processes in a mountainous area (Valle d'Aosta, NW Italy). *Hydrol. Earth Syst. Sci.*, **16**, 517–528.

Ceaglio, E., C. Mitterer, M. Maggioni, S. Ferraris, V. Segor, and M. Freppaz, 2017: The role of soil volumetric liquid water content during snow gliding processes. *Cold Regions Science and Technology*, **136**, 17–29.

CH2011, 2011: *Swiss Climate Change Scenarios CH2011*. C2SM, MeteoSwiss, ETH, NCCR Climate, and OcCC, Zurich, 88 pp.

CH2018, 2018: *Climate Scenarios for Switzerland CH2018*. National Centre for Climate Services, Zurich, 24 pp.

Chen, C.-w., H. Chen, and T. Oguchi, 2016: Distributions of landslides, vegetation, and related sediment yields during typhoon events in northwestern Taiwan. *Geomorphology*, **273**, 1–13.

Chen, G., Q. Weng, G. J. Hay, and Y. He, 2018: Geographic object-based image analysis (GEOBIA): emerging trends and future opportunities. *GISci. Remote Sens.*, **55**, 159–182.

Chen, W., X. Xie, J. Wang, B. Pradhan, H. Hong, D. T. Bui, Z. Duan, and J. Ma, 2017: A comparative study of logistic model tree, random forest, and classification and regression tree models for spatial prediction of landslide susceptibility. *Catena*, **151**, 147–160.

Cignetti, M., D. Godone, and D. Giordan, 2019: Shallow landslide susceptibility, rupinaro catchment, liguria (Northwestern Italy). *Journal of Maps*, **15 (2)**, 333–345.

Conoscenti, C., V. Agnesi, S. Angileri, C. Cappadonia, E. Rotigliano, and M. Märker, 2013: A GIS-based approach for gully erosion susceptibility modelling: A test in Sicily, Italy. *Environmental Earth Sciences*, **70 (3)**, 1179–1195.

Copernicus, 2012: CORINE Land Cover. URL https://land.copernicus.eu/pan-european/corine-land-cover.

D'Oleire-Oltmanns, S., I. Marzolff, K. D. Peter, and J. B. Ries, 2012: Unmanned aerial vehicle (UAV) for monitoring soil erosion in Morocco. *Remote Sens.*, **4**, 3390–3416.

D'Oleire-Oltmanns, S., I. Marzolff, D. Tiede, and T. Blaschke, 2014: Detection of gully-affected areas by applying object-based image analysis (OBIA) in the region of Taroudannt, Morocco. *Remote Sens.*, **6**, 8287–8309.

Dommermuth, C., 1995: Beschleunigte Bodenabtragungsvorgänge in der Kulturlandschaft des Nationalparks Berchtesgaden. Ursachen und Auswirkungen aufgezeigt am Beispiel des Jennergebiets. *Forstwiss. Centralbl.*, **144**, 285–292.

Dormann, C. F., and Coauthors, 2013: Collinearity: A review of methods to deal with it and a simulation study evaluating their performance. *Ecography*, **36 (1)**, 27–46.

Durán, Z. H., and R. C. Pleguezuelo, 2008: Soil-erosion and runoff prevention by plant covers. A review. *Agronomy for Sustainable Development*, **28 (1)**, 65–86.

EDA, 2021: Geografie – Fakten und Zahlen. URL https://www.eda.admin.ch/aboutswitzerland/de/home/umwelt/geografie/geografie---fakten-und-zahlen.html.

EEA, 2006: CORINE Land Cover (CLC). URL https://land.copernicus.eu/pan-european/corine-land-cover/clc-2006.

EEA, 2009: Regional climate change and adaptation — The Alps facing the challenge of changing water resources. Tech. Rep. 8, European Environmental Agency, 1–143 pp.

Egli, M., and J. Poulenard, 2017: Soils of mountainous landscapes. *The International Encyclopedia of Geography*, D. Richardson, N. Castree, M. F. Goodchild, A. Kobayashi, W. Liu, and R. A. Marston, Eds., John Wiley & Sons, Inc.

Eisank, C., D. Hölbling, B. Friedl, and Y. Chin, 2014: Expert knowledge for object-based landslide mapping in Taiwan. *South-Eastern Eur. J. Earth Observ.*, **3**, 347–350.

FAO and ITPS, 2015: Status of the World's Soil Resources (SWSR) - Main Report. Tech. rep., FAO and ITPS, 608 pp.

Fischer, F. K., M. Kistler, R. Brandhuber, H. Maier, M. Treisch, and K. Auerswald, 2018: Validation of official erosion modelling based on high-resolution radar rain data by aerial photo erosion classification. *Earth Surf. Proc. Land*, **43**, 187–194.

Fischer, M., K. Rudmann-Maurer, A. Weyand, and J. Stocklin, 2008: Agricultural land use and biodiversity in the Alps: How cultural tradition and socioeconomically motivated changes are shaping grassland biodiversity in the Swiss Alps. *Mountain Research and Development*, **28 (2)**, 148–155.

Flood, N., F. Watson, and L. Collett, 2019: Using a U-net convolutional neural network to map woody vegetation extent from high resolution satellite imagery across Queensland, Australia. *Int. J. Appl. Earth Obs.*, **82**, 101 897.

Frattini, P., G. Crosta, and A. Carrara, 2010: Techniques for evaluating the performance of landslide susceptibility models. *Engineering Geology*, **111 (1)**, 62–72.

Frei, P., S. Kotlarski, M. A. Liniger, and C. Schär, 2018: Future snowfall in the Alps: Projections based on the EURO-CORDEX regional climate models. *Cryosphere*, **12**, 1–24.

Freppaz, M., D. Godone, G. Filippa, M. Maggioni, S. Lunardi, M. W. Williams, and E. Zanini, 2010: Soil erosion caused by snow avalanches: a case study in the Aosta Valley (NW Italy). *Arct. Antarct. Alp. Res.*, **42**, 412–421.

Fromm, R., S. Baumgärtner, G. Leitinger, E. Tasser, and P. Höller, 2018: Determining the drivers for snow gliding. *Nat. Hazards Earth Syst. Sci.*, **18**, 1891–1903.

FSO, 2013: Land use in Switzerland. Results of the Swiss land use statistics. *Federal Statistics Office*, 24.

Fu, Y., K. Liu, Z. Shen, J. Deng, M. Gan, X. Liu, D. Lu, and K. Wang, 2019: Mapping impervious surfaces in town-rural transition belts using China's GF-2 imagery and object-based deep CNNs. *Remote Sens.*, **11**, 280.

Fuhrer, J., M. Beniston, A. Fischlin, C. Frei, S. Goyette, K. Jasper, and C. Pfister, 2006: Climate risks and their impact on agriculture and forests in Switzerland. *Clim. Change*, **79**, 79–102.

Gao, H., P. S. Fam, L. T. Tay, and H. C. Low, 2020: Logistic regression techniques based on different sample sizes in landslide susceptibility assessment: Which performs better? *Compusoft*, **9 (4)**, 3624–3628.

Gariano, S. L., and F. Guzzetti, 2016: Landslides in a changing climate. *Earth-Sci. Rev.*, **162**, 227–252, doi:10.1016/j.earscirev.2016.08.011.

Geitner, C., and Coauthors, 2017: *Chapter 8 - Soil and Land Use in the Alps—Challenges and Examples of Soil-Survey and Soil-Data Use to Support Sustainable Development A2 - Pereira, Paulo*. 221–292 pp.

Geitner, C., and Coauthors, 2021: Shallow erosion on grassland slopes in the European Alps – Geomorphological classification , spatio-temporal analysis , and understanding snow and vegetation impacts. *Geomorphology*, **373**, 107 446.

Ghorbanzadeh, O., T. Blaschke, K. Gholamnia, S. R. Meena, D. Tiede, and J. Aryal, 2019: Evaluation of different machine learning methods and deep-learning convolutional neural networks for landslide detection. *Remote Sens.*, **11 (2)**.

Gianinetto, M., and Coauthors, 2020: Climate Change and Land Cover Transformations Simulated with Automatic Machine Learning. *Climate*, **28 (8)**.

Gobiet, A., S. Kotlarski, M. Beniston, G. Heinrich, J. Rajczak, and M. Stoffel, 2014: 21st century climate change in the European Alps-A review. *Science of the Total Environment*, **493**, 1138–1151.

Goetz, J. N., A. Brenning, H. Petschko, and P. Leopold, 2015: Evaluating machine learning and statistical prediction techniques for landslide susceptibility modeling. *Computers and Geosciences*, **81**, 1–11.

Gómez, H., and T. Kavzoglu, 2005: Assessment of shallow landslide susceptibility using artificial neural networks in Jabonosa River Basin, Venezuela. *Engineering Geology*, **78 (1-2)**, 11–27.

Guirado, E., S. Tabik, D. Alcaraz-Segura, J. Cabello, and F. Herrera, 2017: Deep-Learning Convolutional Neural Networks for scattered shrub detection with Google Earth Imagery. 1–23.

Guzzetti, F., A. C. Mondini, M. Cardinali, F. Fiorucci, M. Santangelo, and K. T. Chang, 2012: Landslide inventory maps: New tools for an old problem. *Earth-Sci. Rev.*, **112**, 42–66.

Guzzetti, F., S. Peruccacci, M. Rossi, and C. P. Stark, 2008: The rainfall intensity-duration control of shallow landslides and debris flows: An update. *Landslides*, **5 (1)**, 3–17.

Hamdi, Z. M., M. Brandmeier, and C. Straub, 2019: Forest damage assessment using deep learning on high resolution remote sensing data. *Remote Sens.*, **11**, 1976.

Hantel, M., C. Maurer, and D. Mayer, 2012: The snowline climate of the Alps 1961-2010. *Theoretical and Applied Climatology*, **110 (4)**, 517–537.

Haralick, R., K. Shanmugan, and I. Dinstein, 1973: Textural features for image classification. *IEEE Trans. Syst. Man Cybern. Syst.*, **3**, 610–621.

Hastie, T., R. Tibshirani, and J. Friedman, 2009: *The Elements of Statistical Learning - Data Mining, Inference, and Prediction*. 2.

Hastie, T., R. Tibshirani, and M. Wainwright, 2016: *Statistical Learning with Sparsity The Lasso and Generalizations*. Chapman and Hall, London, 362 pp.

Heydari, S. S., and G. Mountrakis, 2019: Meta-analysis of deep neural networks in remote sensing: A comparative study of mono-temporal classification to support vector machines. *ISPRS J. Photogramm. Remote Sens.*, **152**, 192–210.

Hölbling, D., L. Abad, Z. Dabiri, G. Prasicek, T.-t. Tsai, and A.-l. Argentin, 2020: Mapping and analyzing the evolution of the Butangbunasi landslide using Landsat time series with respect to heavy rainfall events during Typhoons. *Appl. Sci.*, **10**, 630.

Hölbling, D., H. Betts, R. Spiekermann, and C. Phillips, 2016a: Identifying spatio-temporal landslide hotspots on North Island, New Zealand, by analyzing historical and recent aerial photography. *Geosciences*, **6**, 48.

Hölbling, D., H. Betts, R. Spiekermann, and C. Phillips, 2016b: Semi-automated landslide mapping from historical and recent aerial photography. *Proc. 19th Agile 2016 Conf. Geographic Information Science*, Helsinki, 14–17.

Hölbling, D., C. Eisank, F. Albrecht, F. Vecchiotti, B. Friedl, E. Weinke, and A. Kociu, 2017: Comparing manual and semi-automated landslide mapping based on optical satellite images from different sensors. *Geosciences*, **7**, 37.

Hölbling, D., B. Friedl, and C. Eisank, 2015: An object-based approach for semi-automated landslide change detection and attribution of changes to landslide classes in northern Taiwan. *Earth Sci. Inform.*, **8**, 327–335.

Höller, P., 2014: Snow gliding and glide avalanches: A review. *Natural Hazards*, **71 (3)**, 1259–1288.

Hosmer, D. W., and S. Lemeshow, 2000: *Applied Logistic Regression*. 2nd ed., John Wiley & Sons, Inc., New York.

Huang, B., B. Zhao, and Y. Song, 2018: Urban land-use mapping using a deep convolutional neural network with high spatial resolution multispectral remote sensing imagery. *Remote Sens. Environ.*, **214**, 73–86.

in der Gand, H. R., 1968: Neue Erkenntnisse über das Schneegleiten. *Schweizerische Bauzeitung*, **86 (31)**, 557–561.

IUSS Working Group WRB, 2006: *World reference base for soil resources*. Rome, 1–128 pp.

Ivanovsky, L., V. Khryashchev, V. Pavlov, and A. Ostrovskaya, 2019: Building detection on aerial images using U-NET neural networks. *Conference of Open Innovation Association, FRUCT*, 116–122.

Johansen, K., S. Taihei, D. Tindall, and S. Phinn, 2012: Object-based monitoring of gully extent and volume in North Australia using lidar data. *Proc. 4th GEOBIA*, **I**, 168–173.

Kägi, H., 1973: Die traditionelle Kulturlandschaft im Urserental: Beitrag zur alpinen Kulturgeographie. Ph.D. thesis, University of Zurich, Switzerland, 212 pp.

Karami, A., A. Khoorani, A. Noohegar, S. R. F. Shamsi, and V. Moosavi, 2015: Gully erosion mapping using object-based and pixel-based image classification methods. *Environ. Eng. Geosci.*, **21**, 101–110.

Karger, D., and Coauthors, 2018: Data from: Climatologies at high resolution for the earth's land surface areas. Dryad, Dataset.

Karger, D. N., and N. E. Zimmermann, 2019: Climatologies at High resolution for the Earth Land Surface Areas CHELSA V1 . 2: Technical specification. Tech. Rep. April, 41 pp.

Karger, D. N., and Coauthors, 2017: Climatologies at high resolution for the earth's land surface areas. *Scientific Data*, **4**, 1–20.

Kattenborn, T., J. Eichel, and F. E. Fassnacht, 2019: Convolutional Neural Networks enable efficient, accurate and fine-grained segmentation of plant species and communities from high-resolution UAV imagery. *Sci. Rep.*, **9**, 17 656.

Kavzoglu, T., E. K. Sahin, and I. Colkesen, 2014: Landslide susceptibility mapping using GIS-based multi-criteria decision analysis, support vector machines, and logistic regression. *Landslides*, **11 (3)**, 425–439.

Kingma, D. P., and J. L. Ba, 2015: Adam: A method for stochastic optimization. *3rd International Conference on Learning Representations, ICLR 2015*, 1–15.

Konz, N., D. Baenninger, M. Konz, M. Nearing, and C. Alewell, 2010: Process identification of soil erosion in steep mountain regions. *Hydrol. Earth Syst. Sci.*, **14**, 675–686.

Konz, N., V. Prasuhn, and C. Alewell, 2012: On the measurement of alpine soil erosion. *Catena*, **91**, 63–71.

Korup, O., and C. Rixen, 2014: Soil erosion and organic carbon export by wet snow avalanches. *Cryosphere*, **8**, 651–658.

Krizhevsky, A., I. Sutskever, and E. G. Hinton, 2012: ImageNet Classification with Deep Convolutional Neural Networks Alex. *Advances in Neural Information Processing Systems*, **25**.

Laatsch, W., and U. Baum, 1976: Faktoren der Wald- und Bodenzerstörung durch Schnee in den Alpen. *Agrochimica*, **20**, 324–338.

Labhart, T., 1999: Planbeilage: Geologisch-tektonische Übersichtskarte Aaremassiv, Gotthardmassiv und Tavetscher Zwischemassiv. Balkema, A. A., Rotterdam.

Lal, R., 2001: Soil degradation by erosion. *Land Degradation and Development*, **12 (6)**, 519–539.

Lal, R., 2004: Soil carbon sequestration impacts on global climate change and food security. *Science*, **304 (5677)**, 1623–1627.

Lal, R., 2014: Soil conservation and ecosystem services. *International Soil and Water Conservation Research*, **2 (3)**, 36–47.

Lal, R., 2019: Accelerated Soil erosion as a source of atmospheric CO 2. *Soil and Tillage Research*, **188**, 35–40.

Lee, D. H., Y. T. Kim, and S. R. Lee, 2020: Shallow landslide susceptibility models based on artificial neural networks considering the factor selection method and various non-linear activation functions. *Remote Sensing*, **12 (7)**.

Leitinger, G., K. Meusburger, J. Rüdisser, E. Tasser, J. Walde, and P. Höller, 2018: Spatial evaluation of snow gliding in the Alps. *Catena*, **165**, 567–575.

Leitinger, G., H. Peter, E. Tasser, J. Walde, and U. Tappeiner, 2008: Development and validation of a spatial snow-glide model. *Ecol. Model.*, **211**, 363–374.

Leonarduzzi, E., P. Molnar, and B. W. McArdell, 2017: Predictive performance of rainfall thresholds for shallow landslides in Switzerland from gridded daily data. *Water Resources Research*, 1–11.

Lepeška, T., 2016: Dynamics of development and variability of surface degradation in the subalpine and alpine zones (an example from the Velká Fatra Mts., Slovakia). *Open Geosciences*, **8 (1)**, 771–786.

Li, Y., H. Zhang, X. Xue, Y. Jiang, and Q. Shen, 2018: Deep learning for remote sensing image classification: A survey. *Wiley Interdisciplinary Reviews: Data Mining and Knowledge Discovery*, **8 (6)**, 1–17.

Li, Z., W. Shi, S. W. Myint, P. Lu, and Q. Wang, 2016: Semi-automated landslide inventory mapping from bitemporal aerial photographs using change detection and level set method. *Remote Sensing of Environment*, **175**, 215–230.

Löbmann, M. T., R. Tonin, C. Wellstein, and S. Zerbe, 2020: Determination of the surface-mat effect of grassland slopes as a measure for shallow slope stability. *Catena*, **187**, 104 397.

Lombardo, L., and P. M. Mai, 2018: Presenting logistic regression-based landslide susceptibility results. *Engineering Geology*, **244**, 14–24, doi:10.1016/j.enggeo.2018.07.019.

Lombardo, L., and H. Tanyas, 2021: From scenario-based seismic hazard to scenario-based landslide hazard: fast-forwarding to the future via statistical simulations. *Stochastic Environmental Research and Risk Assessment*, **1**.

Lu, H., L. Ma, X. Fu, C. Liu, Z. Wang, M. Tang, and N. Li, 2020: Landslides information extraction using Object-Oriented Image Analysis paradigm based on Deep Learning and Transfer Learning. *Remote Sens.*, **12**, 752.

Ma, L., Y. Liu, X. Zhang, Y. Ye, G. Yin, and B. A. Johnson, 2019: Deep learning in remote sensing applications: A meta-analysis and review. *ISPRS J. Photogramm. Remote Sens.*, **152**, 166–177.

Maag, S., J. Nösberger, and A. Lüscher, 2001: *Mögliche Folgen einer Bewirtschaftungsaufgabe von Wiesen und Weiden im Berggebiet Ergebnisse des Komponentenprojektes D, Polyprojekt PRIMALP*. Graslandwissenschaften, ETH Zurich, 58 pp.

Märker, M., L. Angeli, L. Bottai, R. Costantini, R. Ferrari, L. Innocenti, and G. Siciliano, 2008: Assessment of land degradation susceptibility by scenario analysis: A case study in Southern Tuscany, Italy. *Geomorphology*, **93 (1-2)**, 120–129.

Martha, T. R., N. Kerle, V. Jetten, C. J. van Westen, and K. V. Kumar, 2010: Characterising spectral, spatial and morphometric properties of landslides for semi-automatic detection using object-oriented methods. *Geomorphology*, **116**, 24–36.

Martha, T. R., N. Kerle, C. J. van Westen, V. Jetten, and K. Vinod Kumar, 2012: Object-oriented analysis of multi-temporal panchromatic images for creation of historical landslide inventories. *ISPRS J. Photogramm. Remote Sens.*, **67**, 105–119.

Mayr, A., M. Rutzinger, M. Bremer, and C. Geitner, 2016: Mapping Eroded Areas on Mountain Grassland With Terrestrial Photogrammetry and Object-Based Image Analysis. *ISPRS Annals Photogramm. Remote Sens. Spat. Inf. Sci.*, 137–144.

Mboga, N., S. Georganos, T. Grippa, M. Lennert, S. Vanhuysse, and E. Wolff, 2019: Fully convolutional networks and geographic object-based image analysis for the classification of VHR imagery. *Remote Sens.*, **11**, 597.

Meier, L., S. Van De Geer, and P. Bühlmann, 2008: The group lasso for logistic regression. *Journal of the Royal Statistical Society. Series B: Statistical Methodology*, **70 (1)**, 53–71.

MeteoSwiss, 2021: The Climate of Switzerland. URL https://www.meteoswiss.admin.ch/home/climate/the-climate-of-switzerland.html.

Meusburger, K., and C. Alewell, 2008: Impacts of anthropogenic and environmental factors on the occurrence of shallow landslides in an alpine catchment (Urseren Valley, Switzerland). *Nat. Hazards Earth Syst. Sci.*, **8**, 509–520.

Meusburger, K., and C. Alewell, 2009: On the influence of temporal change on the validity of landslide susceptibility maps. *Nat. Hazards Earth Syst. Sci.*, **9**, 1495–1507.

Meusburger, K., and C. Alewell, 2014: Soil Erosion in the Alps. *Federal Office for the Environment FOEN*, 118.

Meusburger, K., D. Bänninger, and C. Alewell, 2010a: Estimating vegetation parameter for soil erosion assessment in an alpine catchment by means of QuickBird imagery. *Int. J. Appl. Earth Obs. Geoinf.*, **12**, 201–207.

Meusburger, K., N. Konz, M. Schaub, and C. Alewell, 2010b: Soil erosion modelled with USLE and PESERA using QuickBird derived vegetation parameters in an alpine catchment. *International Journal of Applied Earth Observation and Geoinformation*, **12 (3)**, 208–215.

Meusburger, K., G. Leitinger, L. Mabit, M. H. Mueller, and C. Alewell, 2013: Impact of snow gliding on soil redistribution for a sub-alpine area in Switzerland. *Hydrol. Earth Syst. Sci. Discuss.*, **10**, 9505–9531.

Meusburger, K., G. Leitinger, L. Mabit, M. H. Mueller, A. Walter, and C. Alewell, 2014: Soil erosion by snow gliding - A first quantification attempt in a subalpine area in Switzerland. *Hydrology and Earth System Sciences*, **18 (9)**, 3763–3775.

Meusburger, K., A. Steel, P. Panagos, L. Montanarella, and C. Alewell, 2012: Spatial and temporal variability of rainfall erosivity factor for Switzerland. *Hydrol. Earth Syst. Sci.*, **16**, 167–177.

Moine, M., A. Puissant, and J.-P. Malet, 2009: Detection of landslides from aerial and satellite images with a semi-automatic method. Application to the Barcelonette basin (Alpes-de-Haute-Provence, France). *Int. Conf. 'Landslide Processes: From Geomorphological Mapping to Dynamic Modelling'*, 63–68.

Moser, M., and F. Hohensinn, 1983: Geotechnical aspects of soil slips in Alpine regions. *Engineering Geology*, **19 (3)**, 185–211.

Nearing, M., F. Pruski, and M. O'Neal, 2004: Expected climate change impacts on soil erosion rates: A review. *J. Soil Water Conserv.*, **59**, 43–50.

Nearing, M. A., Y. Xie, B. Liu, and Y. Ye, 2017: Natural and anthropogenic rates of soil erosion. *Int. Soil Water Cons. Res.*, **5**, 77–84.

Newesely, C., E. Tasser, P. Spadinger, and A. Cernusca, 2000: Effects of land-use changes on snow gliding processes in alpine ecosystems. *Basic and Applied Ecology*, **1**, 61–67.

Nhu, V. H., and Coauthors, 2020a: Shallow landslide susceptibility mapping: A comparison between logistic model tree, logistic regression, naïve bayes tree, artificial neural network, and support vector machine algorithms. *International Journal of Environmental Research and Public Health*, **17 (8)**.

Nhu, V. H., and Coauthors, 2020b: Shallow landslide susceptibility mapping by Random Forest base classifier and its ensembles in a Semi-Arid region of Iran. *Forests*, **11 (4)**.

Oh, H. J., and S. Lee, 2017: Shallow landslide susceptibility modeling using the data mining models artificial neural network and boosted tree. *Applied Sciences (Switzerland)*, **7 (10)**, 1–14.

O'Mara, F. P., 2012: The role of grasslands in food security and climate change. *Annals of Botany*, **110 (6)**, 1263–1270.

Osman, K. T., 2014: *Soil degradation, conservation and remediation*, Vol. 9789400775. 1–237 pp.

Pan, X., J. Zhao, and J. Xu, 2019: An object-based and heterogeneous segment filter convolutional neural network for high-resolution remote sensing image classification. *Int. J. Remote Sens.*, **40**, 5892–5916.

Parente, L., E. Taquary, A. P. Silva, C. Souza, and L. Ferreira, 2019: Next generation mapping: Combining deep learning, cloud computing, and big remote sensing data. *Remote Sensing*, **11 (23)**.

Pérez, E., 2017: Monitoring soil erosion by raster images: From aerial photographs to drone taken pictures. *European Journal of Geography*, **8 (1)**, 117–129.

Persichillo, M. G., and Coauthors, 2017: Shallow landslides susceptibility assessment in different environments. *Geomatics, Natural Hazards and Risk*, **8 (2)**, 748–771.

Petschko, H., A. Brenning, R. Bell, J. Goetz, and T. Glade, 2014: Assessing the quality of landslide susceptibility maps - Case study Lower Austria. *Natural Hazards and Earth System Sciences*, **14 (1)**, 95–118.

Pimentel, D., 2006: Soil erosion: A food and environmental threat. *Environment, Development and Sustainability*, **8 (1)**, 119–137.

Pimentel, D., and M. Burgess, 2013: Soil Erosion Threatens Food Production. *Agriculture*, **3 (3)**, 443–463.

Pimentel, D., and N. Kounang, 1998: Ecology of soil erosion in ecosystems. *Ecosystems*, **1 (5)**, 416–426.

Pimentel, D., and Coauthors, 1995: Environmental and economic costs of soil erosion and conservation benefits. *Science*, **267 (5201)**, 1117–1123.

Pintaldi, E., C. Hudek, S. Stanchi, T. Spiegelberger, E. Rivella, and M. Freppaz, 2017: Sustainable soil management in ski areas: Threats and challenges. *Sustainability (Switzerland)*, **9 (11)**, 1–17.

Pohl, M., D. Alig, C. Körner, and C. Rixen, 2009: Higher plant diversity enhances soil stability in disturbed alpine ecosystems. *Plant and Soil*, **324 (1)**, 91–102.

Poulenard, J., and P. Podwojewski, 2004: Alpine Soils. *Encyclopedia of Soil Science, Third Edition*.

Prakash, N., A. Manconi, and S. Loew, 2020: Mapping landslides on EO data: Performance of deep learning models vs. Traditional machine learning models. *Remote Sens.*, **12 (3)**.

Prasuhn, V., H. Liniger, S. Gisler, K. Herweg, A. Candinas, and J. P. Clément, 2013: A high-resolution soil erosion risk map of Switzerland as strategic policy support system. *Land Use Policy*, **32**, 281–291.

Pruski, F. F., and M. A. Nearing, 2002: Climate-induced changes in erosion during the 21st century for eight U.S. locations. *Water Resour. Res.*, **38**, 1–11.

Radoux, J., and P. Bogaert, 2017: Good practices for object-based accuracy assessment. *Remote Sens.*, **9**, 1–23.

Raja, N. B., I. Çiçek, N. Türkoğlu, O. Aydin, and A. Kawasaki, 2017: Landslide susceptibility mapping of the Sera River Basin using logistic regression model. *Natural Hazards*, **85 (3)**, 1323–1346.

Rickli, C., and F. Graf, 2009: Effects of forests on shallow landslides – case studies in Switzerland. *For. Snow Landsc. Res.*, **82**, 33–44.

Ronneberger, O., P. Fischer, and T. Brox, 2015: U-net: Convolutional networks for biomedical image segmentation. *Medical Image Computing and Computer-assisted intervention - MICCAI 2015*, N. Navab, J. Hornegger, W. Wells, and A. Frangi, Eds., Vol. 9351, 234–241.

Saez, J. L., C. Corona, M. Stoffel, and F. Berger, 2013: Climate change increases frequency of shallow spring landslides in the French Alps. *Geology*, **41**, 619–622.

Samarin, M., L. Zweifel, V. Roth, and C. Alewell, 2020: Identifying soil erosion processes in alpine grasslands on aerial imagery with a u-net convolutional neural network. *Remote Sensing*, **12 (24)**, 1–21, doi:10.3390/rs12244149.

Schauer, T., 1975: Die Blaikenbildung in den Alpen. *Schr.reihe Bayer. Landesamtes Wasserwirt.*, **1**, 29.

Scheurer, K., C. Alewell, D. Bänninger, and P. Burkhardt-holm, 2009: Climate and land-use changes affecting river sediment and brown trout in alpine countries - a review. *Environ. Sci. Pollut. Res.*, **16**, 232–242.

Schmidt, S., C. Alewell, and K. Meusburger, 2018: Mapping spatio-temporal dynamics of the cover and management factor (C-factor) for grasslands in Switzerland. *Remote Sens. Environ.*, **211**, 89–104.

Schmidt, S., C. Alewell, and K. Meusburger, 2019a: Monthly RUSLE soil erosion risk of Swiss grasslands. *J. Maps*, **15**, 247–256.

Schmidt, S., S. Tresch, and K. Meusburger, 2019b: Modification of the RUSLE slope length and steepness factor (LS-factor) based on rainfall experiments at steep alpine grasslands. *MethodsX*, **6**, 219–229.

Shakhashiro, A., and L. Mabit, 2009: Results of an IAEA inter-comparison exercise to assess 137Cs and total 210Pb analytical performance in soil. *Applied Radiation and Isotopes*, **67 (1)**, 139–146.

Shruthi, R. B., N. Kerle, V. Jetten, and A. Stein, 2014: Object-based gully system prediction from medium resolution imagery using Random Forests. *Geomorphology*, **216**, 283–294.

Shruthi, R. B. V., N. Kerle, and V. Jetten, 2011: Object-based gully feature extraction using high spatial resolution imagery. *Geomorphology*, **134**, 260–268.

Shruthi, R. B. V., N. Kerle, V. Jetten, L. Abdellah, and I. Machmach, 2015: Quantifying temporal changes in gully erosion areas with object oriented analysis. *Catena*, **128**, 262–277.

Sidle, R. C., and T. A. Bogaard, 2016: Dynamic earth system and ecological controls of rainfall-initiated landslides. *Earth-Science Reviews*, **159**, 275–291, doi:10.1016/j.earscirev.2016.05.013, URL http://dx.doi.org/10.1016/j.earscirev.2016.05.013.

Smith, D. D., and W. H. Wischmeier, 1957: Factors affecting sheet and rill erosion. *Eos, Trans. Amer. Geophys. Union*, **38**, 889–896, doi: 10.1029/TR038i006p00889.

Stanchi, S., M. Freppaz, E. Ceaglio, M. Maggioni, K. Meusburger, C. Alewell, and E. Zanini, 2014: Soil erosion in an avalanche release site (Valle d'Aosta: Italy): Towards a winter factor for RUSLE in the Alps. *Nat. Hazards Earth Syst. Sci.*, **14**, 1761–1771.

Steger, S., A. Brenning, R. Bell, H. Petschko, and T. Glade, 2016: Exploring discrepancies between quantitative validation results and the geomorphic plausibility of statistical landslide susceptibility maps. *Geomorphology*, **262**, 8–23.

Steyerberg, E. W., A. J. Vickers, N. R. Cook, T. Gerds, M. Gonen, N. Obuchowski, M. J. Pencina, and M. W. Kattan, 2010: Assessing the performance of prediction models: A framework for traditional and novel measures. *Epidemiology*, **21 (1)**, 128–138.

Stumpf, A., and N. Kerle, 2011: Object-oriented mapping of landslides using random forests. *Remote Sens. Environ.*, **115**, 2564–2577.

Stumpf, F., M. K. Schneider, A. Keller, A. Mayr, T. Rentschler, R. G. Meuli, M. Schaepman, and F. Liebisch, 2020: Spatial monitoring of grassland management using multi-temporal satellite imagery. *Ecological Indicators*, **113**, 106 201.

Swisstopo, 2010: Swissimage. Das digitale Farborthophotomosaik der Schweiz.

Swisstopo, 2014: SwissALTI3D. Das hoch aufgelöste Terrainmodell der Schweiz.

Swisstopo, 2019: SwissTLM3D. Das grossmassstäbliche Topografische Landschaftsmodell der Schweiz.

Swisstopo, 2020: Swissimage - Das digitale Farbphotomosaik der Schweiz. *Produktinformation*, 17.

Tanyaş, H., D. Kirschbaum, and L. Lombardo, 2021: Capturing the footprints of ground motion in the spatial distribution of rainfall-induced landslides. *Bulletin of Engineering Geology and the Environment*, **80 (6)**, 4323–4345.

Tasser, E., M. Mader, and U. Tappeiner, 2003: Effects of land use in alpine grasslands on the probability of landslides. *Basic Appl. Ecol.*, **4**, 271–280.

Tasser, E., and U. Tappeiner, 2002: Impact of land use changes on mountain vegetation. *Appl. Veg. Sci.*, **5**, 173–184.

Tasser, E., U. Tappeiner, and A. Cernusca, 2005: Ecological Effects of Land-use Changes in the European Alps. *Global Change and Mountain Regions: An Overview of Current Knowledge*, 409–420.

Tibshirani, R., 1996: Regression selection and shrinkage via the lasso. 267–288 pp.

Tien Bui, D., T. A. Tuan, H. Klempe, B. Pradhan, and I. Revhaug, 2016: Spatial prediction models for shallow landslide hazards: a comparative assessment of the efficacy of support vector machines, artificial neural networks, kernel logistic regression, and logistic model tree. *Landslides*, **13 (2)**, 361–378.

Torresani, L., J. Wu, R. Masin, M. Penasa, and P. Tarolli, 2019: Estimating soil degradation in montane grasslands of North-eastern Italian Alps (Italy). *Heliyon*, **5**, e01 825.

Valavi, R., J. Elith, J. J. Lahoz-Monfort, and G. Guillera-Arroita, 2019: blockCV: An r package for generating spatially or environmentally separated folds for k-fold cross-validation of species distribution models. *Methods in Ecology and Evolution*, **10 (2)**, 225–232.

Von Ruette, J., P. Lehmann, and D. Or, 2013: Rainfall-triggered shallow landslides at catchment scale: Threshold mechanics-based modeling for abruptness and localization. *Water Resources Research*, **49 (10)**, 6266–6285.

Vorpahl, P., H. Elsenbeer, M. Märker, and B. Schröder, 2012: How can statistical models help to determine driving factors of landslides? *Ecological Modelling*, **239**, 27–39.

Vrieling, A., S. C. Rodrigues, H. Bartholomeus, and G. Sterk, 2007: Automatic identification of erosion gullies with ASTER imagery in the Brazilian Cerrados. *International Journal of Remote Sensing*, **28 (12)**, 2723–2738.

Wang, B., Z. Zhang, X. Wang, X. Zhao, L. Yi, and S. Hu, 2020: Object-based mapping of gullies using optical images: A case study in the black soil region, Northeast of China. *Remote Sens.*, **12**, 487.

Wiegand, C., and C. Geitner, 2010a: Flachgründiger abtrag auf Wiesen- und Weideflächen in den Alpen (Blaiken) - Wissensstand, Datenbasis und Forschungsbedarf. *Mitt. Osterr. Geogr. G.*, **152**, 130–162.

Wiegand, C., and C. Geitner, 2010b: Shallow erosion in grassland areas in the Alps. What we know and what we need to investigate further. 76–83.

Wiegand, C., and C. Geitner, 2013: Investigations into the distribution and diversity of shallow eroded areas on steep grasslands in Tyrol (Austria). *Erdkunde*, **67**, 325–343.

Wiegand, C., M. Rutzinger, K. Heinrich, and C. Geitner, 2013: Automated extraction of shallow erosion areas based on multi-temporal ortho-imagery. *Remote Sens.*, **5**, 2292–2307.

Wilks, D., 2006: *Statistical Methods in the Atmospheric Sciences*. 2nd ed., Academic Press, London.

Wilson, M. F., B. O'Connell, C. Brown, J. C. Guinan, and A. J. Grehan, 2007: *Multiscale terrain analysis of multibeam bathymetry data for habitat mapping on the continental slope*, Vol. 30. 3–35 pp.

Woebbecke, D. M., G. E. Meyer, K. Von Bargen, and D. A. Mortensen, 1995: Color indices for weed identification under various soil, residue, and lighting conditions. *Trans. ASAE*, **38**, 259–269.

Wood, J. L., S. Harrison, T. A. R. Turkington, and L. Reinhardt, 2016: Landslides and synoptic weather trends in the European Alps. *Climatic Change*, **136**, 297–308.

Wulamu, A., Z. Shi, D. Zhang, and Z. He, 2019: Multiscale Road Extraction in Remote Sensing Images. *Comput. Intel. Neurosc.*, **2019**, 1–9.

Wyss, R., 1986: Die Urseren-Zone - Lithostratigraphie und Tektonik. *Eclogae Geol. Hel.*, **79**, 731–767.

Xu, Y., L. Wu, Z. Xie, and Z. Chen, 2018: Building extraction in very high resolution remote sensing imagery using deep learning and guided filters. *Remote Sens.*, **10**, 144.

Yang, J., J. Guo, H. Yue, Z. Liu, H. Hu, and K. Li, 2019: CDnet: CNN-based cloud detection for remote sensing imagery. *IEEE Trans. Geosci. Remote Sens.*, **57**, 6195–6211.

Yi, Y., Z. Zhang, W. Zhang, C. Zhang, W. Li, and T. Zhao, 2019: Semantic segmentation of urban buildings from VHR remote sensing imagery using a deep convolutional neural network. *Remote Sens.*, **11**, 1774.

Yong-Zhong, S., L. Yu-Lin, C. Jian-Yuan, and Z. Wen-Zhi, 2005: Influences of continuous grazing and livestock exclusion on soil properties in a degraded sandy grassland, Inner Mongolia, northern China. *Catena*, **59 (3)**, 267–278.

Yuan, M., and Y. Lin, 2006: Model selection and estimation in regression with grouped variables. *Journal of the Royal Statistical Society. Series B: Statistical Methodology*, **68 (1)**, 49–67.

Yuan, M., Z. Liu, and F. Wang, 2019: Using the wide-range attention u-net for road segmentation. *Remote Sens. Lett.*, **10**, 506–515.

Yuan, Q., and Coauthors, 2020: Deep learning in environmental remote sensing: Achievements and challenges. *Remote Sens. Environ.*, **241**, 111 716.

Zakerinejad, R., and M. Märker, 2015: An integrated assessment of soil erosion dynamics with special emphasis on gully erosion in the Mazayjan basin, southwestern Iran. *Natural Hazards*, **79 (1)**, 25–50.

Zevenbergen, L. W., and T. C., 1987: Quantitative analysis of land surface topography. *Earth Surface Processes and Landforms*, **12**, 47–56.

Zhang, C., I. Sargent, X. Pan, H. Li, A. Gardiner, J. Hare, and P. M. Atkinson, 2018a: An object-based convolutional neural network (OCNN) for urban land use classification. *Remote Sensing of Environment*, **216**, 57–70.

Zhang, L., L. Zhang, and V. Kumar, 2016: Deep learning for Remote Sensing Data. *IEEE Geoscience and Remote Sensing Magazine*, **7954154**, 18.

Zhang, Z., Q. Liu, and Y. Wang, 2018b: Road Extraction by Deep Residual U-Net. *IEEE Geosci. Remote Sens. Lett.*, **15**, 749–753.

Zhao, C., and Z. Lu, 2018: Remote sensing of landslides-A review. *Remote Sensing*, **10 (2)**, 8–13.

Zhao, Y., S. Peth, J. Krümmelbein, R. Horn, Z. Wang, M. Steffens, C. Hoffmann, and X. Peng, 2007: Spatial variability of soil properties affected by grazing intensity in Inner Mongolia grassland. *Ecological Modelling*, **205 (1-2)**, 241–254.

Zhong, C., Y. Liu, P. Gao, W. Chen, H. Li, Y. Hou, T. Nuremanguli, and H. Ma, 2020: Landslide mapping with remote sensing: challenges and opportunities. *International Journal of Remote Sensing*, **41 (4)**, 1555–1581.

Zhu, X. X., D. Tuia, L. Mou, G. S. Xia, L. Zhang, F. Xu, and F. Fraundorfer, 2017: Deep learning in remote sensing: a review. *arXiv*, **(41501462)**, 1–60.

Zweifel, L., K. Meusburger, and C. Alewell, 2019: Spatio-temporal pattern of soil degradation in a Swiss Alpine grassland catchment. *Remote Sens. Environ.*, **235**, 111 441.

Zweifel, L., M. Samarin, K. Meusburger, and C. Alewell, 2021: Investigating Causal Factors of Shallow Landslides in Grassland Regions of Switzerland. *Natural Hazards and Earth System Sciences*, 1–24, doi:10.5194/nhess-2021-198.

Acknowledgments

First, I would like to express my gratitude to Christine Alewell and Katrin Meusburger, who co-supervised my thesis and supported and guided me during the past four years.

Thank you also to Maxim, for the collaboration on this project and for teaching me many cool and valuable skills.

Many thanks to all my UGW colleagues for creating such a nice and fun atmosphere to work, relaxing breaks, countless cakes (keeping moral and blood sugar levels high) as well as during the past year for keeping a sense of community going while working from home.

A special thank you to Miriam, for being such a great friend during this adventure.

Thank you to my family and friends for always encouraging me and last but not least a massive thanks to Roman for his continuous care and support.

Curriculum Vitae

Lauren Zweifel

2017 – 2021	PhD at the Department of Environmental Science, University of Basel Thesis: *Identifying Soil Erosion Processes in the Alps using Machine Learning Techniques*
Autumn/Winter 2016	Internship at the Swiss Federal Office for the Environment, Bern
2013 – 2016	Master of Science in Atmospheric Sciences, University of Innsbruck, Austria Thesis: *Probabilistic Foehn Forecasting for the Gotthard Region based on Model Output Statistics*
Autumn/Winter 2012	Internship at SRF Meteo, Swiss Radio and Television, Zürich
2009 – 2013	Bachelor of Science in Geosciences, University of Basel Thesis: *Vegetationsdynamik im Nordosten Australiens – Vergleich eines neutralen Jahres und eines El Niño beeinflussten Jahres anhand von MODIS-Satellitendaten*
2004 – 2009	Swiss Matura at Gymnasium Leonhard, Basel
1996 – 2004	Elementary and Middle School in Basel
July 1990	Born in Basel, Switzerland